Probing the Symmetry-Breaking Phases in Iron-based Superconductors with Combined Strain, Transport and X-ray Techniques

Joshua Javier Sanchez

A dissertation

submitted in partial fulfillment of the

requirements for the degree of

Doctor of Philosophy

University of Washington

2021

Reading Committee:

Assistant Professor Jiun-Haw Chu, Chair

Professor Anton Andreev

Professor Miguel Morales

Program authorized to offer degree:
Department of Physics

University of Washington

Abstract

Probing the Symmetry-Breaking Phases in Iron-based Superconductors with Combined Strain, Transport and X-ray Techniques

Joshua Javier Sanchez

Chair of Supervisory Committee:

Jiun-Haw Chu, Department of Physics

Spontaneous rotational symmetry breaking phases, such as the electronic nematic phase and charge and spin stripe phases, are commonly found in the phase diagram of strongly correlated materials including many of the high-temperature superconductors. This thesis is essentially a study of how tuning parameters, namely applied uniaxial stress and applied magnetic field, can interact with the rotational symmetry-breaking order parameters of these phases, either to probe the system and better understand its intrinsic properties or to create new states in the system that are not spontaneously generated. This thesis discusses the development of a methodology which combines synchrotron x-ray techniques and transport measurements of a single crystal sample mounted to a uniaxial stress device. This methodology is used in iron-based high temperature superconducting materials to probe the nematic and magnetic phases. In Co-doped $BaFe_2As_2$, the coupling between electronic nematicity, the crystal lattice and the resistivity anisotropy is probed by strain, and a temperature and phase independent transport-structural correspondence is demonstrated. In $EuFe_2As_2$, the effects of nematicity on the Eu localized magnetic order is demonstrated from a strongly anisotropic antiferromagnetic coupling between Eu moments. While the work in this thesis is primarily focused on iron-based superconductors, these ideas are very general to the field of condensed matter physics, and this methodology of applied fields combined with x-ray measurements developed here is broadly applicable to systems with structural domains, large magnetoelastic coupling, and other strongly correlated electron effects.

Acknowledgements & Dedications

As I write this, it is August 30th, 2021, and I am moments away from submitting this thesis and finishing my PhD in Physics at the University of Washington. I have my first first-author paper published in a high-impact journal and have given talks on this research at Stanford, Caltech and MIT among other research universities. I have just won an NSF postdoctoral fellowship and will begin a new position at MIT in a couple of weeks. I appear to be on track to build a real science career, either at a university or at a national laboratory, and I feel more confident than ever in my ability to do so. To get here required a tremendous amount of effort over years. Several times I was not successful in a deeply-desired personal or career goal, and I needed to soul search and redefine what my goals were. Many other times, I achieved a goal but only just barely, and was afterwards left feeling burned out or emotionally exhausted. I worked to develop myself as a scientist while navigating difficult family situations and inter and intrapersonal conflicts. As I am now preparing to finish this degree, I am recalling all of the very many people who contributed to me becoming who I am and who supported me through difficult times. I would like here to attempt to name names and express my gratitude to some of these people, knowing that it will be an incomplete list.

Starting at my very foundation, I have to thank my two parents, Diane and Javier, and my two younger brothers, Nico and Dillon. It's hard to express how much they mean to me and of course I can't sum it up in a paragraph. My dad has an incredible work ethic and is intensely self-motivated, and remembering how hard he's had to work to get where he has gotten to has always helped me refocus when I lose drive. My mom is one of the kindest, happiest people I've ever met and she more than anyone can recharge me when I've pushed myself too hard. Both of them are incredibly patient and generous people and I have learned many ways to be a good person from them. I cherish my childhood memories with my brothers, and they are the people who I've laughed the hardest with in this life. To a large extent, my instinct to teach and mentor goes all the way back to being an oldest child and raising my younger brothers. The experience taught me that being a mentor to someone isn't about deciding who they should become but supporting them through their life journey as they become who they want to be.

I am grateful to my big, wonderful family, which has a plethora of "characters" and "strong personalities" that make life anything but boring. A nonexhaustive list of people who taught me and helped raise me, who fed me and let me crash with them, and who made my life fuller: Al and Mary, Brian and Dawn, Luis y Ana, Lucho, Guapo, Angelica, Jose, Jessica, Marina, and Cecilia. I have so many great memories with so many people and I think I'm really lucky to have you all in my life. Looking back, I think it was really important to me to have Brian and Dawn as people with engineering degrees who did science projects with me as a child and who I could talk about math science and sci-fi ideas with in detail. Besides them, I really don't think I had any role models in STEM or any personal connection with science until I started college and suddenly found myself engulfed by it. I want to thank my cousin Marina for being so hospitable and supportive in the final year and especially the final months of my program. And finally, I am thankful for a lifelong

friendship with mi comadre Leti, my ride or die, and I am so thankful to Leti for bringing my beautiful and clever goddaughter Crisana and her beautiful and clever sister Alexa into the world.

Growing up, I didn't feel like I knew anyone who was nearly as much of a nerd as I was and I often felt isolated, but I want to say thank you to those friends who I have the best memories with; thank you Casey, Jake, Schreier, Alty, Kal, Ashley, Rhoda, and Amanda.

When I went to college, it was the first time I really felt like I was somewhere I belonged, and I've never really doubted my interest in an academic career since then even if at times I've doubted my ability to actually succeed. I'd like to thank the scientists, professors, students and staff who helped make my 5 years at the University of Wisconsin such a positive formative experience. I started college as part of the Chancellor's Scholars program led by Dr. Mercile Lee and meeting her changed my whole perspective of the nature of equity work. She was my first academic role model and remains a guiding presence for me. In her program I also met a lifelong friend, thank you Andre for existing! Thank you Yolanda and Dominic for always making time for me when I needed to talk.

From my undergraduate neuroscience lab, I thank Dr. Tononi for the opportunity to work with him studying the neuroscience of sleep, and for him giving me the chance to partner with a postdoc to try and develop a new TMS/EEG technique (it didn't work! but it was the first time I really felt like I was actively doing real science and I loved every minute of that experiment, thank you Jan!). Big thank you's to my mentors, Erik and Melanie, for your support and patience as I developed from a kid to a real researcher. A huge thank you to Simone for helping me arrange a summer REU in Milan learning TMS, it was an unforgettable experience. Also Jeff, Tim, Goldstein, Daniella, Francesca, Marcello Massimini and Barry Van Veen. And thank you to Dr. Janet Branchaw for taking me into her URM program and exposing me to the broader culture of academic research. Dave, I could thank you for a lot of career things but maybe your biggest impact on me was introducing me to Steely Dan and A Tribe Called Quest, the soundtracks to many late hours in the lab.

Next, thank you's to the physics department. First, thank you to the truly wonderful Susan Nossal, from whom I learned how to teach physics and in the process greatly deepened my own understanding of physics. When I was only a week into my first semester of college physics ever, I boldly (foolishly) signed up to be a tutor for intro physics. Susan was the director of the tutoring program; she saw I wasn't ready to teach, but instead of turning me away she let me get paid as an understudy to another tutor and learn the material as I helped teach it. I went on to work as a tutor more than half of my semesters at UW and it prepared me to be an educator alongside my research career. I'll always be inspired by her passion for reducing inequities in education and for being outspoken at meetings and marches for the need to take action on climate change. Thank you too to Amihan and Larry for making tutoring such a fun experience. In this program I also got to meet one of my favorite people ever, thank you Jan for existing! As a student, I only made a strong connection with one professor. In my second semester of college physics I already felt like I was barely staying afloat and my hope to become a physicist was rapidly diminishing; this feeling in fact led me to explore research in the neuro department even while I stayed a physics major. Nevertheless, almost every week I went to office hours with the amazing Prof. Lisa Everett who took the time to help me grasp the foundational concepts of physics and get me through her course. She was never again my class instructor, but there is no one in physics who had a bigger impact on me than her. For the rest of my degree she made time to meet with me and guide me, and ultimately she's the one who gave me the encouragement to apply to the physics PhD program when I didn't think I was good enough

to do it. When I got accepted to the University of Washington, a hypothetical problem became real; I had skipped the undergraduate quantum mechanics courses in favor of neuroscience courses and had very little time to prepare for graduate QM. Lisa told me her stories from grad school about completing whole textbooks to learn physics more deeply, and she gave me a challenge; she told me to do every problem in Shankar's QM textbook. For about 3 months before grad school started, I worked almost every day and often late into the night solving nearly every problem in the book (I allowed myself to skip one per chapter and I never finished the final chapter on intro to field theory). This really did prepare me to do well in my graduate courses and I did pass my QM qualifying exam, and this remains my favorite academic achievement. So, Lisa, my success today results directly from your example and your mentorship, and I can't say thank you loud enough! Finally, I want to thank some of my college friends, who made my life what it was. In no particular order, thank you Chris, Mel, Jay, Plunket, Mitch, Yorgos, Rae, Emily, Dan, Dan + Carlos, Lauren, Lima, Jeff, James, Nathan!, David (with the hair), Matt, Amy, Brent, Ruby, Alisa, Evan, James, Lisa, Carmel, PK, and my bandmates Aarushi, Allie, and Matt; thank you all for the memories!

Now on to Seattle. Of course, I need to thank my advisor Prof. Jiun-Haw Chu for the opportunity to work in his group and learn condensed matter experiment and theory. In particular, I learned a lot about how to write a compelling research paper and how to address reviewer feedback. I want to thank Josh Mutch for being co-first-student with me; together the two of us built Jiun-Haw's lab from an empty room to a bustling research operation with 10+ group members active today. He is truly one of the nicest people I've ever met and I'm glad I got to work with him. I thank Paul Malinowski for literally hundreds of small science chit chats that developed my understanding of physics; in particular, thank you for working through the Girvin and Yang condensed matter textbook with me and for always being down to go see bands play. Nathan Wilson from the lab next door was the first friend I made in Seattle and remained one of my best friends, and I was honored that he asked me to be the officiant at his wedding. Really, there are so many wonderful people working in the basement of the physics building and I am happy I was part of such a great community. In no particular order, I again want to thank Seattle friends who made my life great and supported me through tough times, thank you Sara, Oliver, Isaac, Maria, Eris, Jenny, Audrey, Charlie, Alaina, Kevin, Kyle, Andrew, Akaxia, Natalie, Nozomi, Kshama, Cami, Jorge, Qianni, Yue, Mike, Michael + Raf, J, my incredible mentor Julieta, my lab mentees Philip Ahmed Anna Thalya and Winnie (I'm so happy you are doing so well!) and my bandmates Marian, Danica and Ana (I could write a whole essay for you Ana but I'll just leave it at this, you are my favorite bassist ever thank you for existing). And thank you to the city of Seattle and your amazing local music scene.

When I wasn't in lab I spent a great deal of my time involved in social justice work and organizing with my union, UAW4121, to improve the working conditions for student workers at the University of Washington. In particular, I'm proud of my work with our union to win a contract that provides $0 premium healthcare, including free mental health coverage, and for winning a contract that leads the nation in antiharassment policies and gender affirming healthcare. Thank you David, Sam, Emily, Brian, Nayon and many more people for your work and solidarity. Unfortunately, my years of work in the lab coincided with some very difficult national events and family troubles, and I found myself in a very negative headspace for the middle years of my program. I'd like to thank the UW mental health services for helping me develop methods to deal with stress and work through difficult issues, and I encourage anyone reading this to open yourself up to trying counselling if you haven't yet. And thank you Kurt, Layne, Chris, Chester, and Stuart, your voices are still with me.

I spent 5 months at Argonne National Laboratory on a DOE fellowship before the pandemic shut down the world, but nonetheless those 5 were the best months of science of my whole life. I want to thank the beamline scientists for their friendship and mentorship, thank you Jong-Woo, Gilberto and everyone else. Phil, thank you for all the help getting me here, it's been a real joy working with you, and many more years of collaboration are coming! Thank you Prof. Jian Liu and your group for that first opportunity to travel to Argonne and for the many collaborations. During the pandemic I relocated to Milwaukee to be near family while I wrote my papers and thesis. Thank you Prof. Prasenjit Guptasarma for setting me up with an office at the University of Wisconsin-Milwaukee to work out of, and for inviting me to give talks and join your group meetings, and for always making time to guide me through this experience, I greatly appreciate you. And thank you to Kellie and Patricia for our masked up jam sessions, which was the best part of the lockdown. This thesis was written in about 4 weeks, thank you to the following folks who read and gave feedback on sections and chapters and helped make it a document that I am incredibly proud of: DeStefano, Qianni, Zhaoyu, Paul, Josh, Andre, Connor, Jong-Woo, Gilberto, Mary, Shashi, Jian, Marcel, Anton, Miguel, Prasenjit, and Jiun-Haw.

Finally, I want to dedicate this thesis to the memory of a few people who I wish were around to celebrate my graduation with me, and who have often been in my thoughts recently as I finish this degree. First, Mercile, I'm going to do my best to carry on your work in my own ways, thank you for redirecting me towards this path. Next, my very first childhood friend died of alcoholism in his young adulthood, which is one of several reasons that I no longer drink alcohol myself. Casey, I'm sorry we lost you. Next, one of my best friends in high school died of a brain tumor just a few months before I started grad school. Life is very fragile and should be cherished. Kal I wish you were here so I could entertain you with all the weird facts I've learned in the past 6 years. Next, my grandparents Javier y Natividad Sanchez left Mexico in the middle of their lives to travel to a country they had never been, without knowing the language, to build a better life for their kids. To my knowledge, neither had more than an 8^{th} grade education, and they both worked very hard to support their family taking what work they could get. They both died before I even graduated high school, let alone college or my PhD, and I really wish they could have been here to be a part of my adult life. I dedicate this thesis to them knowing that they did the hardest part to get me where I am today.

Table of Contents

List of Figures

Chapter 1:
Iron-based High-Temperature Superconductors

1.1 Introduction

The explosion of interest in iron-based high-temperature superconducting materials came in 2008 [1] after the discovery of a high superconducting transition temperature (T_c =26K) in doped $La(O_{1-x}F_x)FeAs$ (Fig.1.1). This was particularly surprising because magnetic order is typically antagonistic to classical type I superconductivity, and relatively few Fe-based materials had been known to superconduct at all. Quickly, it was found that several different Fe-based crystal structures yielded superconductivity, including the original 1111 family (e.g. $LaOFeAs$), the 111 family (e.g. $LiFeAs$), the 11 family ($FeSe$), and the 122 family (e.g. $BaFe_2As_2$). Due to the relative ease of growing large high-quality single crystals, as well as having high superconducting transition temperatures, the 122 family quickly took center stage in the study of iron-based superconductors. All of the 122 iron pnictide parent compounds ($RFe_2As_2, R = Ba, Sr, Ca, Eu$) were found to exhibit an antiferromagnetic order, later shown to be a structurally-distorted stripe-type order, with no superconductivity at ambient pressure. Nearly-universally, the suppression of magnetism with hydrostatic pressure or a wide range of electron, hole and isovalent chemical doping series was found to induce superconductivity, leading to general consensus that antiferromagnetic spin fluctuations play a role in mediating this unconventional superconductivity.

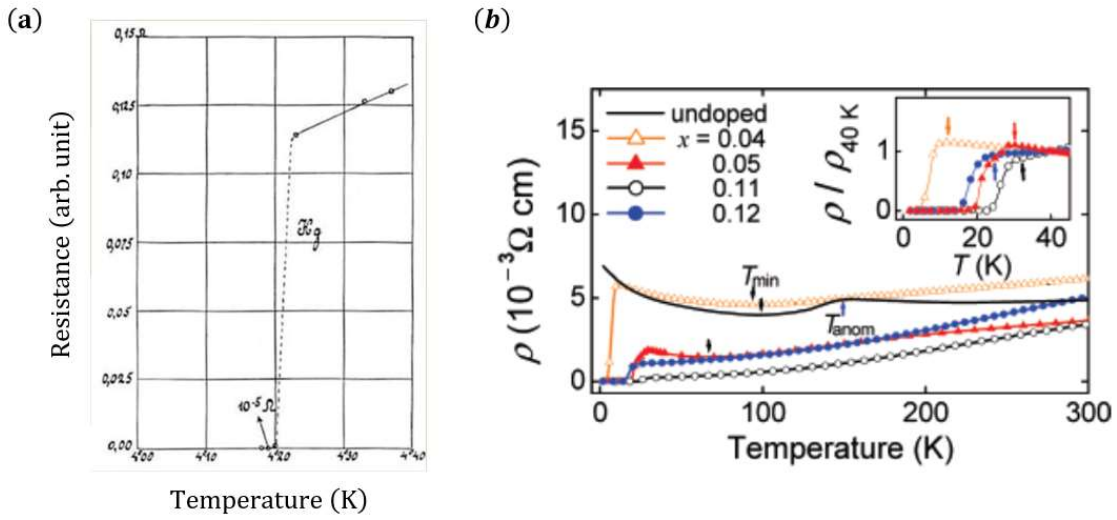

Figure 1.1 Historical resistivity vs temperature plots. (a) The first discovery of superconductivity in mercury (Hg) cooled to liquid helium temperatures. Superconductivity onsets sharply at 4.2K. From the 1911 lab notebook of Karl Ohnnes, reprinted in ref.[2]. (b) The first reported discovery of high-temperature superconductivity in $La(O_{1-x}F_x)FeAs$. All four presented dopings show superconductivity, while the parent compound (black) has a resistivity bump marked "T_{anom}" which was later shown to indicate the onset of nematic order. Adapted with permission from ref.[1] Copyright (2008).

Although the superconducting and magnetic phases drew all of the initial attention, a third phase would come to dominate the discussion of iron pnictide materials. In that same very first report of iron-based high temperature superconductivity, an unknown phase transition in the parent compound was observed from a slope change in the resistivity above the magnetic transition at a temperature labeled "T_{anom}". This phase would later be shown to be an electronic nematic phase[3], in which correlations of conduction electrons lead to a rotational symmetry breaking phase transition with no translational symmetry breaking and no long range magnetic order. This results in a structural orthorhombicity and a large transport anisotropy among other changes. It was found through doping and pressure studies in the 122 system that the transition temperatures for the nematic and the magnetic transitions split such that the former occurs at slightly higher temperature (usually 0K-10K higher) than the latter, creating a narrow band across the phase diagram of a nonmagnetic structurally-distorted phase. For $Ba(Fe_{1-x}Co_x)_2As_2$ specifically (but not exclusively), it appeared that optimal superconductivity occurs in the vicinity of the full suppression of the nematic phase (Fig.1.2), leading to theoretical developments describing a nematic quantum critical point and enhanced superconductivity from nematic quantum critical fluctuations [4].

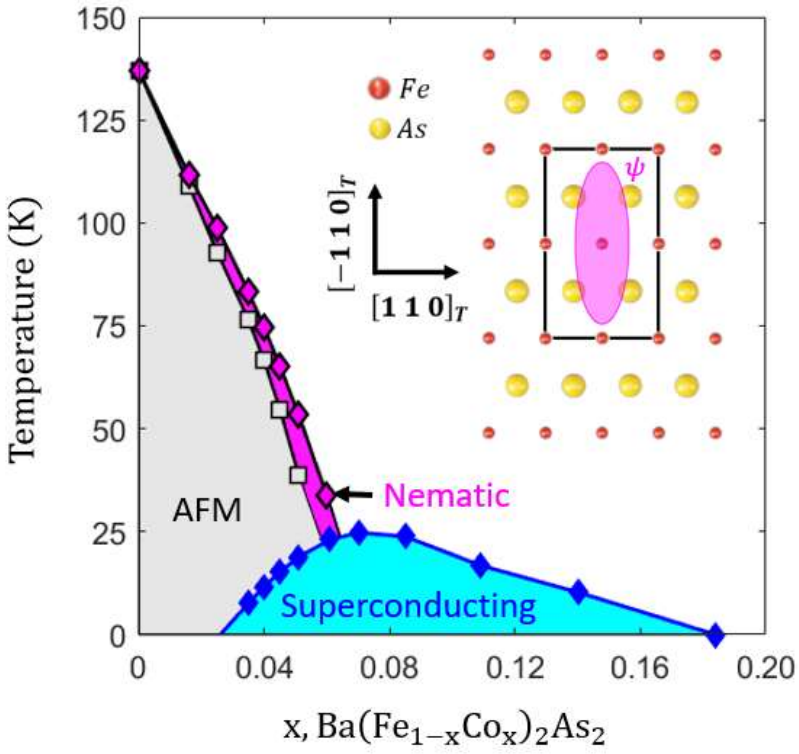

Figure 1.2 *x-T* phase diagram of Co-doped $BaFe_2As_2$. Inset is a representation of the nematic order parameter ψ (magenta) aligned with the in-plane orthorhombicity ε (black) of the FeAs plane within the structurally-distorted nematic phase. From ref.[5].

The precise microscopic description of nematicity remains elusive, and nematicity continues to be studied through its coupling to other quantities such as the resistivity anisotropy and the orthorhombic distortion of the crystal lattice. Through the development of elastoresistivity techniques[6], it was shown that the resistivity anisotropy diverges towards the nematic transition and can be as much as two orders of magnitude larger than the simultaneous structural distortion, which was the original key indicator that the nematicity is driven by conduction electrons. However, transport quantities are not thermodynamic quantities, and a key outstanding question in the study of nematicity even beyond this material system is how well the resistivity anisotropy actually represents the real nematic order.

While $BaFe_2As_2$ is widely regarded as the prototypical iron pnictide material, its structurally identical cousin $EuFe_2As_2$ is arguably the most unique among them [7]. In the undoped parent compound, the same nematic and antiferromagnetic order in the FeAs plane is observed, but below $T_N = 19K$ an A-type antiferromagnetic order is formed by the large Eu magnetic moments. A magnetic field of order 25T applied to $BaFe_2As_2$ can couple to Fe moments and induce a full reorientation (detwinning) of the antiferromagnetic-structural domains; in contrast, a field of only 0.3T applied to $EuFe_2As_2$ can accomplish this same full detwinning due to the highly susceptible Eu moments. This large magnetostructural coupling occurs despite a lack of dipolar coupling between Eu and Fe moments, suggesting the influence of nematic conduction electrons mediating the magnetic interaction. Further, across a variety of doping series the Eu moments can be made to orient ferromagnetically while the FeAs planes exhibit superconductivity. Thus, doped $EuFe_2As_2$ realizes a rare state of matter, a ferromagnetic superconducting state.

1.2 Thesis layout

In this thesis, I expand on our understanding of the relationship between electronic nematicity, magnetic order, the crystal lattice and the electronic transport anisotropy in the Co-doping series of $BaFe_2As_2$ and $EuFe_2As_2$. To do so, I have developed a new method to precisely characterize the transport, structural and magnetic response to applied strain and magnetic field in order to further understand the intertwined nature of these quantities. This method combines simultaneous transport measurements and applied in-situ tunable uniaxial stress of single crystal samples with diverse synchrotron x-ray techniques. I developed this methodology as a user at the Advanced Photon Source (APS) at Argonne National Laboratory during several weeklong beamtimes in 2017-2019, and later during a one-year position at the APS as part of the Department of Energy SCGSR program in 2019-2020. This work has so far led to four papers using this methodology, one which was published in 2020 [8], one which was published in 2021 [5], one which is currently in submission[9], and one which is in preparation, which form the core of this thesis work.

In Chapter 2, I give a quick tour of the phases present in $BaFe_2As_2$, focusing on the phenomenology of each phase and the symmetry breaking of each phase transition.

In Chapter 3, I discuss the mean-field Landau free energy used to describe nematicity thermodynamically. I derive the important structural and transport quantities driven by nematic

fluctuations above the transition and by static nematic order below the transition, as well as the discontinuity in the heat capacity at the transition itself. I present data from several previously published papers supplemented with my own data of these quantities and show that this model not only correctly captures the temperature dependence of each quantity, but that their magnitudes can be related precisely through a new thermodynamic relation I have developed. This work is in preparation as a first-author publication.

In Chapter 4 I give a brief introduction to and present data collected with five x-ray techniques used during my PhD work, including four synchrotron x-ray techniques I used during my stay at the APS. Two of these techniques, x-ray diffraction (XRD) and x-ray magnetic circular dichroism (XMCD) are used extensively in the following chapters.

In Chapter 5 I discuss how a uniaxial stress results in a lattice distortion that can be decomposed into several strain terms belonging to different symmetry channels corresponding to the irreducible representations of the D_{4h} point group. I present three sets of applied uniaxial stress data combined with XRD or XMCD to characterize strain-induced changes in the structural order and magnetic field-induced changes to the magnetic order. I present preliminary data on Co-doped $\mathrm{EuFe_2As_2}$ in which uniaxial tensile stress is shown via XRD to suppress nematicity, resulting in an enhanced superconductivity as indicated by a drastically reduced resistivity. Further, I use XMCD to show that an applied magnetic field can reorient the Eu ferromagnetic moment and enhance superconductivity.

In Chapter 6 I address the question of how well the resistivity anisotropy represents nematicity. To do so, I use a sample of Co-doped $\mathrm{BaFe_2As_2}$ and use simultaneous transport and XRD measurements to characterize the response of the resistivity anisotropy and the lattice to applied uniaxial stress. Through a simultaneous measurement of the nematically-coupled transport and structural quantities above and below the nematic transition, I show that the ratio of nematic-transport to nematic-structural coupling is temperature and phase independent, which demonstrates that for all practical purposes the resistivity anisotropy behaves like a thermodynamic order parameter. This work is the first report of a precise measurement of the resistivity anisotropy in the zero-stress limit of a detwinned sample within the nematic phase.

In Chapter 7 I show that planes of Eu atoms in undoped $\mathrm{EuFe_2As_2}$ have a strongly anisotropic antiferromagnetic interaction, likely due to the influence of nematic conduction electrons. I use uniaxial stress to detwin the sample and hold the sample length fixed to prevent field detwinning. A magnetic field is applied to reorient Eu moments either parallel or perpendicular to the Fe antiferromagnetic easy axis, and the directionally dependent field dependence of the magnetization is measured with XMCD. This work is the first report of the Eu metamagnetic spin flip transition, which is usually masked in a freestanding sample by the rapid field detwinning.

Chapter 2:
Iron Pnictide Phase Transitions, Phenomenology, and Symmetry

This thesis explores several symmetry breaking phase transitions and the coupling of their order parameters to externally applied mechanical stress and magnetic field. To describe these phenomena we use the language of symmetry groups. In this section, I will give a quick tour of the formation of the iron-based superconducting crystals and their various phase transitions. This section focuses on the phenomenology and the symmetry of the transitions, while Chapter 3 discusses the thermodynamic Landau free energy description of the nematic transition in great detail.

2.1 Formation of the crystal

Starting at the very beginning, the electroweak symmetry breaking just after the Big Bang produced a universe-filling amount of hydrogen and helium which eventually condensed into stars of different masses and gave rise to diverse nucleosynthesis processes. The incredibly high-energy core collapse supernova is the exclusive origin of As, while Fe and Co are formed by both core collapse and the lower energy type Ia supernovae which may result from the collision of white dwarf stars. Ba originates primarily from low mass stars slowly burning out, while Eu is mostly produced by cataclysmic neutron star mergers. Therefore, at least 4 distinct astrophysical events needed to occur in the same spatial vicinity for these elements to cooccur in the Earth and form the $\mathrm{Ba(Fe_{1-x}Co_x)_2As_2}$ and $\mathrm{Eu(Fe_{1-x}Co_x)_2As_2}$ crystals studied in this thesis [10]. While the cosmological origin of elements is interesting in its own right, its important in the study of condensed matter physics to keep in mind that the energy of the nucleus is far greater than the energies of bonds between atoms in a crystal, which themselves are greater in energy than the quasiparticles (e.g. phonons, magnons) and phase transition ordering energies (e.g. the superconducting energy gap) that are among the most commonly studied quantities in the field. The large nuclear energies hold the core electrons so tightly bound that for the most part we only really need to consider the behavior of the valence electrons of any atom. Elements with very large positive charge in their nuclei (and thus very large core level energies) are the source of interesting behavior not present in lighter elements. For instance, in lanthanides like Eu, the 4f electrons create large localized magnetic moments, while in heavy transition metals like Ir the 5d electrons exhibit large spin-orbit coupling. These high n orbital states would not be more than barely occupied at cryogenic temperatures or even at thousands of Kelvin without the large nuclei energies.

Next we consider forming a crystal of $\mathrm{BaFe_2As_2}$ by filling a chemically-inert aluminum oxide ($\mathrm{Al_2O_3}$) crucible with a mixture of Ba, Fe and As atoms and heating them to a temperature near 1400K such that the Fe and As atoms form a liquid flux and mix together with the Ba (this is the condition under which the $\mathrm{BaFe_2As_2}$ crystals used in this work were grown; see Chapter 9.1). We can define a coordinate axis with an origin at the center of the crucible. The random motion of the atoms causes the density ρ at any one location $\vec{r}$ to fluctuate wildly at each moment, but over a time average the density is actually constant in every direction, with $\rho(\vec{r}) = \rho_l$. In this state there is both a continuous translational symmetry (no radial dependence of static density) and a continuous rotational symmetry (no angular dependence of static density). This is reflected in the underlying Hamiltonian in which the

interaction between two atoms only depends on the relative distance between them and not on their absolute location in space, i.e. all potential terms between any two atoms have a form $V_{1,2}(\overrightarrow{r_1}, \overrightarrow{r_2}) = V(\overrightarrow{r_1} - \overrightarrow{r_2})$. However, atoms cannot get arbitrarily close to each other without starting to form new bound states by sharing electrons through different bonding processes. From the perspective of any one atom, the density around it does not appear constant due to short range interactions that depend on the energies and symmetries of the highest-occupied valence orbitals. This leads to short range correlations and local spatial arrangement fluctuations that are different for each element as they interact with surrounding atoms (this can be demonstrated by x-ray absorption measurements in the liquid phase). These fluctuations spontaneously happen along every possible rotation axis and at every point of space in the crucible such that no one direction or location is preferred and the time-averaged density still remains totally constant, i.e. the continuous symmetries are preserved. These fluctuations represent the balance between the large kinetic energy and higher entropy of the hot liquid-phase atoms and the interaction energy that groups of atoms can save by arranging themselves in specific patterns.

As the temperature is lowered below the melting temperature, it becomes energetically favorable to form a solid crystal, but this does not happen throughout the whole volume all at once. Instead, in a random small volume of the liquid there occurs a momentarily increased density and decreased temperature where a small number of atoms spontaneously form a stable crystal nucleus. As the temperature is slowly lowered further, more and more material is incorporated as layers around this crystal nucleus, repeating its periodic arrangement of atoms and forming a bulk single crystal. This description is appropriate for supercooled spontaneous nucleation in a flux growth, but nucleation can also occur on the crucible surface or around a doping impurity site, or even on a seed crystal imbedded in the flux, all of which allow diverse methodologies to grow single crystals of varying size and quality (see ref. [11]) . A precise model for the microscopic details of crystal nucleation is still an outstanding problem in condensed matter physics and is a fascinating area of current research [12]. For our purposes in this chapter we can consider the state of the sample once a macroscopic volume has converted into a perfect single crystal.

When the crystal nucleus forms, a random lucky spatial arrangement fluctuation becomes stabilized (frozen), and suddenly a single absolute position and rotation axis is spontaneously chosen for all atoms in the crystal. Now, any single atom has a specific location in space relative to the other atoms which are now at fixed distances and angles from it. From the perspective of the fixed coordinate system, the density is no longer constant but has a discrete radial and angular dependence; thus, the system has experienced a continuous to discrete translational and rotational symmetry breaking. Essentially, any particular location or rotation axis would be equally energetically favorable in terms of the underlying interaction Hamiltonian, and thus equally likely to occur, but as the temperature is lowered below the critical temperature it becomes more energetically favorable to pick a specific location and axis instead of maintaining the higher-symmetry liquid state. This is known as a spontaneous symmetry breaking, and this concept is critical for understanding phenomena as diverse as electronic nematicity, charge and spin density waves, and localized magnetism.

We can describe this phase transition and symmetry breaking mathematically by defining an order parameter, which is a quantity that is zero above a phase transition and nonzero below it and has the same symmetry properties of the new phase. Understanding the symmetries, temperature dependence and external field couplings to order parameters give information about underlying interactions that generate the transitions and are an essential component to this thesis and broadly to condensed matter physics. Crystal formation is a complicated process, and even for the simplest theoretical case of a single element crystallizing, there are multiple order parameters needed to characterize the phase transition [13]. We can write down the density in a form that can describe both the liquid and crystal phases as

$$\rho(\vec{r}) = (1-\eta)\rho_l + \rho_l \sum_n \mu_n e^{i\,\vec{k}_n \cdot \vec{r}}\; e^{i\theta_n}$$

where ρ_l is the density of the liquid phase. Here, η controls the average density between the liquid and nucleated crystal phases and jumps from zero to nonzero at the transition. This is an order parameter which is associated with a change in translational order but not orientational order as it represents how the liquid phase atoms become packed more closely together upon freezing. The μ_n coefficients are the Fourier components of the crystal lattice and describe the amplitude of atomic localization at different lattice sites; they are also zero above the transition and become nonzero below the transition as the crystal lattice forms. These order parameters are associated with the orientational order symmetry breaking of the phase transition via the wave vectors $\vec{k}_n$ that define the spatial scale over which atoms are separated by and define the orientation axis of the crystal. This splitting of the translational and orientational symmetry breaking into different order parameters implies that it may be possible for the two symmetries to be broken at different temperatures, creating an intermediate phase with well-defined orientational order but no translational (positional) order. Indeed, this is observed for instance in the nematic phase of liquid crystals where rodlike molecules order with a net alignment along one direction, spontaneously breaking the rotational symmetry, but still without having fixed relative positions and so maintaining full translational symmetry (note that to define a nematic liquid crystal transition requires rank two tensor order parameters and not just vector or scaler order parameters, discussed in section 2.5). In analogy to nematic liquid crystals, we can also treat nematic conduction electrons as a fluid with a spontaneous orientational order, as discussed later in this chapter.

Returning to the crystal density equation, the μ_n and $\vec{k}_n$ terms define where atoms are located relative to each other, while the phase factors θ_n define where in absolute space each atom is localized. For instance, in a 1-D chain of atoms with a distance a between each atom, $\theta_n = 0$ may correspond to one atom being located at $x = 0$ and all others placed at $x = Na$, while different values of θ_n correspond to the whole chain of atoms being shifted in absolute position along the x axis. When the crystal is formed, a single set of θ_n are chosen even though any value would have an equivalent energy and is equally likely. This result enables a discussion of a subtle phenomenon that marks an essential difference between continuous and discrete symmetry breaking. A continuous-to-discrete symmetry breaking phase transition always results in a zero-energy collective excitation known as a *Goldstone boson*. In this particular case, it costs zero energy to move every atom in the crystal uniformly by the same distance along any one direction, i.e. a change of the continuous phase of the order parameter

costs zero energy. This is a result of the maintained continuous translational symmetry of the Hamiltonian describing the interactions between particles even in the broken translational symmetry phase. However, the displacement of any single atom relative to the others does cost energy in the broken symmetry state. A transition from one discrete symmetry phase to a lower symmetry discrete phase also can be described by the phase of an order parameter, but in this case the phase will have discrete values and a change from one phase to another will in general cost energy. Thus there is no Goldstone boson associated with these discrete-discrete symmetry breaking phase transitions. Experimentally, the major work in this thesis relates to changing the phase and/or the magnitude of nematic and magnetic order parameters by applying stress and magnetic field, and the precise details of how the order parameter magnitudes and discrete phases change with applied field gives key information about the form of the underlying interactions.

As a final note, all of the above discussion relates to the localization of the positively charged nuclei and the closest-held core electrons, and the translational and rotational symmetry breaking relates to these objects. However, in a metallic crystal like $\mathrm{BaFe_2As_2}$ the valence electrons of each atom form metallic bands in which the highest energy electrons delocalize and "hop" between atomic sites; this sharing of electrons effectively holds the crystal together. Relatively small changes in the way these electrons hop can create new phenomena and new phases in a crystal. These are referred to as electronically-driven phase transitions, and four such transitions are under study in this thesis: superconductivity, nematicity, the spin density wave, and localized Eu antiferromagnetism. As this electron hopping is also the process by which an electric current is carried, electric transport measurements are especially sensitive to electronically-driven phase transitions. There is often a transport signature of a phase transition that can be reliably trusted to characterize the transition, such as a change in slope of the temperature dependence of the resistivity or most dramatically as the total loss of resistivity for a superconducting transition.

2.2 Defining the unit cell and its symmetries

We now discuss the structure and symmetry of the fully-formed $\mathrm{BaFe_2As_2}$ crystal. The crystal has the $ThCr_2Si_2$ (122) structure, which can be understood as a stacking of alternating layers of FeAs and Ba sheets (Fig.2.1a). The Fe atoms form a square lattice with As atoms tetrahedrally coordinated at the center of these squares and alternating above and below this plane. These layers are stacked with the above-planar As atoms in one layer aligned with the below-planar As atoms of the next layers, such that two layers together constitute one repeating unit when considering translation along the $\hat{z}$-axis. The Ba atoms form their own planar square lattice with atoms placed collinear to the As atoms along the $\hat{z}$-axis.

We can discuss the symmetries of each atom by assigning them to different point groups, and then discuss the symmetries of the unit cell by determining its point group and space group. The classic text on symmetry groups is ref.[14]. Again, the breaking of these symmetries internally from phase transitions or with externally applied strain and magnetic fields are the core focus of this thesis, and it's worth taking the time to define them in detail. The quick guide for determining symmetries is to perform a symmetry operation (e.g. a rotation, translation or other operation defined by the symmetry group) and check if the crystal has returned to the same initial state.

We first consider a single FeAs plane. In Figure 2.1c-d, it is shown that for a centered As atom there is a four-fold (C_4) rotational symmetry about the $\hat{z}$ axis (the principal rotation axis), while the coordination of As atoms results in only a 2-fold (C_2) rotational symmetry for a centered Fe atom. We can also consider reflections across vertical mirror planes defined from the $\hat{z}$ axis and the Fe-Fe or Fe-As bonding directions. In Figure 2.1c-d it is also clear that the crystal is invariant to both sets of mirror plane reflections when the mirror planes are centered on an As atom, but is only invariant to Fe-As mirror plane reflections when centered on an Fe atom. A Ba atom has the same rotational and vertical mirror plane symmetries as an As atom. Returning to Figure 2.1a, a C_2 rotation about the $\hat{x}$ axis running through a Ba atom leaves the crystal invariant, and likewise for a C_2 rotation about the $\hat{x} + \hat{y}$ axis, but these rotations through the Fe and As atoms do not return the same crystal structure due to the coordination of As and Ba atoms. Next we consider the horizontal mirror plane reflection operation, which takes all points from (x, y, z) to (x, y, -z). This returns the original crystal structure only when the Ba atom is centered. Finally, an inversion operation takes all points from (x, y, z) to (-x, -y, -z), and again this leaves the crystal invariant only when the Ba atom is centered (at these points there is inversion symmetry). From this analysis, we determine the point groups of each atom as such: Ba (D_{4h}), As (C_{4v}), and Fe (C_{2v}), where the number indicates the n-fold discrete rotational symmetry about the primary ($\hat{z}$) axis, the D indicates rotations about the primary axis plus n perpendicular C_2 rotation axes, the C indicates rotations about the primary axis only, the h indicates the horizontal mirror plane reflection symmetry, and the v indicates n vertical mirror plane symmetries only (note that the combination of D and h implies the existence of the vertical mirror plane symmetries) [14], [15].

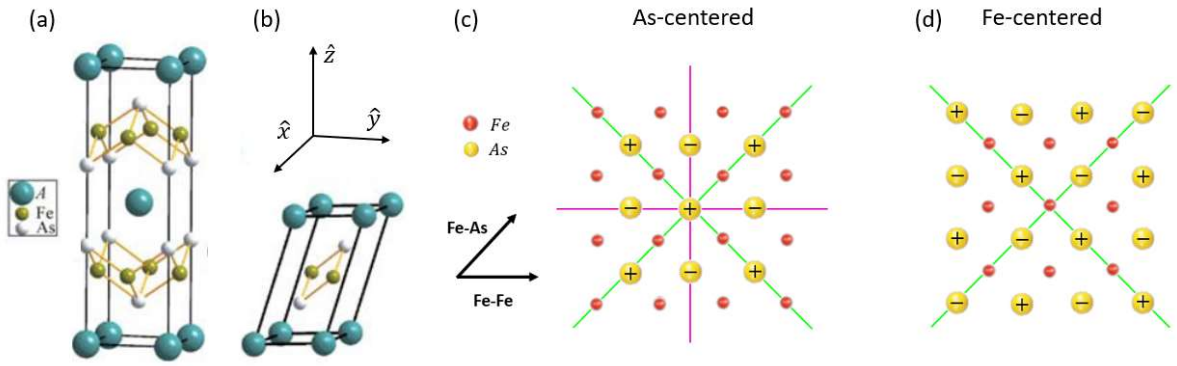

Figure 2.1 (a) Conventional unit cell ($Ba_2Fe_4As_4$), also generally referred to as the tetragonal unit cell and the 2-Fe unit cell (due to 2 Fe atoms in a single $FeAs$ plane). (b) Primitive unit cell ($BaFe_2As_2$). Adapted with permission from ref. [16], Copyright 2010. (c-d) A single Fe square plane with As coordination above and below the plane marked with "+" and "−", respectively. Green (magenta) lines mark mirror planes along the Fe-As (Fe-Fe) bonding directions. A centered As atom is invariant under both sets of mirror plane reflections and has 4-fold rotational symmetry, while a centered Fe atom is only invariant for reflections about the Fe-As bonding direction planes and has only 2-fold rotational symmetry.

Next we construct the appropriate unit cell for $BaFe_2As_2$ which we will use to discuss structural changes from applied stress and from phase transitions. First we can construct the primitive unit cell

which contains one Ba atom, two Fe atoms and two As atoms (Figure 2.1b). This primitive unit cell is the smallest volume unit cell that has the correct chemical stoichiometry of the crystal and has the full translational symmetry; however, as it is a triclinic structure it lacks the rotational and inversion symmetries present in the Ba atom point group [16]. To address this, we can construct a conventional unit cell with the goal of having the highest attainable symmetry when considering the space group, i.e. the full set of translations combined with rotations and other spatial operations under which the unit cell returns to its initial condition. To craft this unit cell with both C_4 and inversion symmetries, we choose a rectangular prism shape and center a Ba atom so that any 90 degree in-plane rotation about the z-axis returns the same crystal structure. The centered Ba atom makes this a body-centered unit cell, and from the inversion symmetry of the Ba atom this central point is known as the inversion center (a lattice with an inversion center is said to be centrosymmetric). With these conditions set, any square-face rectangular prism unit cell with basis vectors along the Fe-As or Fe-Fe bonding directions will also have all 4 vertical mirror plane symmetries shown in Figure 2.1c. Therefore, the whole unit cell has D_{4h} symmetry and belongs to the I4/mmm space group (the I indicates that the unit cell is body-centered) [15], [16]. Further, we can describe this unit cell as having tetragonal symmetry, because the in-plane a and b lattice constants are equal in length and unequal to the out of plane c lattice constant, and the three basis vectors are all perpendicular ($\alpha = \beta = \gamma = 90°$).

With the shape and center of the unit cell determined, we now need to determine the orientation and minimum volume of the unit cell that respects all of the symmetries and capture the essential physics of the system. The unit cell size and orientation will be shown to change at phase transitions and so this warrants a very explicit discussion. Considering a single FeAs plane as seen from above (Fig.2.2a), the obvious first choice is to construct a small square of four Fe atoms around a centered As atom (orange). This is known as the 1-Fe unit cell. However, given the above-below planar coordination of As atoms (+/- signs), the 1-Fe unit cell doesn't actually have translational symmetry, and the translational symmetry breaking potential from these As atoms has been shown to create large changes to the electronic structure [17]. The smallest unit cell that does have translational symmetry is the $45°$ rotated 2-Fe unit cell (black), with in-plane basis vectors $[1\ 0\ 0]_T$ and $[0\ 1\ 0]_T$ along the FeAs bonding direction and with lattice constants a_T and b_T, respectively. In the literature this is usually called the tetragonal unit cell and is mainly considered in the high-temperature nematic-disordered phase. In anticipation of the upcoming discussion, we can also define a 4-Fe unit cell aligned with the Fe-Fe bonding direction (blue) with lattice basis vectors $[1\ 0\ 0]_{Or} = [1\ 1\ 0]_T$ and $[0\ 1\ 0]_{Or} = [-1\ 1\ 0]_T$ and lattice constants $a_{or} = b_{or} = \sqrt{2}a_T$. In the high-temperature phase, all of these unit cells have tetragonal symmetry, but below the nematic transition the 4-Fe unit cell becomes orthorhombic and hence is often called the orthorhombic unit cell [18]. As discussed in section 2.4, the nematic phase is also described by the 2-Fe unit cell (but for convenience is often depicted in the 4-Fe unit cell), while the spin density wave phase must be described the 4-Fe unit cell.

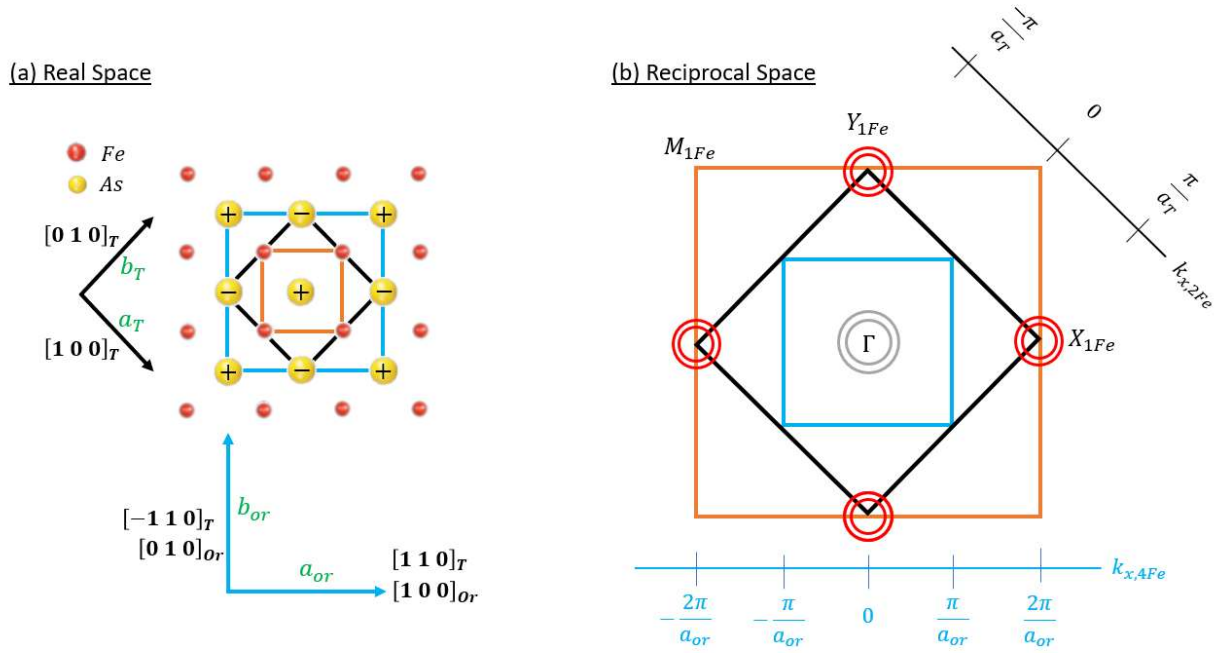

Figure 2.2 $\mathbf{BaFe_2As_2}$ real space and reciprocal space structure in the high-temperature disordered state ($\boldsymbol{T > T_S}$). (a) Real space picture of a single FeAs plane, where + and – signs on As sites indicate coordination above and below the Fe plane. The 1-Fe (orange), 2-Fe (black) and 4-Fe (blue) unit cells are outlined. The 1-Fe unit cell does not actually have translational symmetry, and so the 2-Fe unit cell is used to define the $[\mathbf{1\,0\,0}]_T$ and $[\mathbf{0\,1\,0}]_T$ tetragonal basis vectors, of length $\boldsymbol{a_T}$ and $\boldsymbol{b_T}$ respectively. The 4-Fe unit cell has basis vectors $[\mathbf{1\,0\,0}]_{Or} = [\mathbf{1\,1\,0}]_T$ and $[\mathbf{0\,1\,0}]_{Or} = [\mathbf{-1\,1\,0}]_T$, with lengths $\boldsymbol{a_{Or}}$ and $\boldsymbol{b_{Or}}$ respectively. Below the nematic transition ($\boldsymbol{T < T_S}$), $\boldsymbol{a_T = b_T}$ while $\boldsymbol{a_{Or} > b_{Or}}$. (b) Qualitative schematic of the first Brillouin zone at $\boldsymbol{k_z = 0}$ for the 1-Fe (orange), 2-Fe (black) and 4-Fe (blue) unit cells. Red (grey) circles represent the location of Fermi surface sheets forming two electron (hole) pockets at the 1-Fe X and Y points ($\boldsymbol{\Gamma}$ point).

2.3 Basics of the electronic structure

In the above discussion we have focused on the position of the atoms, meaning really the nuclear ion cores and the tightly-bound core electrons. However, the formation of the crystal lattice is made possible by electronic bands originating from the outermost valence electrons of each element (specifically, the 6s electrons of Ba, the 4s and 4p electrons of As, and the 4s and 3d electrons of Fe). In particular, the Fe 3d orbitals of xz, yz and xy symmetry form bands that cross the Fermi surface and so make the largest contribution to the electronic and magnetic properties [19]–[21]. To directly see the symmetries involved, we switch the discussion to considering the first Brillouin zone of the unit cells. Theory and experiment agree that these bands form sets of hole-like and electron-like Fermi surfaces shaped as warped cylinders along the z-axis and which are open at the top and bottom Brillouin zone

faces (Fig.2.3) [22]. The circular shape of these pockets means the conduction electrons behave more or less like they have continuous in-plane rotational symmetry. The presence of multiple electron and hole surfaces makes $BaFe_2As_2$ a multiband system[23], which also results in a multiband superconducting order, discussed below [24]. $BaFe_2As_2$ is a compensated metal, meaning it has an equal number of electron and hole carriers. This should give rise to a nominal zero value of the normal Hall resistivity, but as the effective masses and the scattering rates are different between the electron band and hole band carriers, there is a substantial nonzero Hall resistivity [25]. In the metallic phase, $BaFe_2As_2$ has features of a "bad metal" such as incoherent hole carriers with a mean-free path length smaller than the lattice spacing [26]. However it still has classic features of a Fermi liquid, such as a resistivity with at T^2 temperature dependence and a high-temperature saturating resistivity[23]. With Co doping the system in one way becomes a better metal as it has increased electron carriers as seen from a larger Hall coefficient [27], but near the optimal doping the resistivity becomes almost perfectly linear to temperature, making it a non-Fermi liquid. For detailed discussions of the band structure and Fermi surface, see refs.[21], [22], [28], [29].

In Figure 2.2b we show a qualitative representation of the $k_z = 0$ slice of the first Brillouin zone. Starting with the 1-Fe unit cell (orange), we find that the bands crossing the Fermi surface create 2 hole pockets at the Γ point and 2 electron pockets at the X and Y points. We note that strictly speaking the X and Y points are equivalent points in the tetragonal phase but become inequivalent below the nematic transition or in the presence of a rotational symmetry-breaking field such as a strain field. Interestingly, there are different symmetries at each point in the Brillouin zone corresponding to the symmetries of different points within the structural unit cell. For instance, the Γ point has a D_{4h} symmetry like the body-centered Ba atom site, while at other points there is lower symmetry (these different symmetries become important to consider in a discussion of topological features of a material). The 2-Fe unit cell is twice as large as the 1-Fe unit cell in real space, and so correspondingly is half as large in reciprocal space. Further, the 45 degree rotation places the electron pockets at the 2-Fe M point. The 4-Fe unit cell is four times larger in real space compared to the 1-Fe and likewise is four times smaller in reciprocal space, such that the electron pockets are outside the first Brillouin zone and are actually at the edge of second Brillouin zone, which we now show has important consequences for the creation of magnetic order.

The Γ point hole pockets and X/Y point electron pockets have a similar size and shape, which gives rise to an electronic phenomena called Fermi surface nesting [29], [30] in which a single q-vector of fixed length and direction can connect many electron states from one Fermi surface to hole states of degenerate energy on another Fermi surface. The collective interaction of these many particles can create large anisotropic fluctuations that drive the system towards a Fermi surface-reconstructing phase transition. In this case, a q-vector of length $|\vec{q}| = \frac{2\pi}{a_{Or}}$ along the $k_{x,1Fe}$ axis connects the surfaces of the X-electron and Γ-hole pockets, with a matching rotated q-vector connecting the Y-electron and Γ-hole pockets. The length of this vector represents the momentum transfer of the interaction and is very important to the physics of this system, as it is actually just the size of the 1-Fe Brillouin zone ($k_{F,1F} = \frac{2\pi}{a_{Or}}$) and so in real space this corresponds to a density wave along $k_{x,1Fe}$ with periodicity a_{Or}. This implies that the Fermi surface nesting will result in the formation of a commensurate spin density wave

that flips its sign between each Fe atom along the Fe-Fe bonding direction. Even above the magnetic ordering temperature, the effect of this nesting is to create a strong antiferromagnetic interaction between spins along the 1-Fe $\hat{x}$ and $\hat{y}$ directions. This creates strong spin fluctuations along these two directions and thus is a leading candidate for the source of the in-plane rotational anisotropy that ultimately impact other electronic and structural quantities.

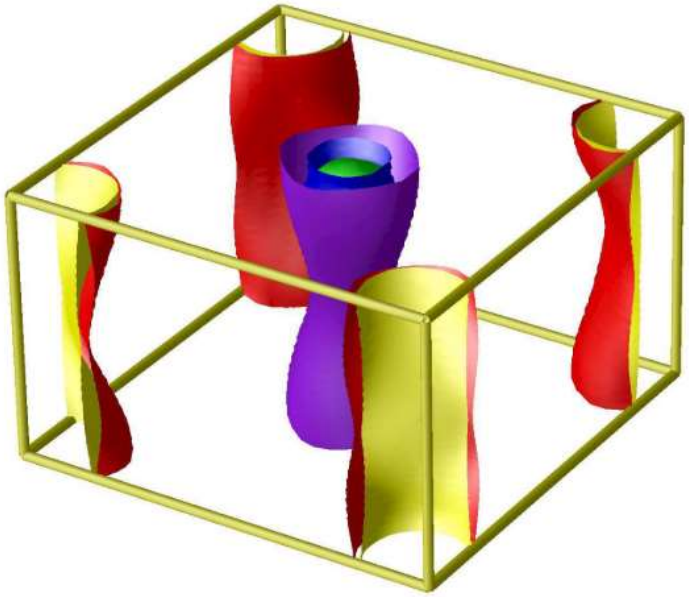

Figure 2.3 DFT calculation of the Fermi surfaces of nonmagnetic overdoped $Ba(Fe_{.90}Co_{.10})_2As_2$ in the 2-Fe first Brillouin zone. Two electron-like surfaces (red, yellow) and three hole-like surfaces (purple, blue, green) extend as warped cylinders along the k_z direction. Adapted with permission from [28] Copyright 2009.

2.4 The nematic and spin density wave transitions

We can now discuss two phases central to this thesis work, the electronic nematic phase and the spin density wave phase. This introduction focuses on the phenomenology and symmetry of the phases because the exact microscopic mechanism of both is still under debate[31], [32]. While a Fermi surface instability towards an itinerant spin density wave phase describes many features of the magnetic order[28], [33], the multiband nature of the Fe 3d orbitals appears to give some local moment character to the magnetism[34], leading to models that use anisotropic nearest-neighbor interactions [35] and/or non-Heisenberg biquadratic interactions [36] between local moments to describe features of the magnetism. Therefore, the Fe moments are not considered to be well described as purely itinerant or localized. However, there is overwhelming evidence that the anisotropy of spin fluctuations plays a

major role if not the central role in understanding nematicity in the 122 iron pnictide materials [37], and so it is necessary to treat the two phases together.

The nematic transition was first understood as a tetragonal-to-orthorhombic structural transition in which the Fe atoms distort from a square lattice to a rectangular lattice (Fig.2.4a). For this brief introduction we can consider a single domain state in which the orthorhombicity is aligned along the $\hat{x}$ axis, with the $\hat{x}$ aligned lattice constant becoming larger than the $\hat{y}$ aligned lattice constant, $a_{Or} > b_{Or}$, with an orthorhombicity value of $\varepsilon = \frac{a_{Or}-b_{Or}}{a_{Or}+b_{Or}}$. Later, it was shown that the nematic phase transport anisotropy was much larger than the lattice orthorhombicity, leading to an understanding of nematicity as an electronically-driven phase in which the structural transition is a mere byproduct of strong electronic interactions [38], [39]. From this, we can define a phenomenological nematic order parameter ψ, where $\psi > 0$ indicates nematic order with a director along the $\hat{x}$ axis (Fig.2.4a) and $\psi < 0$ indicates nematic order with a director along the $\hat{y}$ axis. At the time of writing, the exact microscopic definition of the nematic order parameter in this system is not yet determined, but there is substantial evidence that it is related to strongly anisotropic spin fluctuations that arise in the orthorhombically-distorted unit cell[40], [41], leading to the spin nematic model[3] discussed next. From a material-independent symmetry perspective, a nematic transition can be described as a transition that breaks rotational symmetry but not translational symmetry[42]. In our crystal, this results in the nematic phase being represented by the 2-Fe unit cell with a diagonal distortion (Fig. 2.4a, black). Somewhat confusingly, in the literature the nematic phase structure is often represented with a 4-Fe conventional unit cell to emphasize the square-to-rectangular distortion of the iron atoms; however, a doubling of the real space unit cell would require a translational symmetry breaking that does not occur at the nematic transition. Still, it is convenient to use the 4-Fe cell and this will often be the choice in figures in this thesis, while keeping in mind this nuance.

In this phase, the four-fold (C_4) rotational symmetry is lowered to two-fold (C_2) rotational symmetry and the Fe-As mirror plane reflection symmetry is broken, while the horizontal mirror plane reflection and inversion symmetries are preserved. This gives the nematic phase a total symmetry of D_{2h}, and when using the 4-Fe unit cell it belongs to the space group Fmmm (where the F indicates a face-centered unit cell which occurs from the choice of having Ba atoms occupy all corners of the 4-Fe unit cell)[43]. Within the nematic phase, there is no long range static magnetic order and so time reversal and $O(3)$ spin-rotational symmetries are still present [31], [44]. However, spin fluctuations are found to be strongly enhanced along the nematic axis and suppressed transverse to it [40], which breaks the Z_2 spin symmetry (see ref.[44]). Considering the electronic structure upon entering the nematic phase, the hole pocket at the Γ point is deformed from a circular shape to an elliptical shape along either X or Y, and the 1st Brillouin zone 4-fold rotational symmetry is lowered to a 2-fold rotational symmetry. This electronic structure anisotropy effectively results in a transport anisotropy, but is not necessarily the main source of transport anisotropy, as anisotropic elastic and inelastic scattering (from spin fluctuations or disorder scattering etc.) can also contribute. However, as the size of the unit cell doesn't actually change (no translational symmetry breaking) the Fermi surfaces are deformed (change of shape) but not reconstructed (change of topology, i.e. change in number of electron and hole pockets, and/or change in the size of the first Brillouin zone).

In contrast, the spin density wave (SDW) transition does reconstruct the Fermi surface, resulting in a halved size of the first Brillouin zone and a doubling of the real space unit cell. Within the nematic-phase orthorhombic structural domain, spin fluctuations become much stronger along the long lattice constant axis compared to the in-plane transverse direction, and further increasing the orthorhombicity (via cooling or applied strain) further enhances both the magnitude and the anisotropy of fluctuations. Therefore, the orthorhombic lattice distortion plays a role in stabilizing the SDW transition. The SDW transition can happen within 1K below the nematic transition in the parent $\mathrm{BaFe_2As_2}$ and can be as much as 10K lower at certain Co doping values [45], while in a narrow doping range near optimal doping a nematic transition occurs but no SDW occurs. In this SDW phase, Fe magnetic moments align antiferromagnetically along $\hat{a}_{Or}$ and $\hat{c}$ and ferromagnetically along $\hat{b}_{Or}$. This arrangement of spins is often referred to as a stripe-type antiferromagnet or a C-type antiferromagnet [32] (Fig.2.4b). As mentioned in the introduction of this section, the magnetism in this system has both local and itinerant features and so defies a simple description as a nesting-driven SDW transition. Nonetheless, the SDW transition results in a nesting of the hole and electron pockets, and the 2-Fe first Brillouin zone rotates by 45 degrees and shrinks by half so that the X_{1F} electron pockets coincides with the new 4-Fe Γ point. Structurally, diagonal-adjacent Fe atoms which had been equivalent in the tetragonal and nematic phases become inequivalent by having opposite spin alignment. This results in a doubling of the unit cell (i.e. a translational symmetry breaking), such that the 4-Fe unit cell is the smallest with all correct symmetries. The formation of the SDW order reconstructs the Fermi surface such that the Fermi surface sheets become mostly (but not fully) gapped. This partial gapping results in the SDW state still being metallic while also being magnetic. As this transition does create long range spin order, it breaks time reversal symmetry and the $O(3)$ spin-rotational symmetry [46]. Spins are pseudovectors and are even under inversion, and so this antiferromagnetic alignment actually does still preserve the inversion symmetry as well. The orthorhombic 4-Fe unit cell belongs to the space group Fmmm, but the magnetic order takes the system into the $C_A mca$ magnetic space group [47].

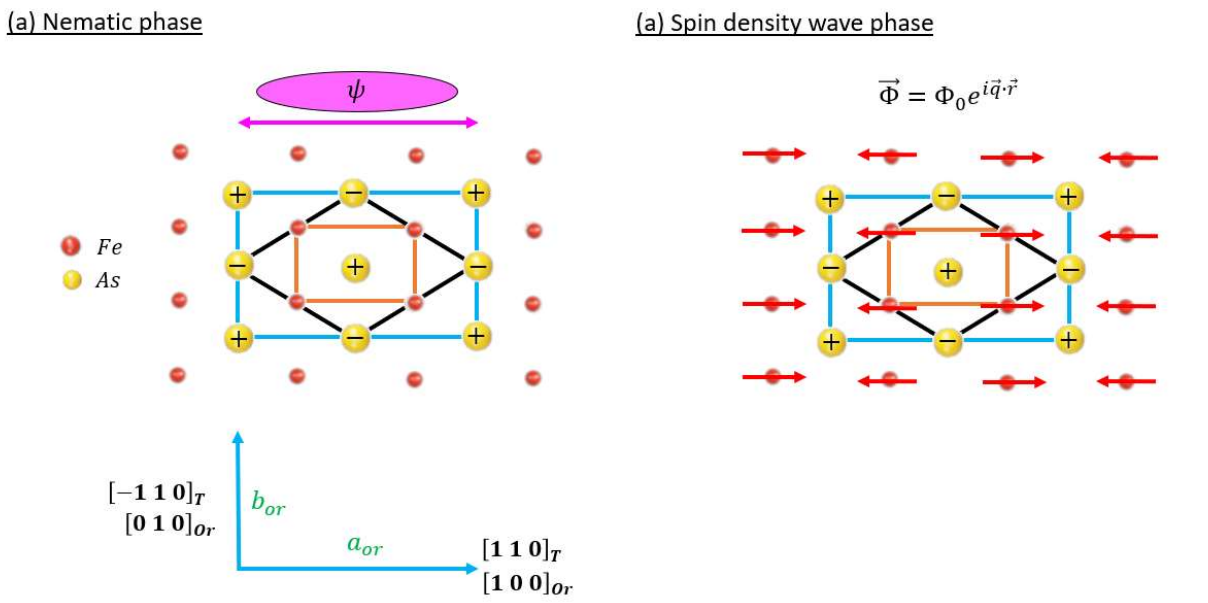

Figure 2.4 (a) Nematic phase and (b) spin density wave phase of $BaFe_2As_2$. (a) the nematic crystal structure for the orthorhombic domain aligned to the $[1\ 0\ 0]_{Or}$ direction ($\hat{x}$), with a representation of the nematic order parameter ψ and its $\hat{x}$-aligned director in magenta. The 2-Fe unit cell (black) is still the correct nematic unit cell, but the 4-Fe is often used for convenience. (b) Spin density wave phase has same orthorhombic structure as the nematic phase and also features a stripe type antiferromagnetic order of Fe spins, with easy axis aligned to the orthorhombic longer lattice constant. To have correct translational symmetry the 4-Fe unit cell must be used.

2.5 Symmetry-breaking order parameters and their fluctuations

We now can define the order parameters of the nematic and spin density wave phases, working in the 4-Fe unit cell coordinate basis. The spin density wave order parameter $\vec{\Phi} = \Phi_0 e^{i\vec{q}\cdot\vec{r}} e^{i\theta}$ has a magnitude Φ_0 (which gives the size of the itinerant Fe moment and is proportional to the energy gap Δ_{SDW} opened by the SDW order), a wavevector $\vec{q}$ (which gives the direction and wavelength of the ordering) and a discrete phase $\theta = n\pi$ (which picks between two antiphase domains, discussed next). Considering the in-plane component, the q-vector can have two directions, either $\overrightarrow{q_1} = (\frac{2\pi}{a_{or}}, 0)$ or $\overrightarrow{q_2} = (0, \frac{2\pi}{a_{or}})$ which orient the antiferromagnetic easy axis along the 4-Fe unit cell $\hat{x}$ or $\hat{y}$ direction, respectively. The SDW order is always aligned with the longer lattice constant of the orthorhombic structural domain, which along with other evidence led to the development of the spin nematic model of iron pnictide nematicity [3], [37], [48], [49] in which the anisotropy of spin fluctuations themselves defines the nematic order parameter ψ.

We sketch out here a basic version of the spin nematic model (see ref.[37] and the supplement of [40] for a more detailed description). We can define Δ_X as a spin density wave order parameter with reciprocal-space propagation vector $(\pi, 0)$, which in real space corresponds to the magnetic moment on each Fe atom aligned along the $\hat{x}$ axis and flipping sign at alternating Fe sites (see Fig.2.4b). Similarly, we can define Δ_Y as the SDW order parameter with reciprocal-space propagation vector $(0, \pi)$, and real space moment alignment along the $\hat{y}$ direction. Above or within the nematic phase, there is no long range magnetic order and the expectation value of each is zero, $\langle \Delta_X \rangle = \langle \Delta_Y \rangle = 0$. However, when considering the instability of the Fermi surface towards the SDW order, there are strong spin fluctuations along the $\hat{x}$ and $\hat{y}$ directions even in the absence of long range magnetic order, which implies $\langle \Delta_X^2 \rangle > 0$, $\langle \Delta_Y^2 \rangle > 0$. Therefore, we can simply define the nematic order parameter as the difference in these expectation values, $\psi \propto \langle \Delta_X^2 \rangle - \langle \Delta_Y^2 \rangle$, with $\langle \Delta_X^2 \rangle = \langle \Delta_Y^2 \rangle$ and $\psi = 0$ above the nematic transition, $\langle \Delta_X^2 \rangle > \langle \Delta_Y^2 \rangle$and $\psi > 0$ below the nematic transition in an $\hat{x}$ oriented orthorhombic domain, and $\langle \Delta_X^2 \rangle < \langle \Delta_Y^2 \rangle$ and $\psi < 0$ below the nematic transition in a $\hat{y}$ oriented orthorhombic domain. These definitions give the nematic order parameter the correct C_2 rotational symmetry observed in the nematic phase. In this mean-field definition, the value of $\langle \Delta_X^2 \rangle - \langle \Delta_Y^2 \rangle$ is taken to be identical at every Fe atom, and so the nematic ordering wavevector is zero, $\vec{q} = 0$. Finally, as ψ can take one of two discrete values, this makes ψ an Ising nematic order parameter (a system in which the nematic order parameter that can have an arbitrary direction in the xy plane is referred to as an XY nematic).

An important subtlety of the nematicity is that the order parameter ψ is defined not as a vector, but as a second rank tensor, and its spatial representation is a **director** which can be drawn as a double-headed arrow with no tail (Fig.2.4a, magenta). This implies that the nematicity generates an anisotropy between the $\hat{x}$ and $\hat{y}$ directions but makes no distinction between $+\hat{x}$ and $-\hat{x}$. Therefore, a vector field (i.e. a first rank tensor field) cannot couple *linearly* to the nematic order parameter but instead can only couple quadratically or in higher even powers of the vector field. A second rank tensor field such as a strain field can couple to the nematic order linearly, but only if it also has the same symmetry as the nematic order; otherwise again it must couple with higher powers. This is discussed in detail in Chapter 5, as the different ways that strains of different symmetry can couple to nematic order is important for understanding how to tune the nematicity. In contrast, an individual spin is a pseudovector that can couple to a (pseudo)vector field, namely an applied magnetic field. The spin density wave order parameter is also a pseudovector, but due to the antiferromagnetic alignment of spins, the coupling to an applied field along the ordering direction is zero, and so an applied magnetic field tends to suppress the spin density wave order by reorienting magnetic moments via canting. As a pseudovector order parameter, the SDW also does distinguish between $+\hat{x}$ and $-\hat{x}$ as well as between $\hat{x}$ and $\hat{y}$. Within a single $\hat{x}$-aligned structural domain, a given stripe can have a spin direction along either $+\hat{x}$ or $-\hat{x}$, and so either of two *antiphase domains* can spontaneously form in the structural domain [50]. To visualize this, consider the SDW-ordered orthorhombic unit cell of Fig.2.4b and flip the head and tail of every spin to create the other antiphase domain. These domains are not often discussed due to their relative inaccessibility, but recent advancement in x-ray resonant magnetic scattering (XRMS) techniques have enabled the direct imaging of antiphase domain boundaries [51]. Finally, the SDW order parameter has

a nonzero ordering wavevector ($q > 0$) while the nematic order parameter (and its associated fluctuations) have a zero ordering wavevector ($q = 0$). This allows nematic fluctuations to couple to superconducting orders of different symmetries and is an important detail in theories of nematic quantum critical enhancement of superconductivity [4].

We can now discuss nematic fluctuations above the nematic transition. Considering again the high-temperature nematically-disordered tetragonal phase, the d_{xz} and d_{yz} -origin bands are equally occupied and the hole pockets at the Γ point have a C_4 symmetry. The lattice constants of the 4-Fe unit cell likewise have an equal length, $a_{or} = b_{or}$. However, anisotropic spin fluctuations aligned to the 4-Fe $\hat{x}$ and $\hat{y}$ directions locally break the C_4 symmetry down to C_2 symmetry in small volumes and for short times before dissociating[52]. As the temperature is lowered towards the nematic transition temperature, these fluctuations grow in strength with a Curie-Weiss (mean-field) temperature dependence, which results in a divergence of numerous measurable quantities such as the shear modulus[43], [46], [53], [54], the elastoresistivity [6], [55], the ^{75}As NMR electric field gradient [52], and the elastocaloric effect [56]. Below the nematic transition, the C_4 symmetry is spontaneously broken to a C_2 symmetry, and all 4-Fe $\hat{x}$ and $\hat{y}$ aligned quantities spontaneously become anisotropic, including in-plane lattice constants[45], the magnetic susceptibility [38], the optical reflectivity (birefringence)[39], [57] and the resistivity [38], [39].

The lowering of the rotational symmetry results in a choice for the nematicity to align along either the $\hat{x}$ or $\hat{y}$ directions. This results in the formation of twin domains, where different volumes of a macroscopic crystal become nematically ordered along the two directions[57]. These domains are in every way identical and only differ by a 90 degree rotation. Considering first a domain with nematic order aligned to the $\hat{x}$ axis of the 4-Fe unit cell (i.e. along $[1\ 0\ 0]_{Or} = [1\ 1\ 0]_T$), the d_{yz}-origin band is slightly lowered in energy and correspondingly more occupied than the d_{xz}-origin band, the electron and hole pockets become elliptical with the long edge along k_x, and the $\hat{x}$ aligned lattice constant becomes larger than the $\hat{y}$ aligned lattice constant, $a_{Or} > b_{Or}$. Now, spin fluctuations become strongly aligned with the x-axis and increase in magnitude strongly with decreasing temperature and the accompanying increasing orthorhombicity. At the SDW transition, these spin fluctuations freeze into long range static magnetic order, and two antiphase domains occur in each of the two structural domains (i.e. 4 total SDW domains across 2 structural domains). With further cooling, the nematic and spin fluctuations actually decrease in magnitude as the static order parameters enhance, until at base temperature both the nematic and SDW order parameters achieve their maximum saturated value. With this overview of the electronic nematic and spin density wave orders complete, we finish out this introduction with a discussion of the superconducting transition.

2.6 Unconventional Superconductivity

Essentially, a superconductor can be thought of as a charged superfluid which results from the formation of an electron condensate made from the bound states of pairs of electrons called Cooper pairs. The symmetry of this pairing process determines the symmetry of the superconductor, which is the main focus of this section. Before discussing the details of this pairing symmetry, I will make a quick digression into the classification of superconductivity as a phase transition following refs. [58], [59].

It is commonly said that a superconductor breaks gauge symmetry. The root of this concept is due to the form of the complex BCS superconducting order parameter $\Delta_0 = |\Delta_0|e^{-i\phi}$, which has a magnitude $|\Delta_0|$ representing the (real) energy gap (i.e. the energy reduction from forming the condensate) and a phase $\phi(\vec{r})$ which is spontaneously chosen upon entering the superconducting state. In BCS theory, this phase has a specific coupling to the electromagnetic field such that when the electromagnetic vector potential undergoes a gauge transformation as $A_\mu \rightarrow A_\mu + \partial_\mu \alpha$ the phase transforms as $\phi \rightarrow \phi + 2e\alpha$. Two concepts now appear to be in conflict. First, according to Maxwell electromagnetism, any choice of gauge refers to the same physical system, i.e. there is gauge invariance. Second, an order parameter must refer to a specific spontaneously-broken symmetry state such that a specific value of ϕ defines a specific value of Δ_0 and describes a single physical state. Therefore, it would seem that making an arbitrary change of gauge would change the order parameter and thus the physical state of the system. To reconcile these two concepts, one could posit that upon entering the superconducting state a specific value of ϕ is attained and gauge invariance is "broken", such that you can no longer make an arbitrary gauge change. However, this discussion has left out the influence of the electromagnetic field, which has a specific form of coupling to ϕ. When taking this coupling into account, a gauge transformation actually does not result in a change to any physical observables, and so effectively any choice of gauge results in the same quantum state. To be clear, ϕ is useful for describing the behavior of the system; for instance, a supercurrent can be represented by a gradient of ϕ induced by an electromagnetic field. The better interpretation of ϕ is just that every possible gauge-transformed value of ϕ is an equivalent description of the same quantum state as long as the electromagnetic field is also transformed equivalently. For this reason, "gauge symmetry breaking" is something of a misnomer [58]. What's more, as the BCS order parameter is complex it doesn't actually represent a real physical observable, and only the magnitude can actually be measured. A more modern treatment of superconductivity identifies superconductivity as a topological phase and not a symmetry-breaking phase [59]. One way to understand this is that all spontaneous symmetry breaking transitions result in a *local* order parameter, which means that in a macroscopic sample, different local volumes will choose to break the symmetry in different ways resulting in the formation of domains, such as the nematic structural domains or the SDW antiphase domains. In contrast, the above-defined BCS order parameter results from an all-space integral and so is actually a globally-defined order parameter, i.e. it requires knowledge of both the bulk and the edges of the system as all topological phases do. Thus, in a macroscopic superconducting state and in the absence of any applied electromagnetic fields there is a single uniform superconducting order.

Now we return to the iron pnictides and the symmetry of the pairing mechanism that leads to the superconductivity. As the superconducting order parameter varies in phase through real space, it also varies across the 1st Brillouin zone and can take specific values at the different Fermi sheets. In classical s-wave superconductors (Fig 2.5a), the electron-phonon interaction causes an effective attraction between electrons, resulting in a superconducting energy gap Δ_0 with the same sign everywhere in reciprocal space. In contrast, superconductivity in the iron-based materials is widely thought to result from a *repulsive* interaction between electrons at the Fermi surface. The trick here is that if the sign of the superconducting order parameter flips between the hole and electron Fermi surface sheets, then the repulsive interaction also gets a sign flip, and a net attractive interaction results.

This is referred to as an s^{+-} pairing symmetry. Early investigations of the band structure of doped $BaFe_2As_2$ indicate that exactly this kind of sign flipping is possible, with positive Δ_0 at the Γ point hole pockets and negative Δ_0 at the X/Y pockets (Fig. 2.5d) [28]. This multiband anisotropic pairing mechanism has similar features to the other classes of high-temperature superconductors, such as the cuprates with a single-band d-wave symmetry (a sign change across a single Fermi sheet) and MgB_2 with two-band s-wave symmetry (two Fermi sheets with the same sign of Δ_0) [60] (Fig. 2.5b,c).

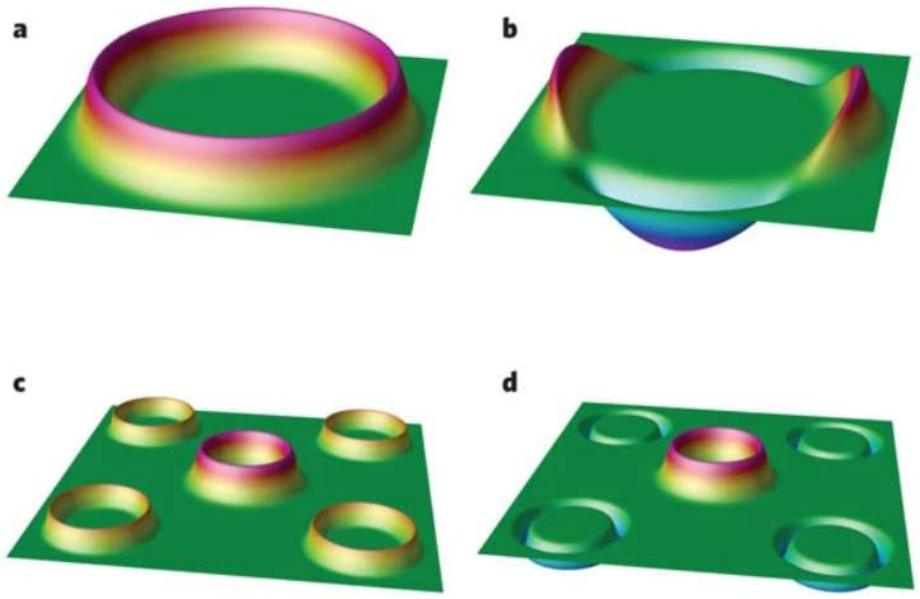

Figure 2.5 Four symmetries of superconducting energy gaps, represented in reciprocal space. (a) single band s-wave symmetry as found in many classical superconductors such as aluminum. (b) single band d-wave symmetry as found in cuprate superconductors. (c) two band s-wave symmetry as found in MgB2. (d) two band $s^{\pm}$ symmetry as expected for iron-based superconductors. In all cases, the height of the 'rubber sheet' is proportional to the magnitude of the order parameter (including its sign). Adapted with permission from [60] Copyright 2010.

For our $BaFe_2As_2$ crystal, the wavevector connecting the Γ and X/Y pockets for superconducting pairing is exactly the same as the Fermi nesting vector that plays a role in forming the spin density wave. Thus, electrons at the Fermi level need to make a choice between whether to order magnetically or superconductively. This competition can be seen from the evolution of the transition temperatures (T_N and T_c) for the two phases. For the parent compound $BaFe_2As_2$, electrons develop a SDW order with a large Fe magnetic moment of about $0.9\mu_B$ [32]and shows no indication of superconductivity down to 2K. This implies that the SDW order decreases the system energy more than the SC phase. However, it has been shown through very many doping series that this relative difference in ordering energies can be tuned by chemical doping [20]. We here consider the Co-doping series ($Ba(Fe_{1-x}Co_x)_2As_2$), where we can consider replacing some percent of Fe atoms with Co (see Fig.1.2). With increasing Co-doping, the

SDW transition temperature T_N gradually decreases, and between 3% and 5.5% Co-doping superconductivity appears at low temperature below the SDW transition[27]. In the range 5.5%-6.8% Co-doping, the SDW phase disappears completely, and superconductivity appears below the nematic transition temperature. The superconducting transition temperature monotonically increases up to about 6.8% Co-doping (the "optimal doping"). Beyond the optimal doping, the nematic phase disappears and T_c decreases, and eventually superconductivity also disappears near 12% Co-doping. Besides the comparison of transition temperatures, the competition between the phases can be seen directly in that the onset of superconductivity actually reduces the magnetic moment size of the SDW order [61]. This is somewhat unexpected as antiferromagnetic order generally persists in a classical superconductor [62]. Even more surprising, for dopings with only a nematic phase and no spin density wave order, the onset of superconductivity also reduces the orthorhombicity and so effectively suppresses the nematic order as well [63]. Finally, the use of both tensile and compressive applied stress has been shown to enhance the orthorhombicity (and thus the nematicity) while suppressing the superconductivity in underdoped Co-doped samples [8].

From these observations it is clear that superconductivity competes for the same electrons that create the nematic and spin density wave phases. For this exact reason, it becomes very important to understand this nematic phase and its associated nematic fluctuations in the high temperature phase in order to gain more insight into the unconventional superconductivity of iron-based high-temperature superconductors.

Chapter 3:
Thermodynamic Nematicity and the Landau Free Energy

This chapter introduces the formalism of Landau continuous phase transitions and how it has been applied to the iron pnictides to make predictions about the magnitude and/or temperature dependence of quantities like the heat capacity, shear modulus, structural orthorhombicity, and enhanced nematic transition temperature. I have a paper in preparation for publication which develops a new relation between the above 4 quantities using this formalism, and the second half of this chapter describes combining published data from several papers confirming the numerical accuracy of this new relation. Beyond this new paper, the results of this section lay an essential foundation for understanding the results of the following chapters as it describes the phenomenological nematic-elastic coupling.

3.1 Introduction

In 1937, Lev Landau published a paper titled "On the theory of phase transitions"[64], which approached the problem of continuous thermodynamic phase transitions by considering the formation of a symmetry-breaking order parameter. In this theoretical framework, we define a phenomenological order parameter which is zero above the transition and becomes nonzero below the transition. This order parameter need not have an exact microscopic description; instead, all it needs is to have the same symmetry properties as the ordered state. This allows for a symmetry-focused thermodynamic description of phase transitions which can be used to make specific predictions about such quantities as the temperature dependence of both the order parameter fluctuations above the transition and the onset of order below the transition, as well as the shape of the heat capacity through the phase transition. It also allows for other quantities of the same or different symmetry to couple to the order parameter and induce other changes to the system; one such quantity is the **conjugate field** which couples linearly (at lowest order) to the order parameter and can enhance or suppress it.

A familiar example of an order parameter is the net magnetic moment in a ferromagnet, which is zero in the high-temperature disordered phase and becomes nonzero below the ferromagnetic transition temperature. In addition to breaking time reversal symmetry, the continuous spin rotation symmetry present in the disordered phase is also broken, as a single direction is spontaneously chosen for the net magnetic moment to point in. In an isotropic Heisenberg spin Hamiltonian, any given direction would have been equally energetically favorable for the moments to align along, and so the ordered phase exhibits lower symmetry than the underlying Hamiltonian. This is an example of a continuous to discrete transition, and so it results in a zero-energy (long-wavelength) Goldstone boson, which for this case is a spin rotation operation. A rotation of all spins by the same angle costs zero energy, which is a major reason why a uniform applied magnetic field can easily reorient a ferromagnetic moment in materials without significant symmetry-breaking magnetocrystalline anisotropy.

Another class of order parameters result from a transition from a higher to lower discrete symmetry state. One example is a tetragonal to orthorhombic structural transition. For a high-temperature tetragonal unit cell with in-plane lattice constants a_x and a_y and out of plane lattice constant c_z, and assuming $a_x = a_y < c_z$, the structural transition results in a relative change of a_x and a_y such that the orthorhombic unit cell has either $a_y < a_x < c_z$ or $a_x < a_y < c_z$ (in this section we will refer to these two cases as the A domain and the B domain, respectively, see Fig.3.1). For this structural transition, the order parameter is the orthorhombicity, $\varepsilon = \frac{a_x - a_y}{a_x + a_y}$. A key point to emphasize is that from the form of ε it is clear that the order parameter is sensitive to the $\hat{x}$ and $\hat{y}$ directions but not to the $\hat{z}$ direction. More technically, it is defined to be within the same symmetry channel as the rotational symmetry which is broken by the structural transition. Within the tetragonal phase, the in-plane rotational symmetry is conserved and so $\varepsilon = 0$. Below the rotational symmetry-breaking structural transition, ε spontaneously becomes nonzero and the system chooses between either $\varepsilon > 0$ and $\varepsilon < 0$. Indeed, for a macroscopic sample, different choices will be made in different local volumes of the sample such that both the A and B domain form with equal probability. This results in the phenomena of "twinning", where a sample cooled below a structural transition forms structural domains. As a note, since this is not a continuous to discrete transition, it does not exhibit a Goldstone boson, which means that it does cost energy to change the A domain to the B domain and vice versa. This domain swapping is accomplished for instance by applying a stress h along the $\hat{x}$ or $\hat{y}$ axis to directly change the values of the lattice constants. This should not be confused with the concept of a "continuous phase transition", which simply means that ε changes from zero to nonzero continuously at the transition temperature.

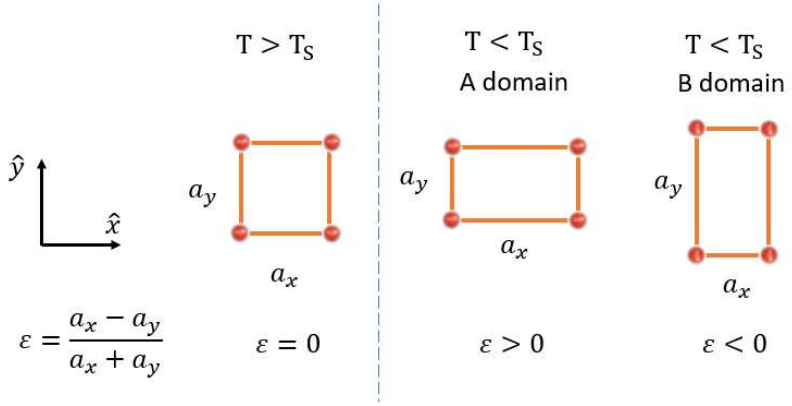

Figure 3.1 The square lattice above the structural transition and the two orthorhombic domains below the transition.

To describe the continuous formation of a nonzero order parameter, Landau developed a theory which defined a free energy density (now named the Landau free energy) in a power expansion of the order parameter. He reasoned that for temperatures very close to the transition, the order parameter will be zero or arbitrarily small, and the key details of the behavior of the system can be understood from just the lowest order terms of the order parameter. From symmetry and stability arguments, he could also remove certain terms and define the sign and temperature dependence of the relevant

coefficients. For our purposes here, we use the most straightforward form of the Landau free energy, which only includes the quadratic and quartic powers of the order parameter. Again, this is not to say that the underlying Hamiltonian includes terms that are quadratic and/or quartic in any quantity, but only that thermodynamically the order parameter can be expressed effectively in this way near the transition. Importantly, the defined quantity is really a free energy *density* (i.e. units of energy per volume) and it is assumed that this free energy density is the same in every unit cell of the crystal. Further, it is assumed that the experienced local fields are identical for every unit cell, so that each unit cell can be considered to have the same value of order parameter everywhere in space. This makes the Landau free energy (density) a mean-field theory.

3.2 The nematic free energy

We now discuss the nematic free energy which as defined below is appropriate for discussing a second-order continuous nematically-disordered to nematically-ordered phase transition. We could also explicitly include terms to capture the physics of the spin-density wave transition and/or the possibility of a first-order nematic transition all in one model (see e.g. [65] and the supplement of [66]), but this is unnecessary for the work in this thesis. Here, the thermodynamic nematic order parameter ψ is treated as a phenomenological quantity with no direct connection to the microscopic interactions that create it. We continue to discuss the nematic transition as a tetragonal to orthorhombic structural transition as above and keep the same definition of the structural order parameter ε, with the main difference being that the nematicity drives the transition and the nematic-elastic coupling then causes the structural transition; this is referred to as a pseudo-proper ferroelastic transition [43], [67]. Hence, ψ is considered to be the primary order parameter, and ε is the secondary order parameter. In this case, ψ an "Ising nematic" order parameter as it has 2 possible values, $\psi > 0$ and $\psi < 0$, just like for ε. Both order parameters belong to the same symmetry channel which allows them to be linearly coupled, and we define λ as the linear coupling energy density between the two order parameters (See Chapter 5 for a discussion of nematic coupling to strains of different symmetries). Just as for ψ we do not make a microscopic description of λ, though different microscopic models can be used to describe how nematic fluctuations couple to the lattice (e.g. [53]). Experimentally, we do not have access to the true thermodynamic conjugate field to the nematic order parameter as we cannot even definite it without defining ψ microscopically. Therefore, we can treat ε as an effective conjugate field to ψ through the linear coupling term $\lambda\psi\varepsilon$. This high-utility term will be used both to determine nematic-driven changes to structural quantities and strain-induced changes to the nematicity. We also include the applied stress h as the conjugate field for ε and note that it can only interact with ψ indirectly through its coupling to ε. Finally, we can write down the free energy as

$$F = \frac{a_0\,(T - T^*)}{2}\psi^2 + \frac{b}{4}\psi^4 + \frac{C_{66,0}}{2}\varepsilon^2 - \lambda\varepsilon\psi - h\varepsilon\,.$$

Here, T^* is the "bare" nematic transition temperature, meaning the temperature at which the nematic transition would attain with zero nematic-elastic coupling, while a_0 and b are phenomenological free energy parameters associated with nematicity; again, a_0 and b are not assigned a microscopic description. The only purely-structural energy density term is the "bare" shear modulus $C_{66,0}$, which is

the material-dependent value of the shear modulus in the absence of nematic coupling. For very overdoped $Ba(Fe_{1-x}Co_x)_2As_2$ samples with very weak nematic fluctuations, $C_{66,0}$ is roughly temperature independent, implying that this crystal structure does not have a significant phonon-driven softening in this channel [68].

We can solve this equation to extract the temperature-dependent behavior of several quantities, including the ordered-phase nematic and structural order parameters and the disordered-phase shear modulus. We can also get information about nematic fluctuations by deriving the *nematic susceptibility*, discussed in detail below. The linear nematic-elastic coupling causes an enhancement of the nematic-structural transition temperature (from T^* to T_S), and at the transition itself there is a jump in the heat capacity which can be expressed in terms of other free energy parameters as well. We will work through the derivation of all of these quantities in the next section. In the following section, we will do a comparison between experiment and theory and show that measured data of all of the above-named quantities agree with each other surprisingly well within this framework for underdoped $Ba(Fe_{1-x}Co_x)_2As_2$ samples.

3.3 The nematic order parameter and nematic fluctuations

We begin by considering the effects of nematic fluctuations in the high-temperature disordered phase. In this phase, there is no static nematic order ($\langle\psi\rangle = 0$), but the nematic order parameter can spontaneously become nonzero for short periods of time such that $\langle\psi^2\rangle > 0$; this is a nematic fluctuation. In the thermodynamic description, it is common to take advantage of the fluctuation dissipation theorem in order to discuss the magnitude of spontaneous fluctuations of an order parameter in terms of the susceptibility of that order parameter to an applied field. We first define the "bare" nematic susceptibility, $\chi = \frac{1}{a_0(T-T^*)}$. This quantity describes how strongly the nematicity would respond to an applied "true" nematic conjugate field, which we lack access to. However, due to the linear nematic-elastic coupling this susceptibility becomes coupled to the lattice, resulting in the "strain" susceptibility $\frac{d\psi}{d\varepsilon}$. In this thesis we will refer to $\frac{d\psi}{d\varepsilon}$ simply as the *nematic susceptibility*, because in practice we always use applied stress to probe $\frac{d\psi}{d\varepsilon}$ and do not have access to χ. We can solve for $\frac{d\psi}{d\varepsilon}$ by minimizing the free energy first with respect to ψ and then to ε and taking the $\psi = 0$ limit:

$$\frac{d\psi}{d\varepsilon} = \lambda\chi = \frac{\lambda}{a_0(T - T^*)}.$$

From this result we see that the nematic susceptibility has a Curie-Weiss temperature dependence and diverges towards the "bare" nematic transition temperature T^* *and not* to the actual structural transition temperature T_S (derived below). This is an important point because a measurement of the susceptibility using a methodology that controls the strain directly (e.g. the modified Montgomery method and applied biaxial strain, as commonly used in elastoresistivity measurements [55]) probes the dynamics of nematicity and not the lattice-coupled dynamics. To make this point clearer, we could consider determining the "stress" susceptibility $\frac{d\psi}{dh}$ by minimizing the free energy first with respect to ψ and then to h and taking the $\psi = 0$ limit:

$$\frac{d\psi}{dh} = \frac{\lambda}{a_0 C_{66,0}(T - T_S)}.$$

The presence of the shear modulus as well as the (nematic-elastic coupling enhanced) structural transition temperature T_S indicates that a stress-tuning methodology probes the nematic-elastic coupled dynamics and not the purely nematic dynamics.

A further consequence of the nematic-elastic coupling is the divergence of the renormalized shear modulus C_{66}, which we obtain by minimizing the free energy with respect to ε and then to ψ and using $\frac{dh}{d\psi} = \frac{d\varepsilon}{d\psi}\frac{dh}{d\varepsilon} = \frac{C_{66}}{\left(\frac{d\psi}{d\varepsilon}\right)}$, resulting in

$$\frac{dh}{d\varepsilon} = C_{66} = C_{66,0} - \lambda\frac{d\psi}{d\varepsilon} = C_{66,0}\left(1 - \frac{\lambda^2}{a_0 C_{66,0}\,(T - T^*)}\right)$$

Essentially, the nematic fluctuations soften the lattice such that a small applied stress yields an increasingly large lattice distortion on approach to the nematic transition temperature. This process enables measurement of the temperature dependence of $C_{66,0}$ to extract T^*. The softening of the shear modulus towards $C_{66} = 0$ enables an infinitesimal stress to induce a stable lattice distortion, resulting in the onset of the nematically-driven structural phase transition. We see that $C_{66} = 0$ when the term in parentheses equals zero, and this is found to occur not at T^* but at an enhanced structural transition temperature T_S, with the enhancement ΔT given by:

$$\Delta T = T_S - T^* = \chi = \frac{\lambda^2}{a_0 C_{66,0}}\ . \qquad (3)$$

From this result it is clear that the lattice acts as a polarizable medium for the nematic fluctuations, not dissimilar to how a paramagnetic medium can be polarized by an embedded magnetic moment. By comparing the divergence temperature T^* and the actual attained structural transition temperature T_S, and with knowledge of the high-temperature value of the shear modulus $C_{66,0}$, one can ascertain the value of the ratio $\frac{\lambda^2}{a_0}$ which will be used in the next section. We note that for $\mathrm{Ba(Fe_{1-x}Co_x)_2As_2}$, ΔT is often found in the range 20K-50K depending on the experimental probe used, but in other materials described by this pseudo-proper ferroelastic formalism it can be significantly larger, for instance up to 230K in $\mathrm{BiVO_4}$ [69].

Having defined the nematic-structural transition temperature, we now derive the temperature-dependent values of the order parameters in the ordered phase. As these order parameters become spontaneously nonzero, we use an "s" subscript to denote their zero-stress value, taking $h = 0$ for the rest of this section. We start by considering some temperature within the nematic phase where the nematic order parameter ψ_S and the (spontaneous) orthorhombicity ε_S are already nonzero. Minimizing the free energy with respect to ε yields the magnitude of the orthorhombicity, $\varepsilon_S = \frac{\lambda}{C_{66,0}}\psi_S$. In words, this equation shows that the size of the structural order parameter driven by the nematic order parameter depends on the balance between the nematic coupling to the lattice and the stiffness

of the lattice, an idea we will return to shortly. Subbing $\varepsilon = \frac{\lambda}{C_{66,0}}\psi$ into the free energy and minimizing with respect to ψ, we obtain

$$\psi\left[a_0\left(T - T^* - \frac{\lambda^2}{a_0 C_{66,0}}\right) + b\psi^2\right] = 0$$

As the second term in the brackets is always positive (since $b > 0$ is required for stability), we find ψ may only have a nonzero value for $T < T^* + \frac{\lambda^2}{a_0 C_{66,0}} = T_S$, which is an alternative route to identify the value of the structural transition temperature. After solving the bracketed equation in terms of ψ, we find that the zero-stress spontaneous nematic and structural order parameters grow with a mean-field temperature dependence as

$$\psi_S = \sqrt{\frac{a_0}{b}}(T_S - T)^{\frac{1}{2}}$$

$$\varepsilon_S = \frac{\lambda}{C_{66,0}}\psi_S = \tilde{\varepsilon}\,(T_S - T)^{\frac{1}{2}}$$

$$\tilde{\varepsilon} = \frac{\lambda}{C_{66,0}}\sqrt{\frac{a_0}{b}}\,.$$

Here we choose to define the magnitude of the orthorhombicity $\tilde{\varepsilon}$ explicitly because a measurement of ε using x-ray or neutron diffraction can only yield its magnitude and the temperature dependence, which alone cannot separate out the magnitude of the nematic order parameter ($\psi = \sqrt{\frac{a_0}{b}}(T_S - T)^{\frac{1}{2}}$) from its proportionality to orthorhombicity $\left(\frac{\lambda}{C_{66,0}}\right)$, nor can it assess the enhancement of the transition temperature ΔT. However, $\tilde{\varepsilon}$ is a second measurable quantity which depends precisely on a_0, b, and λ, which we can combine with ΔT as discussed next. Importantly, a precise measurement of the temperature dependence of the orthorhombicity just below the nematic transition can be used to determine the critical exponent of the transition, which in a mean-field treatment must be $\frac{1}{2}$. As we will show, the critical exponent is indeed very close to $\frac{1}{2}$ within experimental uncertainty for a range of Co-doping values of underdoped $Ba(Fe_{1-x}Co_x)_2As_2$, further validating this mean-field thermodynamic description of the phase transition.

With the thermodynamic order parameters and susceptibilities determined, we can briefly introduce the (non-thermodynamic) transport coefficient of the same symmetry channel, the resistivity anisotropy $\eta = \frac{\rho_{xx} - \rho_{yy}}{\rho_{xx} + \rho_{yy}}$, which is assumed to be linear coupled to the nematic order parameter as $\eta = k\psi$. Given this coupling, we can determine analogous transport quantities for the spontaneous nematic order parameter, here named the spontaneous resistivity anisotropy, $\eta_S = k\psi_S$, and the nematic susceptibility $\frac{d\eta}{d\varepsilon} = k\frac{d\psi}{d\varepsilon}$, which in the zero stress limit is equivalent to the $2m_{66}$ elastoresistivity coefficient, i.e. $2m_{66} = \frac{d\eta}{d\varepsilon}|_{\varepsilon=0}$.

3.4 Thermodynamic equivalence between heat capacity and nematic pressure

We now have the opportunity to reformulate the Landau free energy in terms of purely nematic or purely structural quantities. This reformulation method and its relation to the heat capacity is an original idea of mine that is at the heart of one of my currently in-preparation papers. Here is how it works. Within the nematic phase, we can use the mean-field spontaneous nematic order parameter and the linear proportionality of nematicity to orthorhombicity ($\varepsilon_s = \frac{\lambda}{C_{66,0}}\psi_s$) to rewrite the free energy as

$$F(T < T_S) = -\frac{a_0^2}{4b}(T_S - T)^2 = -\frac{C_{66,0}\tilde{\varepsilon}^2}{4\Delta T}(T_S - T)^2 \quad .$$

The magnitude of the first form depends only on the purely nematic parameters of the free energy, a_0 and b, which are not directly measurable, while the magnitude of the second form depends on $C_{66,0}$, $\tilde{\varepsilon}$ and ΔT which can all be directly measured. Importantly the magnitudes of both forms are unaffected by coupling to the lattice, as the λ term only appears in the enhanced transition temperature and not in the magnitude.

In a second order phase transition, the entropy S is continuous at T_S but its temperature derivative undergoes a discontinuous jump $\Delta\left(\frac{dS}{dT}\right)_{T_S}$ which can be seen directly from comparing the second temperature derivative of the free energy above and below the transition. This is directly measurable as an equivalent jump in the heat capacity ΔC_V, normalized by T_S, which yields the central theoretical result:

$$\Delta\left(\frac{dS}{dT}\right)_{T_S} = \left(\frac{d^2F}{dT^2}\right)_{T_S^+} - \left(\frac{d^2F}{dT^2}\right)_{T_S^-} = \frac{\Delta C_V}{T_S} = \frac{C_{66,0}\tilde{\varepsilon}^2}{2\Delta T} = \frac{a_0^2}{2b}.$$

Thus, we demonstrate that in a 2nd order phase transition driven by a primary order parameter, the heat capacity discontinuity can be directly related to thermodynamic quantities derived from the secondary order parameter. This result is generally true in any Landau model with bilinear coupled order parameters but is typically unnecessary to consider in a system in which the primary order parameter is directly accessible, and so we believe this formulation has not been considered previously. In Figure 3.5b we show a very strong agreement between $\frac{\Delta C_V}{T_S}$ and $\frac{C_{66,0}\tilde{\varepsilon}^2}{2\Delta T}$ for the underdoped side of the $Ba(Fe_{1-x}Co_x)_2As_2$ phase diagram, confirming the validity of this result. We explore the implications of this result in section 3.6. We first review a broad set of previously reported data to extract precise values for $\frac{\Delta C_V}{T_S}$, $\tilde{\varepsilon}, \Delta T$ and $C_{66,0}$ across the underdoped side of the Co-doping phase diagram.

3.5 Comparison of experimental data and theoretical prediction

We first discuss evidence of a mean-field orthorhombicity within the nematic phase. Early characterizations of the structural transition using x-ray diffraction found a continuous onset of orthorhombicity at T_S with either a first-order jump in orthorhombicity at T_N for the parent compound and dopings up to ~2.2% Co, or a continuous orthorhombicity with a change in slope at T_N at higher

dopings [45], [63]. Typically, the temperature dependence of the orthorhombicity has been considered over a large temperature range across both the purely nematic phase ($T_N < T < T_S$) and the antiferromagnetic phase ($T < T_N$), with power law fitting used to describe the temperature evolution [63]. However, the formation of static antiferromagnetic order is expected to contribute additional effects to the temperature dependence of orthorhombic order, and within the SDW phase the orthorhombicity should not be interpreted as perfectly linear proportional to the nematicity as it can be within the paramagnetic nematic phase [65]. Therefore, we extract the mean-field magnitude of the orthorhombicity by considering only the orthorhombicity within the nematic phase, in a window of ~4K-10K below the transition.

We reexamine the x-ray diffraction data for Co= 0.018 and 0.047 in reference [45] , supplemented with our own previously unpublished data for Co=0.025 and 0.040 . In Fig.3.2a-b the orthorhombicity within the nematic phase is well fit to $(T_S - T)^{\frac{1}{2}}$ in agreement with the mean-field prediction, despite the discontinuous jump at T_N for the Co=1.8% sample and the decreased slope for the Co=4.7% sample at T_N. To more quantitatively assess the critical exponent of the orthorhombicity within the nematic phase, we plot the data on a log-log scale using the reduced temperature $\left(\frac{T_S - T}{T_S}\right)$ in Fig.3.2c. We find that for the 4 considered dopings, the nematic phase orthorhombicity can indeed be well described with a critical exponent of $\frac{1}{2}$, with $R^2 > 0.99$ for all dopings. This ensures that the orthorhombicity within the nematic phase is well described by a mean field model. We extract the orthorhombicity amplitude from fitting the data to $\varepsilon = \tilde{\varepsilon}\,(T_S - T)^{\frac{1}{2}}$. In Fig.3.5a (red squares) we find that $\tilde{\varepsilon}$ smoothly decreases as the nematic phase is suppressed with doping.

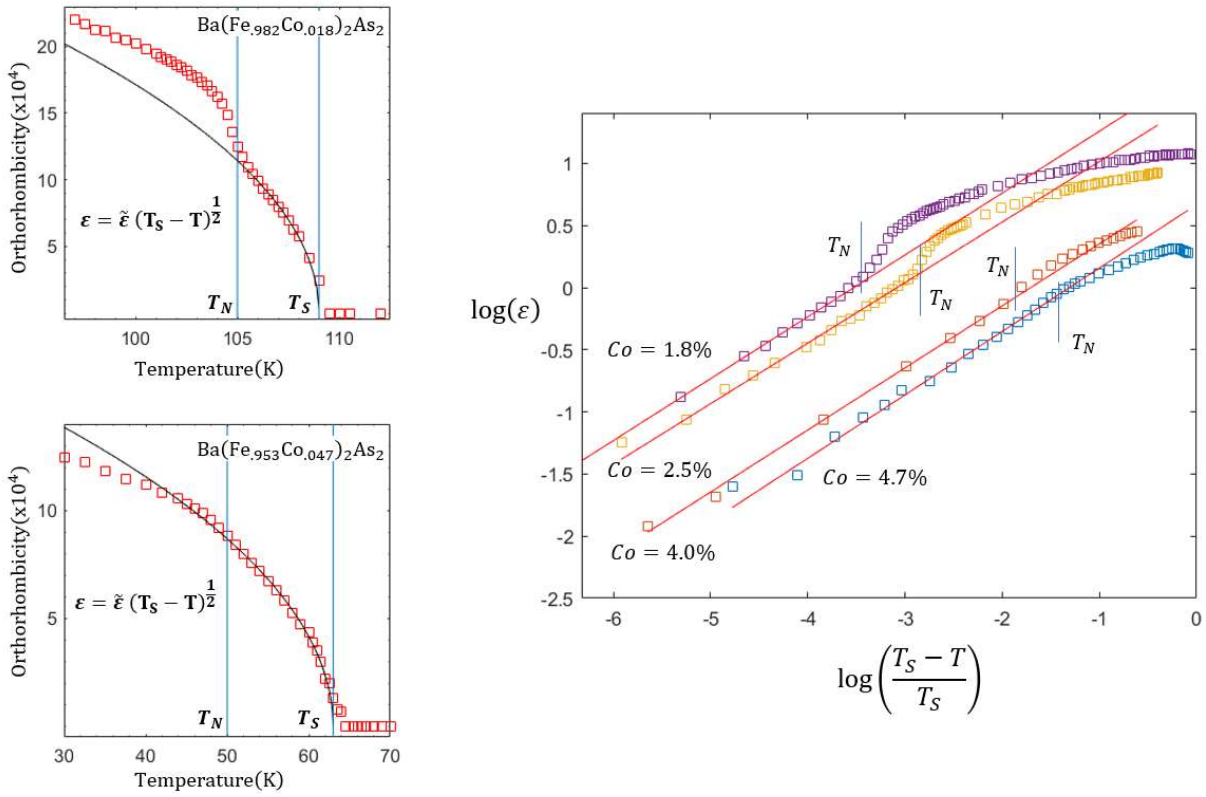

Figure 3.2 The orthorhombicity vs temperature for two Co-doped samples as determined from x-ray diffraction. The orthorhombicity is well fit to $\varepsilon = \tilde{\varepsilon}\,(T_S - T)^{\frac{1}{2}}$ within the purely nematic phase (between the grey bars). Plotting four samples on a log log scale using the reduced temperature shows the orthorhombicity is well fit with a critical exponent of $\frac{1}{2}$ with $R^2 > 0.99$. Values of $\tilde{\varepsilon}$ across the doping phase diagram presented in Fig.3.5a.

Next, we seek to extract the bare nematic transition temperature T^* from measurement of the diverging nematic susceptibility. The Curie-Weiss temperature dependence of the nematic susceptibility and the enhanced transition temperature have been widely observed across a diverse set of measurements, including elastoresistivity [55], [70], electronic Raman scattering[71], [72], and a variety of shear modulus measurement paradigms [43], [46], [53], [54], [73]. We focus here on elastoresistivity measurements which directly probe the conduction electrons at the Fermi surface, i.e. the electrons that form the nematic order. As discussed in Chapter 6, the $2m_{66}$ elastoresistivity constant is directly proportional to the nematic susceptibility as

$$2m_{66} - 2m_{66,0} = k\frac{d\psi}{d\varepsilon} = \left(\frac{k\lambda}{a_0}\right)\frac{1}{(T - T^*)}$$

Where $2m_{66,0}$ is a material dependent background elastoresistivity unrelated to nematicity. In Figure 3.3 we present $2m_{66}$ data for a Co=2.5% sample from ref. [55], which follows a Curie-Weiss fit over a range 100K-200K, with R^2>0.99. From this fit we extract the value of T^*. The structural transition

temperature T_S is defined from the peak in $\frac{d^2\rho}{dT^2}$ which coincides with the formation of the orthorhombic lattice distortion [45], and from these two points we define the temperature enhancement $\Delta T = T_S - T^*$. In Figure 3.5a we show values of ΔT across the underdoped side of the phase diagram, which shows a gradual increase from ~20K at 0% to ~25K by 4.7%. Note that this increase happens along with a ~70% decrease in $\tilde{\varepsilon}$. Meanwhile, the high-temperature limit of the shear modulus, $C_{S,0}$, remains relatively constant across this doping range (data from ref. [68]).

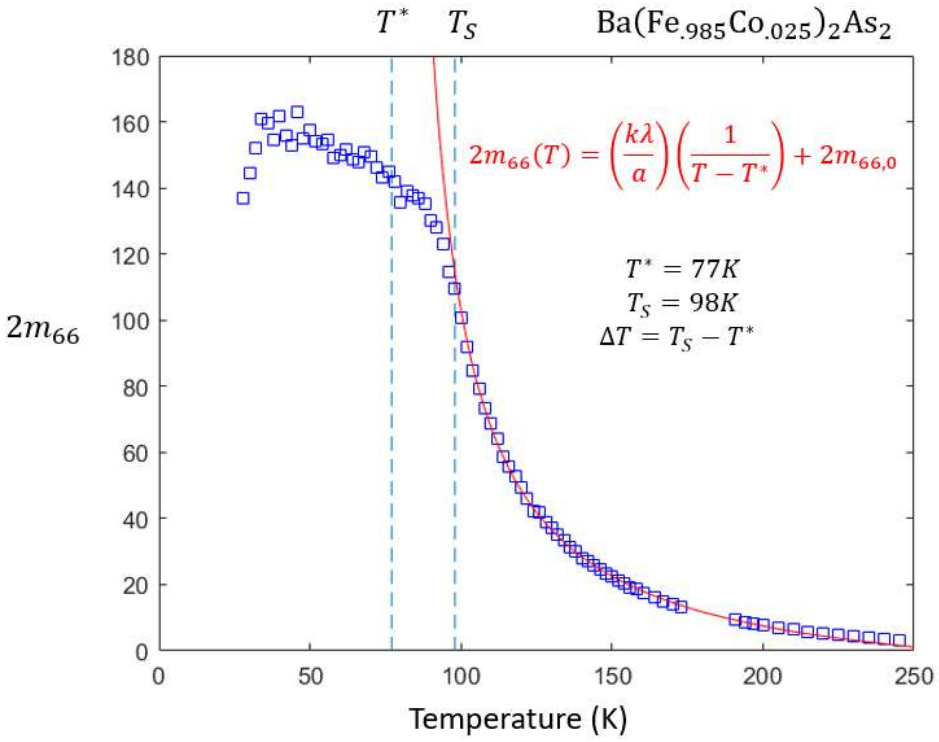

Figure 3.3 The elastoresistivity coefficient $2m_{66}$ vs temperature for a 2.5% Co-doped sample from ref. [55]. For a ~100K temperature range above T_S , we fit the elastoresistivity to a Curie-Weiss dependence as $2m_{66} \propto (T - T^*)^{-1}$ (red line) and extract a value of T^*. From this, we determine the temperature enhancement $\Delta T = T_S - T^*$. Values of ΔT across the doping phase diagram presented in Fig.3.5a.

The heat capacity was measured for 5 samples of $Ba(Fe_{1-x}Co_x)_2As_2$ with dopings x=0, 0.016, 0.025, 0.036, and 0.061 in reference [27] and one sample of x=0.043 in ref. [43]. In the parent compound, any second-order discontinuity in the heat capacity at T_S is washed out by the large first-order latent heat of the antiferromagnetic transition at T_N, which occurs within 1K of T_S (similarly, the continuously-ordering orthorhombicity that forms at T_S is overwhelmed by the discontinuous jump at T_N, preventing a mean-field comparison of heat capacity to orthorhombicity for the parent compound). With Co-doping, the temperature splitting between T_S and T_N increases, allowing the heat capacity features of each transition to be cleanly separated and analyzed. Doping rapidly diminishes the jumps in heat capacity at both transitions, such that by x=0.061 the nematic transition no longer shows a definite

jump. However, this makes the x=0.061 sample useful as a measure of the background phonon contribution. This background is subtracted for x=0.016, 0.025, and 0.036 to reveal the discontinuity in the heat capacity at the transition (Fig.3.4). Due to the doping inhomogeneity of the sample, the discontinuity is spread across a small temperature range. We average data in a ~2K window above and below the transition and take the difference as ΔC_V (Fig.3.4, shaded dots used for the average). The enhanced nematic transition temperature T_S is taken at the middle of the jump. For x=0.043, the discontinuity is very small and ΔC_V is taken as the offset in a linear fit to the heat capacity above and below the transition (see Supplementary Figure A1 in ref. [43]). The quantity $\frac{\Delta C_V}{T_S}$ for each sample is presented in Figure 3.5b (blue dots).

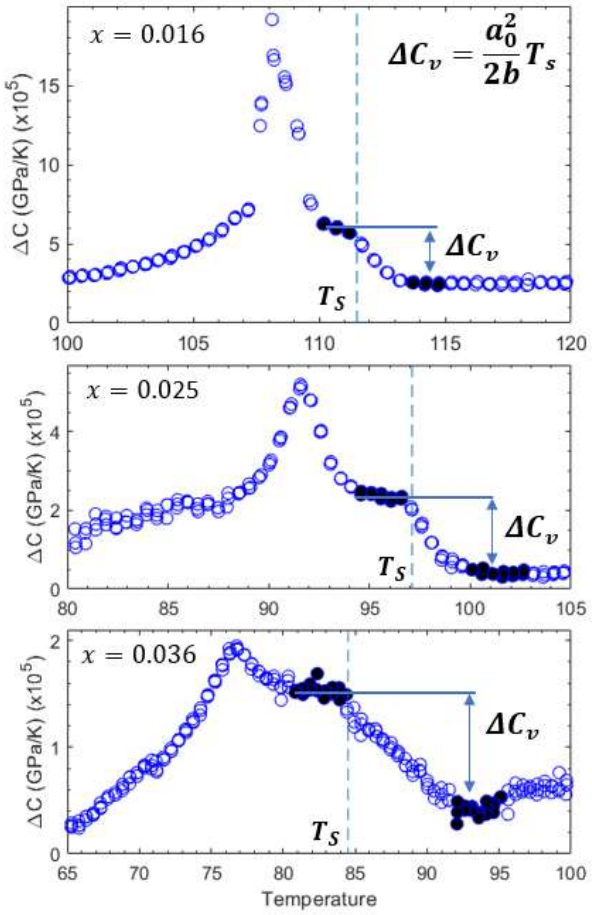

Figure 3.4 Heat capacity with background phonon contribution subtracted for 3 doping values. The step-like increase ΔC_v at T_S is determined by averaging the shaded points above and below the transition and taking the difference. Extracted values of $\frac{\Delta C_V}{T_S}$ across the doping phase diagram presented in Fig.3.5b.

3.6 Conclusions

Figure 3.5b presents the main result. The quantities $\frac{\Delta C}{T_S}$ (blue) and $\frac{C_{S,0}\tilde{\varepsilon}^2}{2\,\Delta T}$ (red) are in excellent agreement with each other. **From this result, we conclude that the purely nematic phase transition in this doping range is very well described by Landau mean-field theory.** While numerous points of evidence have separately suggested a mean-field transition, the presented data are also self-consistent with each other within this framework, strengthening the foundation of this definition of phenomenological mean-field nematicity.

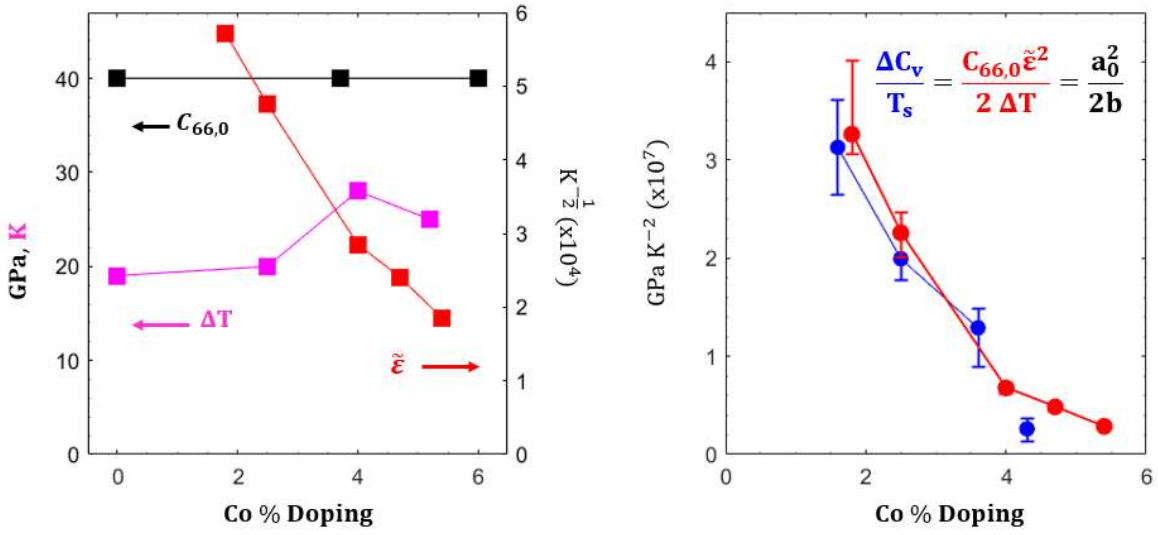

Figure 3.5 (a) The doping dependence of the orthorhombicity magnitude $\tilde{\varepsilon}$, the temperature enhancement ΔT , and the bare shear modulus $C_{66,0}$ (taken as the high temperature limit of the measured shear modulus in ref. [68]). (b) The values of the thermally normalized heat capacity discontinuity $\frac{\Delta C_v}{T_S}$ and the free energy relation of 3 lattice thermodynamic quantities $\frac{C_{66,0}\,\tilde{\varepsilon}^2}{2\,\Delta T}$ are in strong agreement with each other. Here we use the averaged value of $C_{66,0}$ which is essentially constant with doping.

Chapter 4:
X-ray Techniques Review

4.1 Introduction

In 1901 Wilhelm Conrad Röntgen was awarded the first ever Nobel prize in physics for his discovery of x-rays. Since then, there have been at least 10 Nobel prizes in physics and many more in chemistry awarded for either developing our knowledge of x-rays themselves or using them in frontier science for characterizing everything from crystal structures to molecular and biological compounds, including the discovery of the double helix shape of DNA as first measured by Rosalind Franklin. Indeed, x-rays were crucial to proving that regular crystals are formed from a periodic arrangement of atoms, which set the stage for the quantum theory of solid state physics.

An x-ray is a photon with an energy in the approximate range of 100eV to 100 keV. This energy range overlaps with the electron excitation energies for core level transitions in all but the very lightest elements. Therefore, core electron transitions are associated with the absorption and emission of x-rays, which can be used to identify elemental compositions (Section 4.3, EDX) as well as characterize element-specific magnetization (Section 4.4, XMCD). These energies correspond to photon wavelengths in the approximate range 0.1Å to 100Å. As atoms in a crystal are typically a few angstrom apart, x-rays are just the right size to scatter from planes of atoms and constructively interfere, and the wavelike nature of photons gives rise to x-ray diffraction off of static charge order like the crystal structure itself as well as charge density waves (Section 4.5, XRD). When taking into account second-order scattering processes, it is even possible to scatter x-rays from static magnetic order (Section 4.6, XRMS). Finally, photons can also individually scatter to create quasiparticles like phonons and magnons and induce intraorbital transitions, giving rise to inelastic scattering (Section 4.7, RIXS).

In this chapter we will review the theoretical basis for x-ray interaction with electrons and will discuss 5 x-ray techniques I used during my thesis work, including data I collected at beamlines 4-ID-D, 6-ID-B and 27-ID-B at the Advanced Photon Source at Argonne National Laboratory.

4.2 X-ray interaction with electrons.

The original mathematical description of x-ray diffraction involved classical electromagnetic fields interacting with planes of fixed atoms. We briefly recall the results of the Young's double slit experiment from 1801, in which monochromatic light passing through two slits creates a wave interference pattern on the detector, with areas of increased and suppressed light intensity appearing at specific angles from the slits due to the constructive and destructive interference of the light waves generated at each slit. This result led to a general understanding that light was fundamentally a wave phenomenon. Analogously, one way to describe the x-ray diffraction process is to consider x-rays scattering off each diffraction plane of atoms with each plane acting like a slit generating a new source of x-ray waves. The many sources of waves will generally destructively interfere except at the specific

angles given by the Bragg diffraction condition, $2d\ sin(\theta) = n\lambda$, with d being the real-space distance between atom diffraction planes and λ the x-ray wavelength.

In the early days of quantum mechanics, several key developments led to the demonstration of the particle-basis of light. For instance, Einstein's photoelectric effect predicted quantized packets of light with fixed energy (i.e. photons), as did the Bohr model of the atom to explain the fixed energy absorption/emission lines. The most direct evidence came from Compton's x-ray-electron scattering experiments in 1927 which showed that light could inelastically scatter like a single particle. In this same era, it was realized that a single particle of light passing through a double slit apparatus could apparently interfere with itself to yield the same interference pattern generated by a bright light source. These results led to the development of the quantized electromagnetic field theory and single photon interactions with matter, eventually giving rise to quantum electrodynamics. In this framework, a single photon passing through a crystal can be thought to scatter off many planes of atoms and constructively interfere with itself to yield the same Bragg diffraction condition originally developed for a classical electromagnetic field. Further, this theoretical development predicts other types of interactions between photons and matter, such as resonant scattering and inelastic scattering.

Here I will review the basics of an electron's interaction with a beam of incident x-rays by writing out the Hamiltonian of z electrons on one atom in the presence of the quantized electromagnetic radiation field, following refs.[74], [75]:

$$H_e = \sum_{j=1}^{Z} \frac{1}{2m_e}\left[\overrightarrow{p_j} + \frac{e}{c}\vec{A}(\vec{r_j})\right]^2$$

$$= \sum_{j=1}^{Z} \frac{e^2}{2m_e c^2}\vec{A}(\vec{r_j})^2 + \sum_{j=1}^{Z} \frac{e}{2m_e c}\left[\overrightarrow{p_j}\cdot\vec{A}(\vec{r_j}) + \vec{A}(\vec{r_j})\cdot\overrightarrow{p_j}\right] + \dots$$

$$= \Delta\mathrm{H}_1 + \Delta\mathrm{H}_2 + \vartheta(p2)\,.$$

Here, the scattering term given by $\Delta\mathrm{H}_1$ is quadratic in $\vec{A}$ with no dependence on the electron's canonical momentum $\overrightarrow{p}$. The $\Delta\mathrm{H}_2$ term is linear in both $\vec{A}$ and $\overrightarrow{p}$ and will be involved in resonance phenomena. We use this Hamiltonian to connect an initial state $|a, \hbar\omega_k\rangle$ and final state $|b, \hbar\omega_{k'}\rangle$, with electron orbital states a and b and incoming and outgoing photon momenta k and k' respectively. From this we can write out the Fermi golden rule scattering rate:

$$W = \frac{2\pi}{\hbar}\left|\langle b, \hbar\omega_{k'}|\Delta H_1|a, \hbar\omega_k\rangle + \sum_n \frac{\langle b, \hbar\omega_{k'}|\Delta H_2|n\rangle\langle n|\Delta H_2|a, \hbar\omega_k\rangle}{E_a + \hbar\omega_k - E_n}\right|^2 \delta(E_a - E_b + \hbar\omega_k - \hbar\omega_{k'})$$

The first term describes Thomson scattering, an elastic scattering process in which the energy of the photon is unchanged, but its momentum direction can be changed. This term will only be nonzero for $|a\rangle = |b\rangle$, meaning the electron remains in the same orbital state through the scattering process. Further, the photon linear polarization will be unchanged after the scattering. This term is the main contributor to structural x-ray diffraction (XRD).

In the second term, the interaction ΔH_2 can connect two electron states $|a\rangle$ and $|n\rangle$ with energies E_a and E_n and can describe both elastic and inelastic processes. Importantly, the state $|n\rangle$ does not include a photon and so this transitory state represents the absorption of the incident photon. The second term amplitude is smaller by a factor $\frac{\hbar\omega}{mc^2}$ due to the two evaluated matrix elements, and so is generally several orders of magnitude smaller than the first term for arbitrary x-ray energy. However, for a specific photon energy $\hbar\omega_k = E_n - E_a$, the denominator vanishes and this term can become a significant source of x-ray scattering. A photon of this energy causes a transition between two orbital states in the atom, with the transition energy called a **resonance**. This resonance energy is very important for a variety of techniques, including most described here: EDX, XMCD, XRMS and RIXS. The Thomson scattering is always the dominant scattering contributor when present, but for many techniques there are tricks to reduce or eliminate its presence, including by choosing structurally forbidden reflections and by using a polarization dependent analyzer crystal.

4.3 Energy Dispersive X-ray Spectroscopy (EDX) for elemental characterization

Energy dispersive x-ray spectroscopy (known equivalently as EDX or EDS) is a material characterization technique used to find the relative composition of different elements in a sample. It is accessible to UW researchers through the Molecular Analysis Facility on campus and was the first x-ray technique I learned early in my PhD work to characterize samples grown in our lab. In an EDX measurement, the sample is hit with an electron beam which generates electron core transitions and emits x-rays. The energies and relative intensities of these x-rays are characteristic to each element; for instance, in Eu the transition between the 3d and 2p orbitals emits an x-ray of energy 5.85 keV, and so when scanning the electron beam across a crystal sample that contains Eu, an emission peak will occur at this energy. For a sample with multiple elements present, a large number of x-ray emission peaks at different energies will occur. As the emissions for each element are well characterized, the relative intensities of each peak can be used to find the relative proportion of each element in the sample (note that this is a surface dependent technique and so can be very affected by surface oxidation, contaminants, vacancies etc.). Thus, the EDX spectra acts like a “fingerprint” for the composition of a sample. This is very similar in spirit to the use of absorption lines in optical spectroscopy to identify the chemical composition of stars, a technique which was developed by Cecilia Payne at Harvard as the core of her thesis work and which revealed for the first time that the Sun was primarily composed of hydrogen and helium (as she was a woman in the early 1900s, she was denied a PhD from the all-male university, and she instead received the first astronomy PhD from Radcliffe College, the all-women’s college then associated with Harvard [76]).

In Figure 4.1 the EDX spectra is shown for a sample of nominal composition $\mathrm{Fe_3GeTe_2}$ for a single electron beam spot on the crystal surface. The intensity vs emitted x-ray energy shows many peaks corresponding to each element. The relative abundance of each element at this spot is shown in the inset box. The spot size of the electron beam is very small, allowing a characterization of the

chemical composition homogeneity across the whole sample. The table displays the average and standard deviation across 4 total spots on the sample. I took this data to confirm the stoichiometry of samples grown by my labmate Paul Malinowski, and samples from this growth were used in a collaboration with the research group of Prof. Xiaodong Xu and his then-post-doctoral research scientist Zaiyao Fei. This material is among the first discovered exfoliable van der Waals materials that exhibits intrinsic 2D itinerant magnetism, and this work led to the first publication that I was credited on [77].

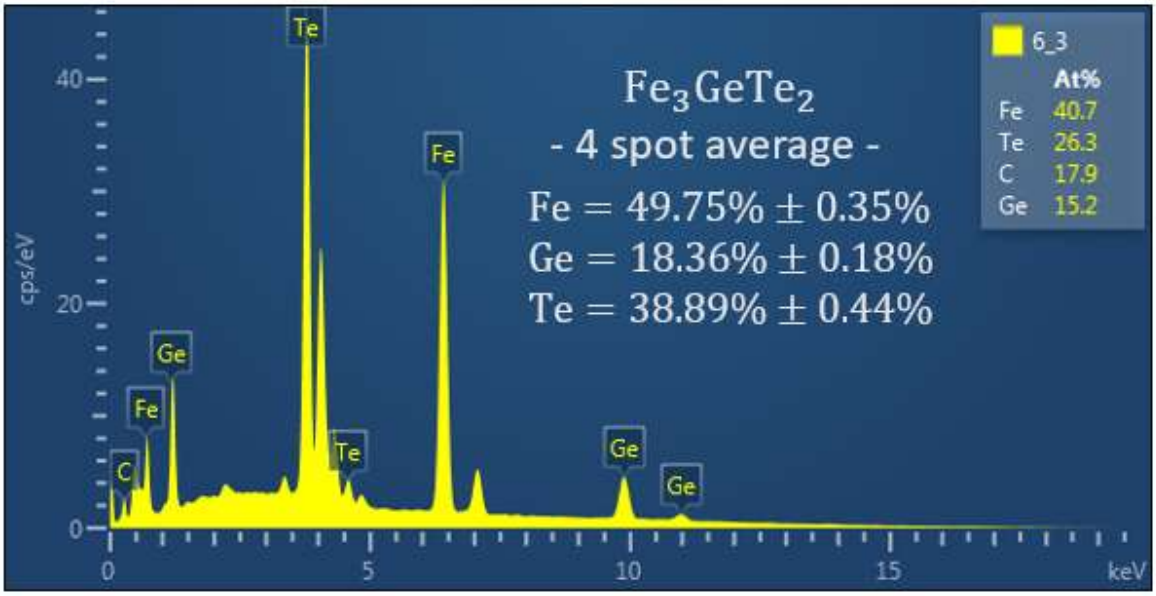

Figure 4.1 EDX spectra of Fe_3GeTe_2. Spectra shown for a single location on crystal surface. Note the presence of carbon (C) due to carbon SEM tape affixing the sample during the measurement. Single location measurement shown in inset box. Four locations were used to yield the averaged values with standard deviation after removing C.

4.4 X-ray Magnetic Circular Dichroism (XMCD) for magnetization characterization

Beyond simply characterizing the elemental composition of a material, there is additional information about the orbital and spin polarization state of atoms that can be gleaned from x-ray absorption and emissions. In this section we discuss x-ray magnetic circular dichroism (XMCD) which as the name implies involves circular polarized x-rays which give information about magnetism. What's more, as this is a resonance technique it has elemental specificity and permits the separation of magnetic contributions from different elemental species in one sample. The XMCD signal is essentially the normalized difference between the x-ray absorption spectra (XAS) of a right and left circularly

polarized x-ray beam and corresponds to the spin polarization of the density of states along the beam direction.

First we discuss the response of a sample containing Eu that has zero spin polarization to a beam of circular polarized x-rays incident along the $+\hat{z}$ direction and tuned to the energy of the Eu L_3 absorption edge (6.97 keV). This energy corresponds to an electronic transition from the totally occupied $2p_{3/2}$ orbital to the 5d orbital. If the beam is left circular polarized, it will cause excitations of both spin up and spin down electrons, but due to the photon angular momentum it will preferentially couple to the spin up electrons such that roughly 63% of the excited electrons are spin up and 37% are spin down. Conversely, a beam of right circular polarized photons excite transitions with the opposite spin probabilities. Importantly, these transitions preserve the spin orientation. As the receiving 5d orbital is not spin polarized, it has an equal number of available spin up and spin down states, and either spin orientation of the 2p excited electron will be equally likely to make the transition. Therefore, the absorption intensities μ_L^{abs} and μ_R^{abs} of the left and right circularly polarized beams will have the same value in the sample. We can define the XMCD as the difference in these intensities $\mu_L^{abs} - \mu_R^{abs}$, which here is just zero.

Next we consider every Eu atom in the sample being weakly magnetized along the $+\hat{z}$ direction. This could be due to an applied magnetic field along $+\hat{z}$, an internal Eu ferromagnetic order aligned along $+\hat{z}$, or as a result of a different element in the crystal having a net magnetization (or all of these at the same time). Now, spin up states in the Eu 5d orbital will be slightly more occupied and spin down states will be slightly more available. From Fermi's golden rule, the spin down electrons will be slightly more favored to make the transition than the spin up electrons. Therefore, we would expect that the absorption of right circular polarized beam to increase and the left circular polarized beam to decrease. Now the XMCD signal $\mu_L^{abs} - \mu_R^{abs}$ becomes nonzero, indicating a net magnetization over all Eu atoms in the sample (really, within the spot size of the beam and within a characteristic x-ray penetration depth, which for this energy is about 5 μm).

Finally, we consider the XMCD signal from an antiferromagnet, in which half of the local Eu moments are aligned along $+\hat{z}$ (with $\vec{m} = +m\hat{z}$) and half along $-\hat{z}$ (with $\vec{m} = -m\hat{z}$). Now, the XMCD signal is positive for the $+m\hat{z}$ aligned atoms and negative for the $-m\hat{z}$ atoms, such that over the sampled volume the average XMCD signal is zero, i.e. $\langle \vec{m} \cdot \hat{z} \rangle = 0$. If the beam had instead been incident along the $\hat{x}$ direction, on each atom there would be no preference between $+\hat{x}$ and $-\hat{x}$ spin polarization and each individual atom would contribute a null XMCD signal, resulting in $\vec{m} \cdot \hat{x} = 0$ for each individual atom and $\langle \vec{m} \cdot \hat{x} \rangle = 0$ across the whole sample.

From this discussion it is clear that the total XMCD signal is only sensitive to the net magnetization of a sample (really, the net spin polarization of the density of states) and not to the local moment size. This stands in contrast to the magnetic scattering technique (XRMS) discussed in the next section, in which the periodicity of long range magnetic order allows for q-dependent diffraction from the magnetic lattice and so can be used to characterize diverse antiferromagnetic orders. Nonetheless, by applying a magnetic field along different crystal axes, the field dependence of the XMCD signal can be used to work out details of the magnetic structure of the sample. Further, as the value of the XMCD

corresponds to the net magnetization of the sample, the slope of the XMCD to applied magnetic field corresponds to the magnetic susceptibility of the sample, which is less directly measurable by XRMS. Finally, XRMS is generally much more difficult to use for characterizing ferromagnetic order than XMCD due to the dominant charge diffraction from the crystal lattice itself.

In a transmission mode XMCD measurement the absorption of each circular polarized beam is determined directly by measuring the transmitted beam intensity. However, this only works well for very thin samples (roughly 10 μm or less). For thicker samples and samples mounted on a stress device, it is necessary to instead measure the intensity of photons that are reemitted after absorption; this is fluorescence mode XMCD. After an electron is excited to the 5d orbital, a hole is left behind in the 2p orbital which is rapidly filled in by other electrons in the atom. For each orbital state with an allowed transition to this 2p hole, there is some probability of the transition occurring and a photon of the corresponding energy difference is emitted in the process (note that the presence of the "positively charged" hole shifts the transition energies between orbitals). In this example, the 3d electrons have the most spatial overlap with the 2p state and so has the highest transition probability, with a photon of energy 5.85 keV being emitted (called the L_α emission line). Thus, the largest fluorescence mode XMCD signal in this case is found by measuring the intensities of the L_α emission line for the two circularly polarized incident beams. After self-absorption correction and a normalization procedure, we define the emission intensities as μ_L and μ_R, with the XMCD defined as $\mu_L - \mu_R$ and the x-ray near-edge absorption spectra (XANES) as $\mu_L + \mu_R$ (the term XANES is used for incident beam energies close to the absorption edge).

Figure 4.2 shows a typical set of fluorescence mode XANES and XMCD data for $\mathrm{EuFe_2As_2}$, with a 1T magnetic field applied in-plane along the beam direction. In a real measurement, the energy of the incident beam is scanned from below to above the absorption edge to map out the full energy dependence of the XANES and the XMCD. The large nonzero value of the XMCD at the absorption edge energy indicates a net magnetization of the sample. Incident x-rays with less energy than the L_3 edge do not cause the 2p-5d transition and so the XANES signal is zero in this range (aside from background sources). Incident x-rays tuned to energies beyond the edge kick core electrons out of their atoms, and so past the absorption edge the XAS is nearly constant up to the next absorption edge (small oscillations in the XAS over this range can give information about ejected electron backscattering using a technique called EXAFS). Different shapes of the XANES give information about the oxidation state of the probed element and for instance has been used to observe element-specific oxidation changes under physical or chemical pressure [78].

As stated above, the field dependence of XMCD with applied magnetic field can be used to work out details of the magnetic order and its response to field. For instance, in Figure 4.3 the same sample of $\mathrm{EuFe_2As_2}$ is strain-detwinned and aligned with the applied field such that the incident beam (and thus the probed magnetic polarization direction) is along the Eu AFM easy axis. For zero applied field, the signal is approximately zero, indicating no net magnetic polarization in this direction. For increasing field the signal is still very small as the moments are unable to cant towards the field direction. At B=0.48T, the XMCD signal suddenly jumps to a nearly full saturation, indicating a metamagnetic spin flip

transition. This is a key result to my paper “Strongly anisotropic antiferromagnetic coupling in $EuFe_2As_2$ revealed by stress detwinning” , ref.[9] , discussed in detail in Chapter 7.

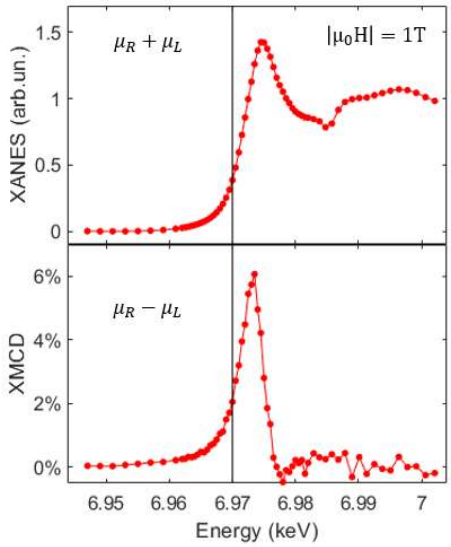

Figure 4.2 XANES and XMCD spectra of $EuFe_2As_2$. μ_R and μ_L correspond to the normalized emitted intensity for right and left circular polarized incident x-rays. Data taken at T=7K and 1T of in-plane applied magnetic field. Note that as a shorthand, the peak value of the XMCD is often also just referred to as the XMCD.

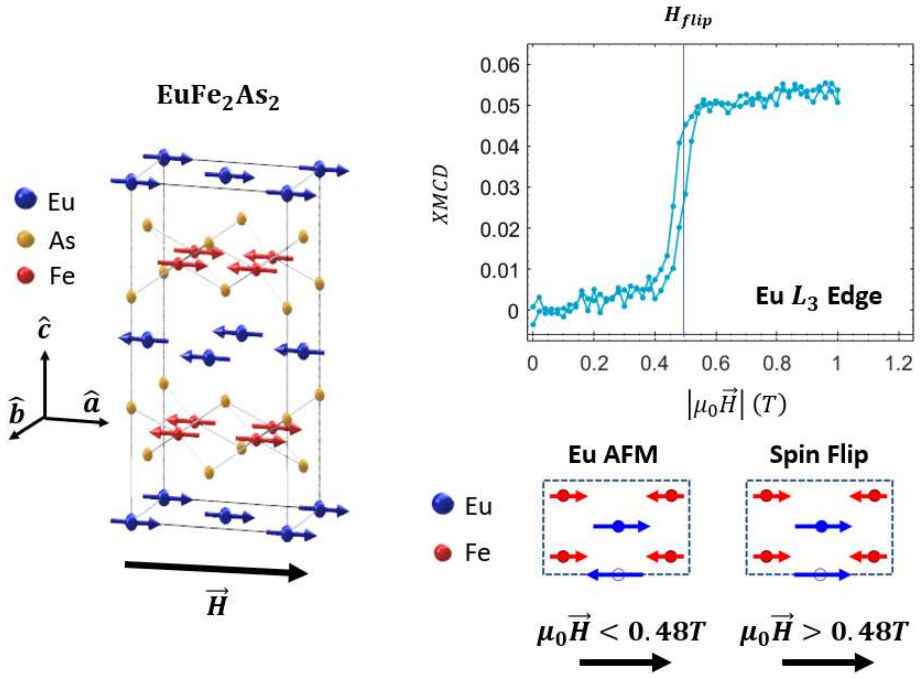

Figure 4.3 The crystal and magnetic structure of fully ordered $EuFe_2As_2$. A field is applied along the Eu AFM easy axis. The XMCD value versus applied field indicates a metamagnetic spin flip transition at 0.48T.

4.5 X-ray Diffraction (XRD) for charge distribution and structural characterization

X-ray diffraction is a powerful technique for determining the crystal structure of a material. A temperature dependence of the crystal lattice constants is often an early measurement done in the characterization of a new material, as it shows how the structural symmetry changes at each phase transition, yielding insight to the symmetry of the electronic, magnetic or structural driver of the transition. In Figure 4.4a, the temperature dependence of the tetragonal $(2\ 2\ 12)_T$ reflection XRD is shown for a sample of $Ba(Fe_{.96}Co_{.04})_2As_2$. The splitting of the structural peak indicates a tetragonal to orthorhombic structural phase transition and the formation of orthorhombic twin domains. A major focus of my thesis work is using XRD combined with uniaxial stress to precisely detwin a material with twin domains. This will be discussed in detail in Chapter 6. As a preview, Figure 4.4b shows the detwinning results for the same sample at T=66K, which shows the relative intensities and positions of the two peaks changing with tension and compression. The lower panel shows the relative intensity corresponding to the A domain, which indicates a smooth strain detwinning between the B and A monodomains, discussed in the figure caption.

Besides the lattice constants of the ideal unit cell of a material, XRD can also be used to find other periodic modulations of charge such as in charge density waves. This section will focus on XRD at

arbitrary energy and not at a resonance energy (resonant x-ray diffraction can be used to measure the spacing of specific atoms within a unit cell, for instance to measure the As height above the Fe plane in $\mathrm{BaFe_2As_2}$ [79]). One type of x-ray diffraction measurement is a simple rotation of the sample (by θ) simultaneous with a rotation of the detector (by 2θ), called a "theta 2 theta" scan. For a given structure (e.g. cubic, orthorhombic etc.) there will only be diffraction peaks at specific angles corresponding to satisfying the Bragg condition. This can be used to determine the structure of a new material. It is also used as a first characterization of a sample to see the sharpness of the peaks (the "mosaicity" or how perfect the crystallinity of the sample is) and as part of an initial calibration lineup of the sample. In Figure 4.5, I show room temperature XRD data for a single crystal sample of $\mathrm{ErTe_3}$, which I scanned over a θ range of 45 degrees as part of an initial lineup of the sample to calibrate the alignment of the sample relative to the beam. The multiple structural peaks were at the expected angles, indicating the structure and lattice constants of the sample matched literature values. The real goal of the $\mathrm{ErTe_3}$ measurement was to observe the charge density wave that forms below $T_{CDW} = 265K$ and attempt to change its intensity by applying strain. In Figure 4.6, I show the XRD data at the (1 15 0.73) reflection where a CDW peak forms. Here, we applied voltage to a strain device and were able to decrease the amplitude by about 30%. This was a proof-of-principle measurement done in collaboration with Prof. Ian Fisher's group at Stanford. For more information on strain tuning charge density waves in this system see ref.[80].

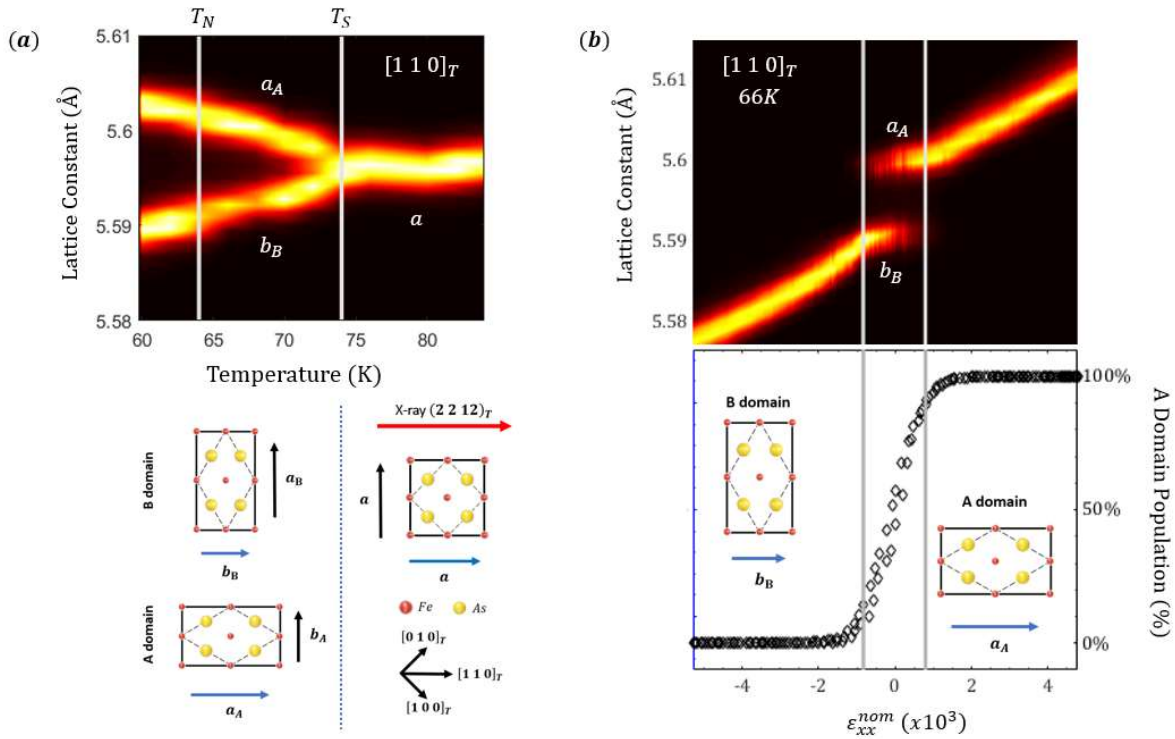

Figure 4.4 (a) XRD vs temperature of a sample of $Ba(Fe_{.96}Co_{.04})_2As_2$ held in a zero nominal strain state. The measurement is at the tetragonal $(2\ 2\ 12)_T$ reflection (direction indicated by red arrow), and the raw XRD data has been converted to the $[1\ 1\ 0]_T$ lattice constant by subtracting the c-axis component from a separate measurement of the temperature-dependent (0 0 14) reflection. Above $T = 74K$, the $(2\ 2\ 12)_T$ reflection shows a single peak indicating only one value of the lattice constant in this direction. Below $T_S = 73.8K$ the single peak splits into two, indicating a tetragonal to orthorhombic structural phase transition and the formation of orthorhombic domains (A and B). In this nomenclature this reflection is sensitive to the longer a lattice constant of the A domain and shorter b lattice constant of the B domain. Conversely, a measurement along the $[1\ 0\ 0]_T$ direction would *not* see a peak splitting, as $\sqrt{a_A^2 + b_A^2} = \sqrt{a_B^2 + b_B^2}$. At $T_N = 64K$ a spin-density wave transition occurs; as this transition does not induce a change in structural symmetry, but instead breaks spin rotation symmetry, it does not make an obvious appearance in the XRD measurement (it can, for instance, manifest as a change in the temperature dependence of a lattice constant, but the spin order does not impact the XRD measurement itself). (b) For the same sample and reflection at 66K, the relative intensities of the a_A and b_B peaks can be strongly tuned by applied tension or compression ($\varepsilon_{xx}^{nom} > 0$ or $\varepsilon_{xx}^{nom} < 0$ respectively). The A domain population is here defined from the intensities of the peaks (I_A and I_B) as $\frac{I_A}{I_A + I_B}$, which varies smoothly from 0% to 100%, i.e. from the B to A monodomain.

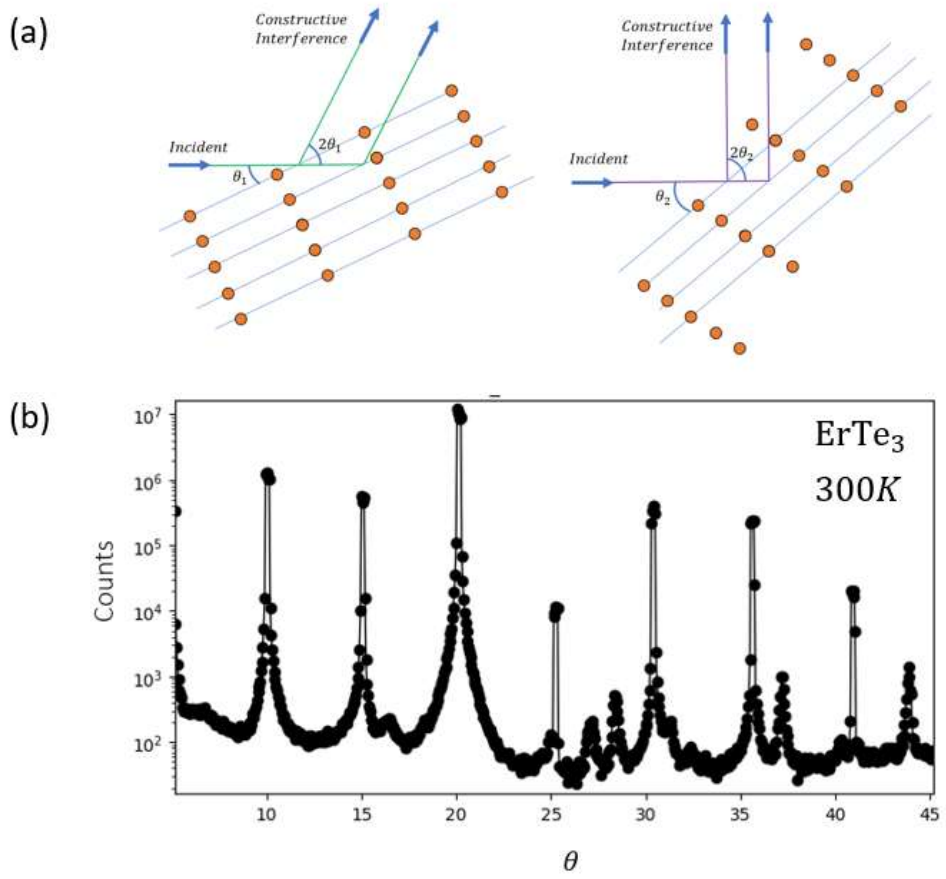

Figure 4.5 (a) schematic of a structural characterization measurement. In a real measurement the incident x-ray beam is held fixed while the sample is rotated, and at specific angles θ_n the Bragg condition is satisfied, allowing constructive interference. (b) A θ rotation scan in $ErTe_3$ at room temperature was performed to characterize the sample. Each intensity peak corresponds to an $(h\ k\ l)$ diffraction peak, specifically a $(0\ k\ l)$ peak (i.e. h is fixed at 0 while k and l change with θ).

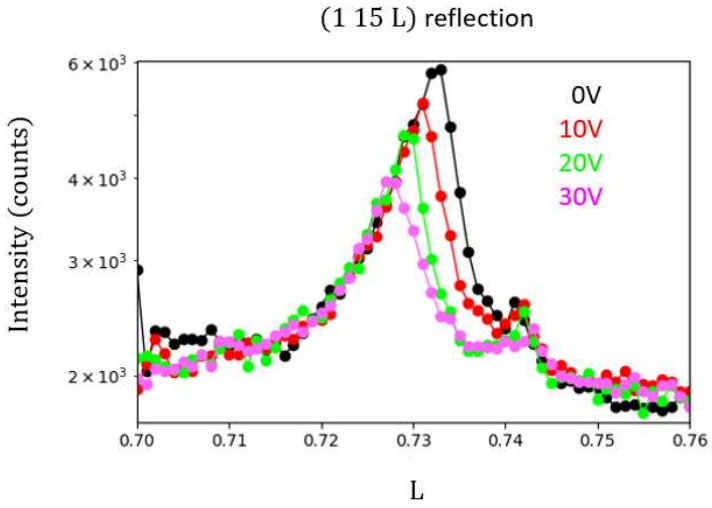

Figure 4.6 (a) $ErTe_3$ sample XRD of the $(1\ 15\ L)$ reflection at 180K. At L=1 a large structural Bragg peak is present. Below the CDW transition at 265K, a small charge density wave peak appears near L=0.73. The amplitude of this peak is found to decrease by ~30% with the application of 30V to the strain device.

4.6 X-ray Resonant Magnetic Scattering (XRMS) for static magnetic order characterization

With the development of very bright highly monochromated x-ray beams from synchrotron sources such as the Advanced Photon Source, it has become possible in the last 30 years to observe the elastic scattering of x-rays off static long-range magnetic order. This is commonly called X-ray Resonant Magnetic Scattering (XRMS) (confusingly, at least two other acronyms for the same technique are in use in the literature, RMXS and MRXS, which are simple commutations of the same terms). This technique offers several advantages over magnetic neutron diffraction, such as being sensitive to the magnetic order of a specific element (via choosing the resonance energy), it can be drastically faster to collect data, and it is usable in much smaller sample sizes. Further, while neutrons are sensitive to the square of the magnetization ($|\vec{m}|^2$), XRMS is sensitive to $\vec{m} \cdot \vec{k}'$, where $\vec{k}'$ is the momentum of the outgoing photon, and so it becomes possible to measure the phase of an antiferromagnetic structure and identify antiphase domains[51]. Conversely, the energy specificity means that soft x-ray sources are needed for lower energy resonances like the L edge of Fe, while hard x-rays are used for the bigger energy k edge of Fe and for heavier elements like Eu and Ir. XRMS was used in ref.[81] to determine the A-type antiferromagnetic structure of Eu moments in $EuFe_2As_2$, one of the two materials I have focused on in my thesis work.

When I first learned of XRMS, I assumed it involved the magnetic field component of a photon interacting with the magnetic moment of electrons. In actuality, it is still the electric field component interacting with the charge of electrons, but the presence of a periodic electron magnetic order causes additional sets of initial and final scattering states to be connected through the quantized photon field

Hamiltonian described above, such that the effective scattering can be described as a scattering from the magnetic lattice[75]. For an arbitrary x-ray energy this magnetic scattering process has a very small scattering cross section; however, the second-quantization formulation of photon-electron interaction shows that at an elemental resonance energy, the scattering intensity can be raised by several orders of magnitude, enabling measurement of magnetic scattering. Whereas charge structure scattering does not induce a phase change in the scattered x-rays, magnetically scattered photons have a 90 degree rotation in their linear polarization. This allows a polarization-sensitive "analyzer crystal" to separate out photons originating from structural vs magnetic scattering such that a detector becomes sensitive to only one source. To further confirm the magnetic origin of the scattered photons, one often picks a specific incident beam polarization and/or a structurally-forbidden reflection in which a magnetic peak is nonetheless allowed to scatter. A key detail in this measurement paradigm is that XRMS does not measure the magnetic moment at a single site but does measure the magnetic lattice formed by the moments. A decrease in XRMS intensity could then result from a decrease in the moment size itself, such as from increasing thermal fluctuations when warming the sample towards the magnetic transition temperature, or as an applied field reorients moments away from the original magnetic structure but doesn't change the moment size. For more information on magnetic scattering see refs.[74], [75].

In Figure 4.7 I present XRMS data from a sample of Sr_2IrO_4. This work was done in collaboration with Professor Jian Liu at the University of Tennessee – Knoxville, and is a continuation of XRMS work in the same material discussed in ref.[82]. This material is a perovskite with an Ir-driven antiferromagnetic order which forms two structural-AFM domains, AFa and AFb, with easy axes along [1 0 0] and [0 1 0], respectively. These structural-AFM domains are similar to those the iron-pnictide materials but with a more complicated arrangement of Ir magnetic moments. At zero magnetic field, the XRMS intensities are similar for the AFa (red) and AFb (blue) domains, implying that each has a similar total volume of the sample. A magnetic field is applied along the [1 1 0] direction which couples to the spins and redirects them towards a ferromagnetic (FM) alignment with the field, suppressing the antiferromagnetic order. This results in both the AFa and AFb intensities approaching zero beyond 1000 Oe while an emergent FM intensity (black) reaches near saturation beyond 1000 Oe. However, the applied field was slightly misaligned such that the AFb moments were able to cant towards the field more effectively and thus reduce their energy compared to AFa moments. This resulted in a modest magnetic field detwinning of the AFa domain towards the AFb domain as seen from the increase in AFb intensity for small applied field. This data demonstrates the power of XRMS to precisely characterize changes in magnetic orders in a complex system.

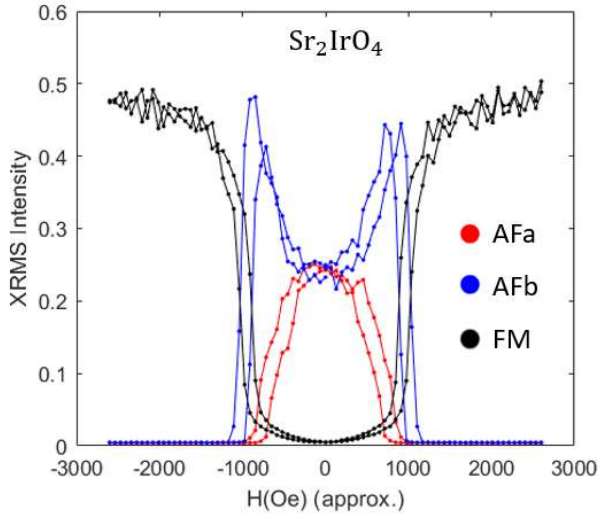

Figure 4.7 XRMS intensity at 210K of the (1 0 22), (1 0 20) and (1 0 21) reflections corresponding to the antiferromagnetic AFa (red) and AFb (blue) domains and the ferromagnetic order (FM, black), respectively. Magnetic field is applied along the nominal [1 1 0] direction.

4.7 Resonant Inelastic X-ray Scattering (RIXS) for quasiparticle and intraorbital transition characterization

Finally, we discuss inelastic x-ray scattering, which simply means the x-ray changes its energy slightly after interacting with the sample. This can happen from a photon losing energy to create a quasiparticle (such as a phonon or a magnon) or by generating an intraorbital transitions such as between two different d orbitals (called d-d excitations) which are not allowed in elastic scattering. When the incident photon is near a resonance energy, its scattering cross section increases dramatically, opening the door to studying element-specific magnetic fluctuations and d-d excitations. Of note, as this is a photon-in photon-out measurement, it can be used to measure magnetic field induced changes to the band structure unlike in ARPES measurements (where the outgoing charged electron is affected by an applied field). Further, this allows for measuring changes in, for instance, the spin fluctuation spectra as the magnetism in a sample is tuned with temperature, applied field, or strain. Finally, an advantage of RIXS over inelastic neutron scattering is that very small samples can be measured.

One common methodology of the RIXS measurement is to use incident photons at one fixed energy and scan the angle of an x-ray analyzer and x-ray detector to measure how many photons are scattered at a particular energy and momentum change. This is then repeated over a range of incident energies to construct an energy transfer plot. Again, this scattering is not from diffraction off a long range charge or magnetic lattice like in XRD or XRMS, nor from an interorbital transition like in EDX and XMCD, but instead is scattering off a single (or sometimes multiple!) quasiparticle (similar to Compton scattering of a photon off a freespace electron) or from a charge transfer between two states within a

single orbital. In the previous discussed scattering techniques, when the sample is aligned to an allowed diffraction reflection there is always some inelastic scattering but it is dwarfed by the much larger elastic scattering intensity. By aligning the sample off a diffraction peak, the elastic scattering intensity decreases enough to observe the inelastic scattering. Among several difficulties with the technique is that there are many potential sources of inelastic scattering for one photon, and so every measurement requires a good theoretical analysis to determine which sources may have contributed to a measured inelastic scattering peak.

As an example of RIXS data, in Figure 4.8 I show data from a sample of $\mathrm{EuFe_2As_2}$ with incident beam energies near the Eu L_3 edge. The sample is oriented at an arbitrary angle where no Bragg diffraction occurs. A large peak is seen near 0 eV loss, which corresponds to elastic scattering events. A second scattering peak is present near 4 eV energy loss, which indicates an inelastic scattering event. This peak is present for 6.973 keV incident photons and gradually shifts into a broad shoulder with increasing incident energy. This is a first RIXS measurement at this energy in this system, and it is assumed that this peak corresponds to an intraorbital charge transfer scattering event as observed in EuB_6 [83]. A future goal for this project is to see how the charge transfer evolves with field and strain tuning of the system.

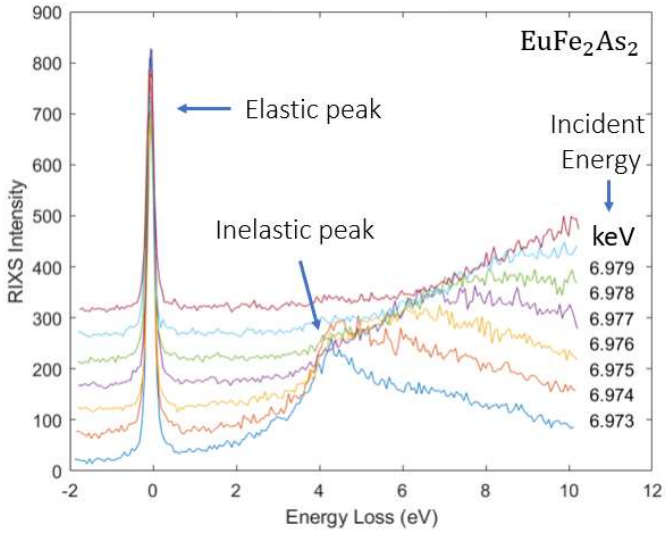

Figure 4.8 RIXS data of $\mathrm{EuFe_2As_2}$. Each line corresponds to a different energy loss scan at fixed incident energy from 6.973 keV to 6.979 keV. The data is characterized by a large zero-energy loss elastic peak and a smaller inelastic peak. The inelastic peak likely corresponds to an intraorbital excitation.

Chapter 5:
Strain and Magnetic Field Coupling to Nematicity and Magnetic Order

Quantum phases are eminently tunable through the coupling of their order parameters to an applied field. The symmetry of the order parameter and field sharply define the way that these two quantities interact. Here I outline 2 sets of combined strain and XRD measurements and one combined strain, magnetic field, and XMCD measurement, which provide useful examples of symmetry breaking field interactions with quantum phases.

5.1 Structural symmetry channels

In this section I will define three strain terms from different symmetry channels that correspond to three irreducible representations ("irreps") of the D_{4h} point group, which are relevant for the tetragonal phase of $BaFe_2As_2$ and $EuFe_2As_2$. These strain terms essentially describe three different ways the lattice can be distorted in-plane and they determine the symmetry change (or lack of change) of each kind of distortion (Fig. 5.1). These distortions can occur spontaneously, for instance by an intrinsic nematic order, and can also be induced by applied hydrostatic pressure or in-plane uniaxial or biaxial stress.

We can determine the $\varepsilon_{A_{1g,1}}$, $\varepsilon_{B_{1g}}$ and $\varepsilon_{B_{2g}}$ strain terms corresponding to the $A_{1g,1}$, B_{1g} and B_{2g} irreps of the D_{4h} point group by using the xyz coordinate system aligned with the 2-Fe unit cell as a basis (note that in Chapter 6 the x-y coordinate plane will be rotated 45 degrees from this definition when using the 4-Fe unit cell). We can define four in-plane lattice constants: a_T and b_T correspond to the unit cell length along the $[1\ 0\ 0]_T$ and $[0\ 1\ 0]_T$ directions (the Fe-As bonding directions), while a_{Or} and b_{Or} correspond to the unit cell length along the $[1\ 1\ 0]_T$ and $[-1\ 1\ 0]_T$ directions (the Fe-Fe bonding directions), respectively. In the undistorted state, $a_{Or} = b_{Or} = \sqrt{2}a_T = \sqrt{2}b_T$ (the undistorted values will hereafter have a 0 subscript). Next we define the unidirectional strains: $\varepsilon_{xx} = \frac{\Delta a_T}{a_{T,0}}$, $\varepsilon_{yy} = \frac{\Delta b_T}{b_{T,0}}$, and $\varepsilon_{xy} = \frac{1}{2}\left(\frac{\Delta a_{Or}}{a_{Or,0}} - \frac{\Delta b_{Or}}{b_{Or,0}}\right) = \frac{1}{2}\left(\frac{a_{Or} - b_{Or}}{a_{Or,0}}\right)$. Finally, we can choose combinations of these unidirectional strains that have the correct symmetry properties as the corresponding irrep name: $\varepsilon_{A_{1g,1}} = \frac{1}{2}(\varepsilon_{xx} + \varepsilon_{yy})$, $\varepsilon_{B_{1g}} = \frac{1}{2}(\varepsilon_{xx} - \varepsilon_{yy})$ and $\varepsilon_{B_{2g}} = \varepsilon_{xy}$. In the tetragonal zero-stress state, all three strain terms are zero. Any arbitrary in-plane distortion $\varepsilon_{inplane}$ from any internal or external source can be decomposed to $\varepsilon_{inplane} = \alpha_1\varepsilon_{A_{1g,1}} + \alpha_2\varepsilon_{B_{1g}} + \alpha_3\varepsilon_{B_{2g}}$ (hence why these terms are called "irreducible"). When an in-plane stress is applied to the sample, the induced lattice distortion will usually be a mix of these different strain terms, as well as an out of plane A_{1g} strain, $\varepsilon_{A_{1g,2}} = \varepsilon_{zz} = \frac{\Delta c}{c_0}$.

Now we discuss the symmetries of the three irreps expressed through the strain terms. To review, the D_{4h} point group has the following symmetries: a 4-fold rotational symmetry about the z axis, four vertical mirror plane reflection symmetries, horizontal mirror plane reflection symmetries, and inversion symmetry (see Chapter 2.2). An $A_{1g,1}$ distortion is an absolute change in the in-plane lattice constants with no relative change between them, and this distortion breaks no symmetries (likewise,

the $A_{1g,2}$ distortion breaks no symmetries). The B_{1g} and B_{2g} distortions involve relative changes of in-plane lattice constants and so both lower the C_4 in-plane rotation symmetry to C_2. A B_{1g} distortion breaks the Fe-Fe mirror plane symmetries while preserving the Fe-As mirror plane symmetries, and vice versa for the B_{2g} distortion. The g subscript of all three irreps indicates that these distortions preserve the inversion symmetry.

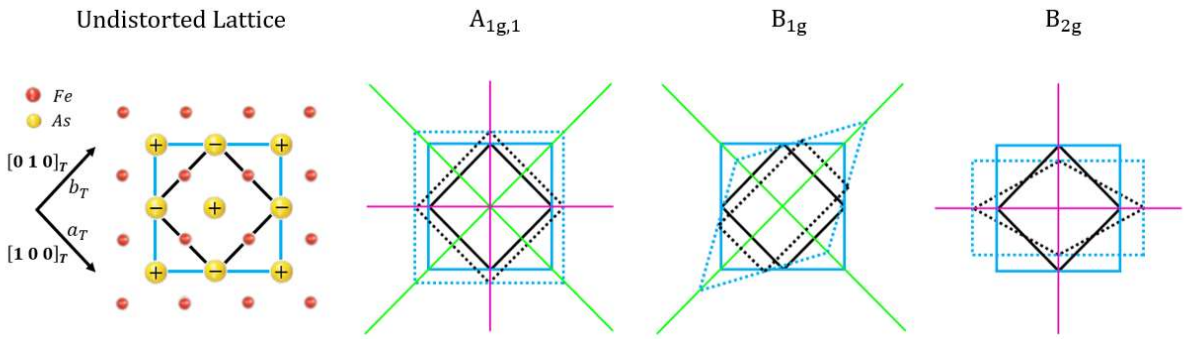

Figure 5.1 The undistorted FeAs plane outlined by the 2-Fe unit cell (black) and the 4-Fe unit cell (blue). The distortions of both unit cells due to the $\mathrm{A_{1g,1}}$, $\mathrm{B_{1g}}$ and $\mathrm{B_{2g}}$ strains are demonstrated as dotted lines, with Fe-As mirror plane (green) and Fe-Fe mirror plane (magenta) preserved symmetries marked as solid lines.

At the nematic transition temperature, a B_{2g} orthorhombicity $\varepsilon_{B_{2g}}$ is spontaneously created, which was an early indicator that the nematicity itself has B_{2g} symmetry (this was later demonstrated further in a variety of elastoresistivity and Raman [71] measurements). As stated above, externally applied stress can generate strain in all three symmetry channels. Now we define how these three strains couple to the nematic order parameter ψ, using a phenomenological description which is very useful for understanding how different strains can tune nematicity and the accompanying resistivity anisotropy. To do so we write out the strain-dependent change ΔF of the Landau free energy (see Chapter 3) that explicitly includes the lowest-order symmetry-allowed coupling to the three different strains,

$$\Delta F \propto -\lambda_{A_{1g,1}}\varepsilon_{A_{1g,1}}\psi^2 + \lambda_{B_{1g}}\varepsilon_{B_{1g}}^2\psi^2 - \lambda_{B_{2g}}\varepsilon_{B_{2g}}\psi\,.$$

Here, the λ terms are phenomenological energy densities for each coupling and are defined as positive constants with the sign given explicitly for the coupling in $\mathrm{Ba(Fe_{1-x}Co_x)_2As_2}$ based on measurements from ref. [84]. As ψ and $\varepsilon_{B_{2g}}$ are in the same symmetry channel they can be linearly coupled at lowest order. The energy of the system is reduced when ψ and $\varepsilon_{B_{2g}}$ have the same sign, and so an applied stress that induces a positive (negative) value of $\varepsilon_{B_{2g}}$ will also induce a positive (negative) value of ψ. Another way to say this is that a particular sign of $\varepsilon_{B_{2g}}$ gives the system a preference in which sign of ψ

to induce. Conversely, a B_{1g} orthorhombicity is in an orthogonal symmetry channel to the B_{2g} nematicity, and so a particular sign of $\varepsilon_{B_{1g}}$ cannot give a preference to a particular sign of ψ. Therefore, their lowest order coupling is quadratic in both $\varepsilon_{B_{1g}}$ and ψ. As an A_{1g} distortion does not break any symmetries, a particular sign of $\varepsilon_{A_{1g,1}}$ likewise cannot give a preference between the two signs of ψ on symmetry grounds, and so the lowest order A_{1g} coupling term must be quadratic in ψ. However, a change in the relative size of the in-plane square lattice can change the relative energy cost of nematic ordering, and so the A_{1g} coupling at lowest order can be linear in $\varepsilon_{A_{1g,1}}$ with either sign of coupling. A biquadratic A_{1g} term of the form $\lambda_{A_{1g,1},A_{1g,1}}\varepsilon^2{}_{A_{1g,1}}\psi^2$ is allowed by symmetry, but this term likely does not need to be considered explicitly as it was shown in ref. [84] that the $\lambda_{B_{1g}}$ coefficient is at least 100 times larger than the $\lambda_{A_{1g,1},A_{1g,1}}$ coefficient for a sample of 2.5% Co-doping.

As a final note, the zero-stress nematic transition is sharply defined at a specific temperature T_S where the C_4 rotational symmetry and the Fe-As mirror plane symmetries are spontaneously broken. A stress applied along $\hat{x}$ will induced strains in the B_{1g} and A_{1g} channels. While this lowers the rotational symmetry to C_2, it still preserves the Fe-As mirror plane symmetries, and so the nematic transition is still sharply defined at the (B_{1g}, A_{1g} strain-tunable) temperature where the Fe-As mirror plane symmetries are broken. At this temperature, the nematic order parameter value goes from zero to nonzero spontaneously, and so it is still described as a thermodynamic phase transition. Conversely, a stress applied in the B_{2g} channel induces a B_{2g} strain which breaks all of the symmetries broken by the nematicity and so induces a finite nematic order parameter even at temperatures far above the zero-stress nematic transition temperature. In this case there isn't really a phase transition when cooling below T_S, but instead a *crossover* happens where the nematic order parameter may become much larger. This distinction becomes very important in measurements involving applied stress because small nonzero values of B_{2g} strain can induce large values of ψ and create anisotropies in many measurable quantities even far above the nematic transition temperature.

5.2 Enhancement of nematicity with B_{2g} strain

In Chapter 6 I discuss the results of my paper, "The transport-structural correspondence across the nematic phase transition probed by elasto-x-ray diffraction" [5]. This paper involves applying in-situ uniaxial stress along the Fe-Fe bonding direction above the nematic transition to induce nematic order. The lattice distortion is measured with x-ray diffraction. Here I demonstrate the decomposition of the lattice response into its $\varepsilon_{A_{1g,1}}$, $\varepsilon_{A_{1g,2}}$ and $\varepsilon_{B_{2g}}$ components.

In Figure 5.2 I present representative data at T=74K, just 0.2K above the nematic transition temperature T_S where the lattice is considerably softened by large nematic fluctuations. Strain was ramped from maximum compression to maximum tension and back, and this loop was repeated a total of three times to measure the a_{or}, b_{or} and c lattice constants. From these terms we can define the unidirectional strains, $\varepsilon_a = \frac{\Delta a_{or}}{a_{or,0}}$, $\varepsilon_b = \frac{\Delta b_{or}}{b_{or,0}}$ and $\varepsilon_c = \frac{\Delta c}{c_0}$. Finally we define three strain terms, $\varepsilon_{B_{2g}} =$

$\frac{1}{2}(\varepsilon_a - \varepsilon_b)$, $\varepsilon_{A_{1g,1}} = \frac{1}{2}(\varepsilon_a + \varepsilon_b)$ and $\varepsilon_{A_{1g,2}} = \varepsilon_c$, which correspond to three irreps of the $\mathrm{D_{4h}}$ point group. The unidirectional lattice constants show the general expected behavior, with ε_a increasing (decreasing) and ε_b and ε_c decreasing (increasing) under tension (compression). However, at this temperature near the nematic transition temperature the nematic fluctuations significantly soften the C_{66} shear modulus, resulting in a strongly nonlinear strain transmission and induced strain response to uniaxial stress. This is further visible in the large slope of the $\varepsilon_{B_{2g}}$ term and the negligible slope of the $\varepsilon_{A_{1g,1}}$ term about zero nominal strain. This demonstrates the importance of simultaneous lattice characterization measurements such as XRD to monitor how the lattice is actually responding to large stresses.

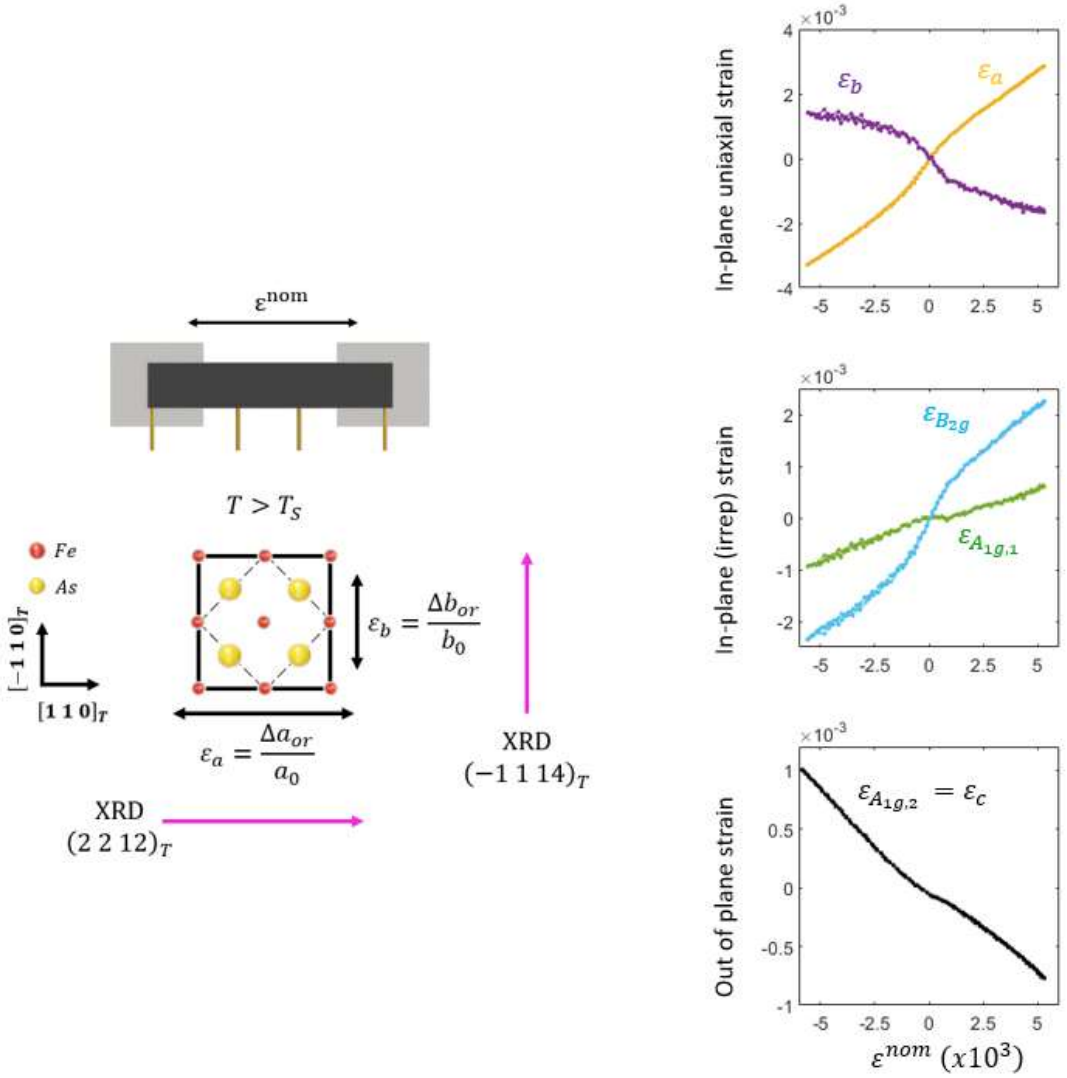

Figure 5.2 Sample of $\mathrm{BaFe_2As_2}$ at T=74K. Uniaxial stress is applied along the tetragonal $[1\ 1\ 0]_T$ which creates uniaxial strains $\varepsilon_a = \frac{\Delta a_{or}}{a_0}$, $\varepsilon_b = \frac{\Delta b_{or}}{b_0}$ and $\varepsilon_c = \frac{\Delta c}{c_0}$ of the a_{or}, b_{or} and c lattice constants,

respectively, with $a_0 = b_0 = 5.5948$ Å and $c_0 = 12.9297$ Å. XRD measurements of ε_a, ε_b and ε_c are used to determine the strain terms $\varepsilon_{B_{2g}} = \frac{1}{2}(\varepsilon_a - \varepsilon_b)$, $\varepsilon_{A_{1g,1}} = \frac{1}{2}(\varepsilon_a + \varepsilon_b)$ and $\varepsilon_{A_{1g,2}} = \varepsilon_c$. Data plotted against the nominal strain ε^{nom} measured from the stress device.

5.3 Intermission: Co-doped $EuFe_2As_2$

We next discuss unpublished data which demonstrates strong strain and magnetic field tuning of superconductivity in a single crystal sample of $\mathrm{Eu(Fe_{0.85}Co_{0.15})_2As_2}$, a doped iron pnictide material with the same crystal structure of $\mathrm{BaFe_2As_2}$ but with Eu atoms instead of Ba between the FeAs planes. Four phase transitions occur in this material, and a clear signature of each transition is apparent in the resistivity vs temperature data from a freestanding sample (Fig.5.3). The sample forms nematic structural domains below $T_S = 66K$, and spin density wave order sets in at $T_{Fe,SDW} = 60K$. At $T_{SC,onset} = 20.5K$, the sample begins a transition into a superconducting state; however, it does not reach a zero resistance state until $T_{SC,0} = 2.5K$. Instead, at $T_{Eu,FM} = 16.9K$ the Eu moments ferromagnetically align along the c-axis. Below this temperature, the nascent superconductivity must compete with both the nematic/SDW order as well as an intrinsic and antagonistic ferromagnetic order. This makes the superconductivity in this temperature range especially tunable with either applied strain or magnetic field.

We discuss both forms of tuning in one single crystal sample mounted to a uniaxial stress device and characterized with x-ray techniques. In the next section we show the suppression of nematicity and accompanying enhancement of superconductivity by uniaxial stress-induced B_{1g} orthorhombicity imaged with XRD. In the following section we show an unusual enhancement of superconductivity with applied magnetic field that can be understood from the reorientation of Eu FM moments to lie along the FeAs planes which is measured with XMCD. The same sample was used for the freestanding resistivity measurement and the XRD and XMCD measurements at APS beamlines 6-ID-B and 4-ID-D, respectively.

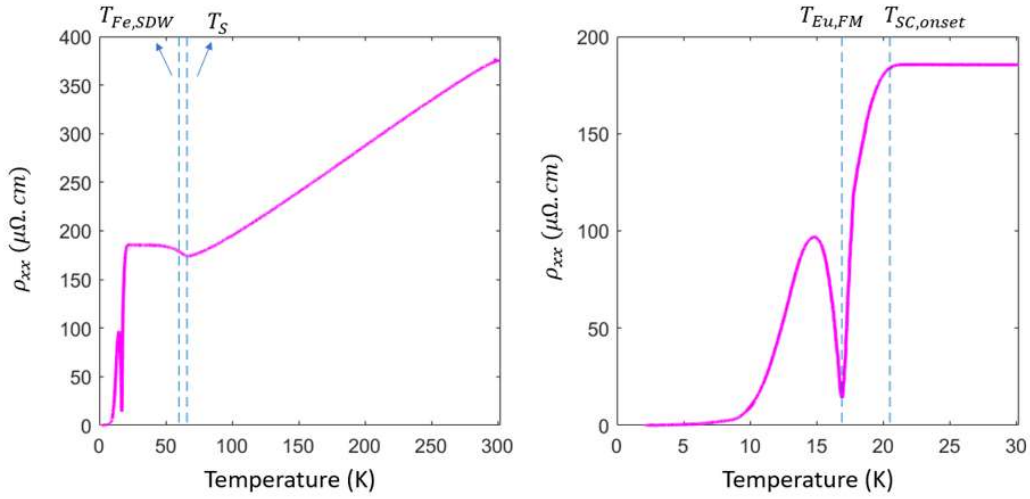

Figure 5.3 Resistivity vs temperature data of freestanding sample with four phase transition temperatures marked by dashed lines.

5.4 Suppression of nematicity with B_{1g} tension

The sample was prepared as a thin bar with transport wires and mounted on a stress device exactly as described in Chapters 6.3 and 7.3 but with the bar cut along the FeAs bonding direction such that uniaxial stress induces B_{1g} orthorhombicity instead of B_{2g} orthorhombicity. This means that an applied stress does not detwin the nematic orthorhombic domains but can instead indirectly control the B_{2g} orthorhombicity magnitude through their mutual coupling to nematicity. In Figure 5.4, resistivity and x-ray diffraction of three lattice constants is presented at T=13.5K. Uniaxial stress was ramped from maximum compression to maximum tension and back (data only collected during tensioning half of the loop), and this loop was repeated a total of three times to measure three reflections. The spontaneous B_{2g} orthorhombicity $\varepsilon_{B_{2g}} = \frac{a_{or}-b_{or}}{a_{or}+b_{or}}$ was measured from the split peak of the $(1\ 1\ 8)_T$ reflection using the same analysis method as discussed in Chapter 6. The stress-aligned a_T lattice constant was measured from the $(1\ 0\ 8)_T$ peak. The transverse-to-stress b_T lattice constant is equal to a_T under zero stress, but without measuring it directly we cannot precisely determine $\varepsilon_{B_{1g}} = \frac{a_T-b_T}{a_T+b_T}$ as a function of strain. However, the response to strain of b_T is expected to be smaller and negatively proportional to a_T as $\Delta b_T = -\eta \Delta a_T$, where $0 < \eta < 1$. Therefore, $\varepsilon_{B_{1g}} = \frac{a_T-b_T}{a_T+b_T} = \frac{1+\eta}{2+(1-\eta)}\left(\frac{\Delta a_T}{a_{T,0}}\right)$ and so $\left(\frac{1}{3}\right)\frac{\Delta a_T}{a_{T_0}} < \varepsilon_{B_{1g}} < \frac{\Delta a_T}{a_{T_0}}$, indicating that the B_{1g} orthorhombicity is of the same order of magnitude as the unidirectional strain of the inline lattice constant. By this same logic, tension is always expected in create a positive value of $\varepsilon_{A_{1g,1}} = \frac{1}{2}\left(\frac{\Delta a_T}{a_{T,0}} + \frac{\Delta b_T}{b_{T,0}}\right)$. The out of plane c lattice constant was measured from the $(0\ 0\ 8)_T$ reflection and used to remove the out of plane components of the above two peaks.

From Figure 5.4, the out of plane lattice constant c is reduced by about 0.085% at maximum tension (and so $\varepsilon_{A_{1g,2}} < 0$) while the stress-aligned lattice constant a_T is increased by about 0.05% at maximum tension (and so $\varepsilon_{B_{1g}} > 0$). As discussed in Chapter 3, below the nematic transition the spontaneous nematic order parameter drives the spontaneous B_{2g} orthorhombicity as $\varepsilon_{B_{2g}} = \frac{\lambda_{B_{2g}}}{C_{66,0}}\psi$, where $C_{66,0}$ is the bare shear modulus. The measured nonzero value of $\varepsilon_{B_{2g}}$ implies a nonzero value of the nematic order parameter ψ. Compared to its zero-stress value of 0.145%, $\varepsilon_{B_{2g}}$ is suppressed by about 0.04% at maximum applied tension, which likewise implies a proportional suppressed value of ψ. The suppression of nematicity benefits the superconductivity, as demonstrated by the large decrease in resistivity to ~20% of its zero stress value at maximum tension. As this is a resistivity measurement in the B_{1g} symmetry channel this is not a resistivity change from domain detwinning (as discussed in Chapters 6 and 7), but instead can be attributed to the enhancement of superconductivity with a suppressed nematicity. Conversely, the resistivity and the B_{2g} orthorhombicity are not similarly decreased with compressive stress, which are both consistent with a maintained nematicity and suppressed superconductivity. It is presently unclear why compression does not result in a similar suppression of $\varepsilon_{B_{2g}}$, but the lattice response to tension and compression are only strictly equivalent in the zero stress limit in the undistorted state, and so structural effects independent of the above discussion may also be at play.

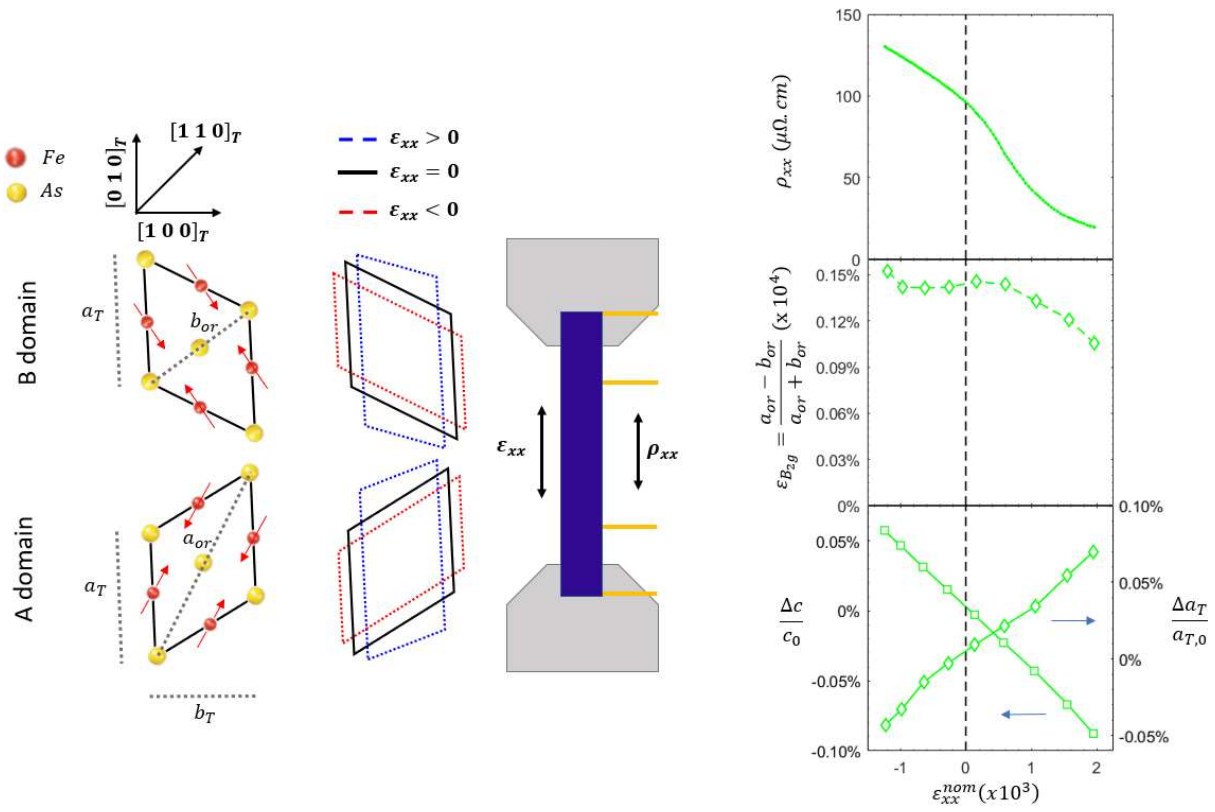

Figure 5.4 At T=13.5K the sample shows two nematic/SDW twin domains (the A and B domain). The sample is oriented on a stress device so that uniaxial stress does not detwin between the two domains but can change the orthorhombicity magnitude (blue and red dotted lines for tension and compression respectively). ρ_{xx} and XRD measurement of three lattice constants (converted into strain terms) plotted vs nominal strain.

5.5 Reorientation of Eu ferromagnetic order parameter with applied magnetic field

Below the Eu ferromagnetic ordering, Co-doped $EuFe_2As_2$ exhibits the rare phenomena of field-induced superconductivity, in which an in-plane applied field decreases the resistivity [85]. This is hypothesized to occur due to reducing the flux from Eu moments through the FeAs superconducting planes by reorienting Eu moments to lie along the FeAs planes. As demonstrated in the previous section, applied stress can tune the competition between superconductivity and nematicity to the benefit of superconductivity. In this section we show that similar strain tuning does not appear to tune the field-induced superconductivity or the susceptibility and magnetization of Eu moments. We continue the study of the same sample discussed in the previous section. Here, we use a magnetic field applied along the tetragonal $[0\ 1\ 0]_T$ direction to reorient the $\hat{c}$-axis aligned ferromagnetic moment of the Eu layers to lie in-plane along the field direction, i.e. in-plane perpendicular to the $[0\ 1\ 0]_T$ strain axis and at approximately 45 degrees to the$[1\ 1\ 0]_T$ Fe nematic and SDW direction (Fig.5.5a). This is accomplished by an in-plane applied magnetic field along $[0\ 1\ 0]_T$. The in-plane Eu moment size is measured with

XMCD on the Eu L_3 edge using the same experimental setup as described in Chapter 7. XMCD is a powerful tool to study ferromagnetic superconductors as it is really an element-specific electronic transition rate measurement and so it bypasses any diamagnetic shielding from the superconductivity.

Figure 5.5c shows XMCD results under 5 strain states over a magnetic field range from 0T to 0.8T. The Eu in-plane moment is initially zero with zero applied field. An increasing field linearly increases the in-plane moment towards saturation at 0.27T. There is no apparent strain-induced change in either the saturation field value or saturation XMCD value (i.e. the saturated magnetization). This can be further understood from considering the half-filled Eu 4f orbitals responsible for the ferromagnetic moments, which have no orbital component (L=0) and so should have an isotropic response to field with minimal response to distortions in the crystal lattice.

Despite the indifference of Eu magnetic order to strain, the resistivity is substantially changed with strain and field. In Figure 5.5b, strain tunes the zero-field resistivity but does not put the system into a superconducting state. For each strain state, an applied field reduces the resistivity substantially with a minimum at 0.27T, before increasing at higher fields. This minimum in resistivity thus corresponds to the full saturation of Eu moments in-plane. For the highest tensile strain state, the resistivity reaches a zero-resistance state at 0.21T up to 0.5T. Therefore, through a combination of magnetic field and uniaxial stress, superconductivity could be induced at a higher temperature than could be attained by either tuning parameter alone (at least at these achieved strain and magnetic field ranges). This demonstrates the power of multiple simultaneous tuning parameters to create new states in a complex quantum material.

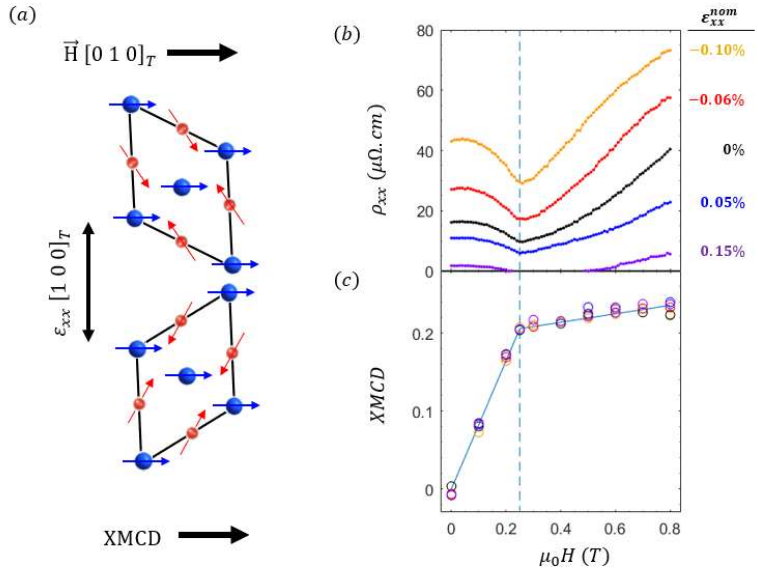

Figure 5.5 (a) Schematic of the A and B nematic domains and Fe moments (red) after a full saturation of Eu moments (blue) in-plane. Eu atoms are coordinated directly above and below As atoms and so we represent the Eu moments on the usual As sites. (b) Resistivity vs applied magnetic field for 5 fixed strain values at 10K. For the highest tensile state (purple) the sample has zero resistance between 0.21T and 0.5T. (c) Simultaneous Eu in-plane XMCD value for the 5 strain states. Dotted line shows saturation field, solid line is a guide to the eye.

Chapter 6:
The Transport-Structural Correspondence to Nematicity

6.1 Abstract:

This chapter covers the topics from my first first-author paper, "The transport-structural correspondence across the nematic phase transition probed by elasto-x-ray diffraction". The key idea of this project is to examine whether the transport coefficient associated with nematicity, the resistivity anisotropy, really does act as an effective proxy for nematic order, especially below the nematic transition where the nematic order parameter becomes large spontaneously (i.e. in the absence of applied fields). I discuss details of the experiment which involve the combination of applied in-situ tunable uniaxial stress, transport measurements, and x-ray diffraction. In both the purely nematic phase and in the high-temperature disordered phase I measure one transport quantity and one structural quantity and show that the transport-structural ratio is relatively constant across temperature and across phase. This implies that the nematic coupling to both the conduction electrons and to the lattice remains constant across this temperature range and phase transition. Finally, I show a comparison of elastoresistivity and shear modulus data from two previously published papers across the underdoped side of the phase diagram to show that this transport-structural nematic coupling actually diverges towards the optimal doping, which has implications for the nematic fluctuation enhancement of superconductivity.

6.2 Introduction: Thermodynamic order parameters and transport coefficients

If you were to ask many people what they think is the single most defining feature of a superconductor, the vast majority would say that it is the zero resistance state. Indeed, this is the feature that gives the phenomena its name. A handful of condensed matter physicists may instead say that the defining feature is the Meissner effect, in which magnetic fields are expelled from the bulk of the material. These two features are interesting to those of us who live outside the superconducting crystal and try to interact with it externally. However, if you were to ask the conduction electrons living inside the crystal this same question, they would say that what defines superconductivity is the presence of an electron condensate formed by Cooper pairs. In fact, in their ground state the electrons aren't even aware of the concept of resistivity, which (ignoring exactly quantized topological transport) is really a macroscopic effective quantity that only comes into play when an applied field or thermal gradient moves the system into a nonequilibrium state and causes an electric current to flow in response. Further, resistivity is not a thermodynamic quantity, and it does not enter into the electron Hamiltonian or the free energy. It is important when thinking about any phase transition to remember that electrons do not interact to form new phases in anticipation that a conjugate field may someday be applied to them, and they certainly do not form new phases with plans to have specific transport properties. Fundamentally, phase transitions occur as the system attempts to lower its internal energy, with specific transport properties and responses to applied fields resulting as unintended byproducts.

However, from the field tuning and transport behavior we can learn many details about the nature of the phases and how measurable quantities couple to the thermodynamic order.

To understand the results of this chapter, it is crucial to differentiate between the true thermodynamic order parameter, its conjugate field, and its associated transport quantity. We briefly review the definitions of each in the context of nematicity in iron pnictide materials. First, as discussed in Chapter 3, we do not have a definite microscopic description of the nematic order parameter and instead represent it as a phenomenological order parameter ψ with $\mathrm{B}_{2\mathrm{g}}$ symmetry. Its true conjugate field is likewise undefined, but through the nematic-elastic coupling the in-plane $\mathrm{B}_{2\mathrm{g}}$ lattice orthorhombicity $\varepsilon = \frac{a-b}{a+b}$ acts as an effective conjugate field, with a and b defined as the lattice constants of the 4-Fe unit cell. The transport quantity is the resistivity anisotropy $\eta = \frac{\rho_a - \rho_b}{\rho_a + \rho_b}$, with ρ_a and ρ_b defined as the resistivities along the a and b lattice directions (Figure 6.1b). We assign a phenomenological linear coupling between the resistivity anisotropy and the nematicity as $\eta = k\psi$, so that whenever the nematicity becomes nonzero a resistivity anisotropy is also induced. We also need to consider the nematic coupling to the lattice, but this relationship is different in the two phases. Below the transition, the nematic ordering drives the spontaneous orthorhombicity, with a relationship as $\varepsilon = \frac{\lambda}{C_{66,0}}\psi$. Above the transition we consider applying stress to induce a lattice distortion and then via the linear nematic-elastic coupling induce nematic order; we express this with the nematic susceptibility, $\frac{d\psi}{d\varepsilon} = \frac{\lambda}{a_0(T-T^*)}$. This nuance makes clear one major difference between the conjugate field and the transport coefficient; you cannot "create" a transport anisotropy which then induces nematic order, but you can create an orthorhombic lattice distortion by applying stress which *does* induce nematic order.

A major focus of this chapter is to demonstrate that the nematic-transport proportionality coefficient k is constant across temperature and across the nematic transition, implying that whatever the nature of nematic coupling to conduction electrons, this coupling is unchanged with temperature and between nematically ordered and disordered phases. This strong correspondence could be assumed in the disordered phase on symmetry grounds but is not guaranteed to occur below the transition when the order parameter becomes large. As the nematic order parameter ψ and the resistivity anisotropy η belong to the same irreducible representation of the high symmetry point group, they are linear proportional in the infinitesimal strain limit [86]. Nevertheless, the resistivity is not a thermodynamic variable and depends on extrinsic properties such as disorder[87]–[90]. While numerous studies using x-ray and neutron diffraction have seen the continuous onset of nematicity via structural diffraction peaks, the (zero-stress) spontaneous resistivity anisotropy has never been precisely measured through the transition. Therefore, a key and very general question is to what extent a transport coefficient can represent the order parameter beyond the infinitesimal limit. This question is especially important for 2D systems such as graphene where thermodynamic measurements are difficult [91].

In this chapter we examine this question in a model system for the study of nematic phase transitions, the iron pnictide superconductor [4], [92]. Because of the electron-lattice coupling, the nematicity in iron-pnictides has been clearly observed in both transport anisotropy and structural thermodynamic variables (schematically displayed in Figure 6.12a). Above the phase transition, the

diverging nematic susceptibility can be seen in the Curie-Weiss temperature dependence of both the $2m_{66}$ elastoresistivity coefficient[55] and the softening of the shear modulus[53] C_{66}. Below the phase transition, the nematic order parameter also generates a large spontaneous resistivity anisotropy η_S [39], [93] and a spontaneous structural distortion ε_S [45], [63]. Each of these four quantities are usually measured separately due to incompatible sample preparation needed for standard techniques, which makes a quantitative comparison difficult. In particular, the spontaneous resistivity anisotropy η_S is notoriously difficult to measure close to the phase transition, because the stress required to detwin the sample always induces additional resistivity anisotropy due to the softening of C_{66} and the divergence of $2m_{66}$. To our knowledge, no study of iron pnictides has ever reported any two of the above quantities within a single sample. In this work, we perform measurements of $2m_{66}$, C_{66}, η_S and ε_S using the technique of elasto x-ray diffraction all within one single crystal sample of $\mathrm{Ba(Fe_{0.96}Co_{0.04})_2As_2}$, located on the underdoped side of the phase diagram with $T_S = 73.8$ K, $T_N = 64$ K and $T_C = 13$ K (Fig. 6.1a). With our unprecedented multi-modal measurement, we show the four quantities perfectly follows a mean-field temperature dependence. Furthermore, the ratio of transport to structural quantities is a constant across the phase transition, suggesting that the resistivity anisotropy behaves just like a thermodynamic variable even for large values of the nematic order parameter. While the $2m_{66}$, C_{66}, η_S and ε_S can be well described by the Landau free energy framework, two unexpected findings stand out. First, using the C_{66} and $2m_{66}$ data from the previous studies[55], [68], we discovered a strong doping dependence of the ratio between transport and structural quantities, increasing by more than fivefold towards optimal doping. Second, when driving the system deep into the non-linear regime with large uniaxial stress, we found that the resistivity anisotropy shows a non-saturating behavior that is drastically different from the dampened response of the lattice. Possible implications of these two unusual phenomena are discussed.

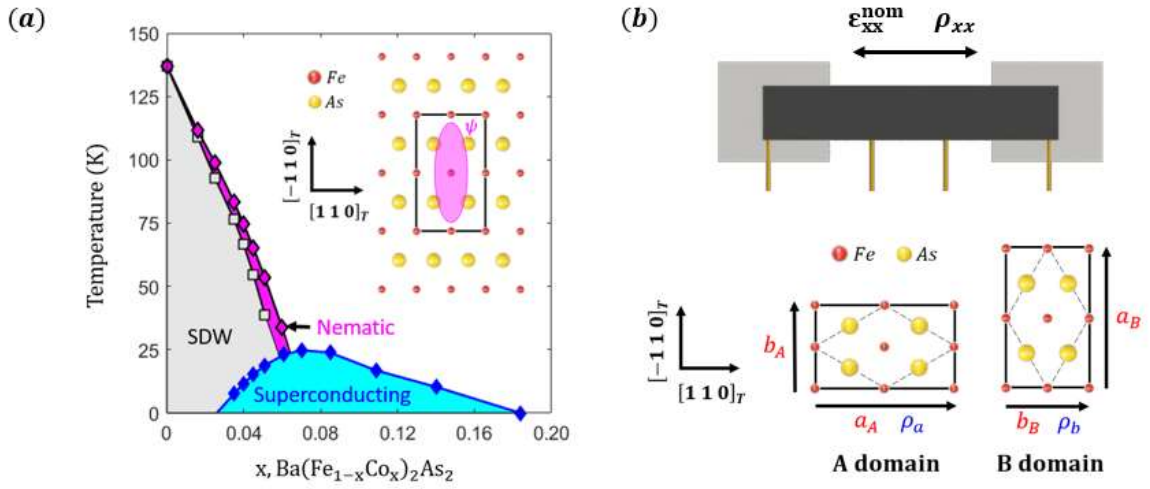

Figure 6.1 Nematic-elastic-transport coupling. (a) *x-T* phase diagram of Co-doped $BaFe_2As_2$. Inset is a representation of the nematic order parameter ψ (magenta) aligned with the in-plane orthorhombicity ε (black). (b) Schematic of the sample measurement geometry and strain device. Uniaxial stress is applied

along the tetragonal $[1\ 1\ 0]_T$ direction. Inline resistivity ρ_{xx} measures ρ_a of the A domain and ρ_b of the B domain.

6.3 Elasto X-Ray Diffraction

In order to simultaneously assess the electronic and structural response to stress in a single crystal sample, we have developed a new experimental platform, the elasto X-ray diffraction (elasto-XRD), that combines electrical transport with *in-situ* uniaxial stress tunability via a Razorbill CS-100 strain device[94] fully integrated with x-ray diffraction (XRD) measurements at beamline 6-ID-B at the Advanced Photon Source (Fig.6.2). This platform allows us to measure the lattice constants, orthorhombic twin domain populations, and electrical resistivity simultaneously while the uniaxial stress is continuously tuned to detwin the sample and enhance the orthorhombicity. Here we review details of the sample preparation.

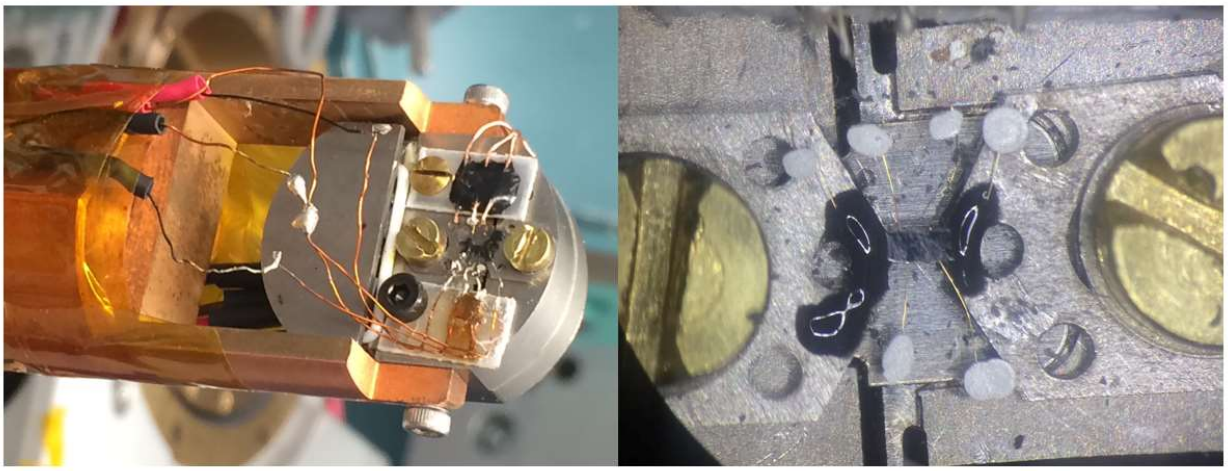

Figure 6.2 Pictures from the experiment at Argonne National Laboratory. (left) The Razorbill CS-100 mounted to a cold find cryostat. (right) the single crystal sample mounted on titanium plates.

Single crystal samples of $Ba(Fe_{.96}Co_{.04})_2As_2$ were grown from an FeAs flux as described elsewhere [55]. The primary sample used in x-ray measurements was prepared as a thin bar of dimensions 2.0 x 0.57 x 0.07 mm and cut along the Fe-Fe bonding direction. Gold wires were glued with DuPont 4929 silver epoxy underneath the sample to not obstruct the x-ray diffraction off the top surface of the crystal. Measurements of the resistivity coefficient ρ_{xx} aligned along the stress axis were performed using a standard 4-point measurement and an SR830 lock-in amplifier. Uniaxial stress was

applied along the tetragonal $[1\ 1\ 0]_T$ direction ($\hat{x}$). The nominal strain is defined as $\varepsilon_{xx}^{nom} = \frac{\Delta L}{L_0}$, where L_0 is the size of the gap between two titanium plates on which the sample was glued with Stycast epoxy. The displacement ΔL was determined from a capacitance strain gauge. The four-wire electrical contact geometry enables the simultaneous resistance measurements along the stress axis.

X-ray diffraction (XRD) measurements were performed at the Advanced Photon Source, beamline 6-ID-B, at Argonne National Laboratories. X-rays of energy 11.215 keV illuminated an area 500x500 um, fully encompassing a cross section of the middle of the crystal where strain transmission is highest. The sample and strain device were mounted on a closed cycle cryostat. Gaussian fits to the tetragonal $(2\ 2\ 12)_T$, $(-1\ 1\ 14)_T$ and $(0\ 0\ 14)_T$ reflections were used to determine the orthorhombic lattice constants in the direction of applied stress (a for $T > T_S$; a_A & b_B for $T < T_S$), in-plane transverse to the stress (b for $T > T_S$; a_B & b_A for $T < T_S$) and normal to the plane (c), corresponding to the $\hat{x}$, $\hat{y}$, and $\hat{z}$ directions, respectively.

All data was collected following a single procedure. At fixed temperatures from 66 K to 140 K, XRD and transport measurements were made by ramping strain from maximum compression to maximum tension and back while measuring a single reflection (i.e. $(2\ 2\ 12)_T$), then this strain loop was repeated for each of the other reflections. The same device voltages were applied through each range. During these loops, both the nominal strain ε_{xx}^{nom} and the resistivity ρ_{xx} were measured. At all temperatures, the ρ_{xx} vs ε_{xx}^{nom} curves are nearly identical for multiple sweeps of voltage on the stress device, implying repeatability of the attained strain state during the measurement of the 3 reflections (Example: 74K Fig.6.3).

One concern with this methodology is that the sample may not actually return to the same experienced strain state across the tension and compression loops or over many loops, resulting in strain offsets between nominal and experienced strain states that would make it more difficult to compare the XRD data between different loops. An alternative methodology would be to measure multiple reflections while the sample is held at a single fixed nominal strain value, to ensure that all lattice constants are determined in the same strain state. However, rotating the sample and detector to reach multiple peaks at each strain step increases the time of each measurement substantially and also introduces the issue of relocating the peak intensity lineup conditions upon return to each reflection, as small misalignments can occur from repeated rotations. Therefore, the fixed temperature multiple strain loop methodology was chosen.

We show now that the possible strain offsets between nominal and experienced strain states must be extremely small. Our most sensitive gauge of the attained strain state throughout the bulk of the sample is the resistivity; for instance, at 74K under compression the resistivity change to nominal strain is about a factor of 40, while the in-plane lattice constant change with nominal strain measured by XRD is about a factor of $\frac{1}{2}$. Zooming in on this most strain-sensitive range of the data, we find that the resistivity data is indistinguishable between the three loops, and all points reside within a tight 95% confidence interval based on the combined data set (dashed lines, see Supplementary Information of ref.[5] for more information).

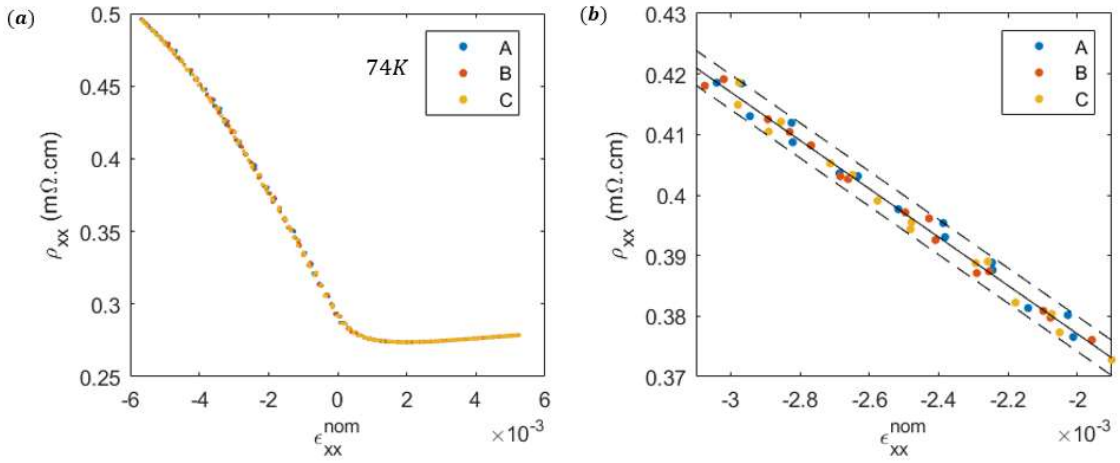

Figure 6.3 (a) Resistivity vs nominal strain at 74K. A, B and C refer to separate strain loops at fixed temperature during the measurement of the $(2\,2\,12)_T$, $(-1\,1\,14)_T$ and $(0\,0\,14)_T$ reflections, respectively. (b) A small strain range of (a) showing the distribution of resistivity points. Solid line shows a linear fit, dashed line a 95% confidence interval for the combined dataset.

6.4 Nematic fluctuation divergence: shear modulus and elastoresistivity

We focus first on the structural and electronic response to applied stress above the nematic transition, where there are no orthorhombic domains. We define $\varepsilon_{xx} = \frac{\Delta a}{a_0}$ and $\varepsilon_{yy} = \frac{\Delta b}{b_0}$ as the XRD-measured strains of the inline $([1\,1\,0]_T)$ and transverse $([-1\,1\,0]_T)$ lattice constants, respectively (see Fig.5.2). At 130 K the lattice constants show a nearly linear response to ε_{xx}^{nom}, while just above the transition at 74 K the response becomes strongly nonlinear, with an enhanced response at $\varepsilon_{xx}^{nom} = 0$. This results in the strain transmission $\frac{d\varepsilon_{xx}}{d\varepsilon_{xx}^{nom}}$ and the induced B_{2g} orthorhombicity $\varepsilon = \frac{1}{2}(\varepsilon_{xx} - \varepsilon_{yy})$ becoming increasingly nonlinear with cooling (Fig.6.4).

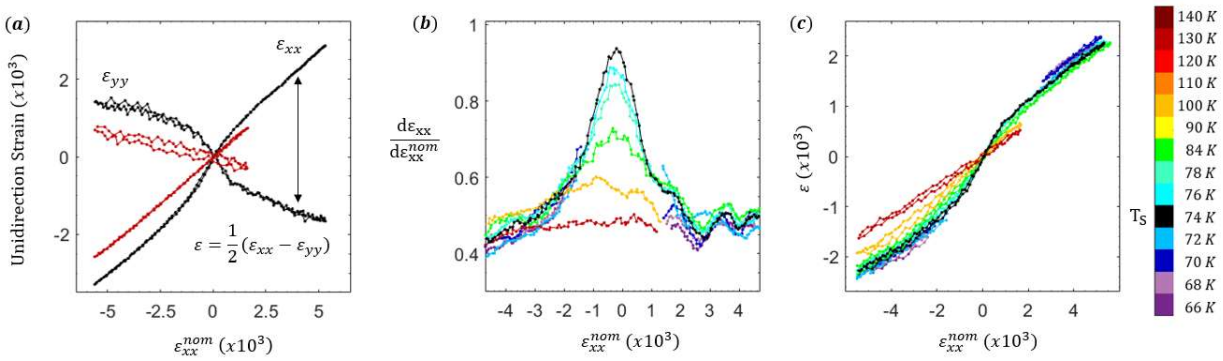

Figure 6.4 (a) Unidirectional lattice constant strains ε_{xx} and ε_{yy} vs nominal strain ε_{xx}^{nom}at $T = 74\ K$ (black) and 130 K (red). (b) Strain transmission $\frac{d\varepsilon_{xx}}{d\varepsilon_{xx}^{nom}}$ and (c) in-plane orthorhombicity $\varepsilon = \frac{1}{2}\left(\varepsilon_{xx} - \varepsilon_{yy}\right)$ across several measured temperatures. For (b) and (c), data within nematic phase plotted only in the high-strain fully detwinned regime.

The rate of change of the in-plane transverse strain to inline strain $\frac{d\varepsilon_{yy}}{d\varepsilon_{xx}}$ approaches a peak value of -1 with cooling to T_S and decreases to its high-temperature value at large ε (Fig.6.5a). We extract the shear modulus from Poisson's ratio ($\nu_{xy} = -\frac{d\varepsilon_{yy}}{d\varepsilon_{xx}}|_{\varepsilon=0}$) using $C_{66} = (50.5\ GPa)\frac{1-\nu_{xy}}{1+\nu_{xy}}$, where the magnitude is determined from other elastic modulus terms using ultrasound data from ref.[68] (see Chapter 9.2). In Figure 6.5b, C_{66} diminishes to nearly zero at T_S (black dots). Fitting C_{66} with a Curie-Weiss temperature dependence, $C_{66} = C_{66,0} - A(T - T^*)^{-1}$ (red line, $R^2 > .98$), yields a fitted value of the bare shear modulus $C_{66,0} = 38.8 \pm 4.7$ GPa in agreement with the high-temperature ultrasound data[68]. The extracted bare nematic transition temperature, $T^* = 50K \pm 8.3K$ is considerably larger than the values obtained from several other shear modulus measurements[43], [46], [53], [54], where $T_S - T^* \sim 40K - 50K$, yet as we discuss below it agrees well with the T^*obtained from the simultaneous elastoresistance measurement. We note that a major difference is that in the previously reported measurements C_{66} is reduced but nonzero at the transition, possibly due to local strain inhomogeneities and resulting domain microstructures adding a small background signal near the transition[43]. Since C_{66} varies most rapidly near the transition, this difference may strongly influence the Curie-Weiss fitting, hence the discrepancy in T^*.

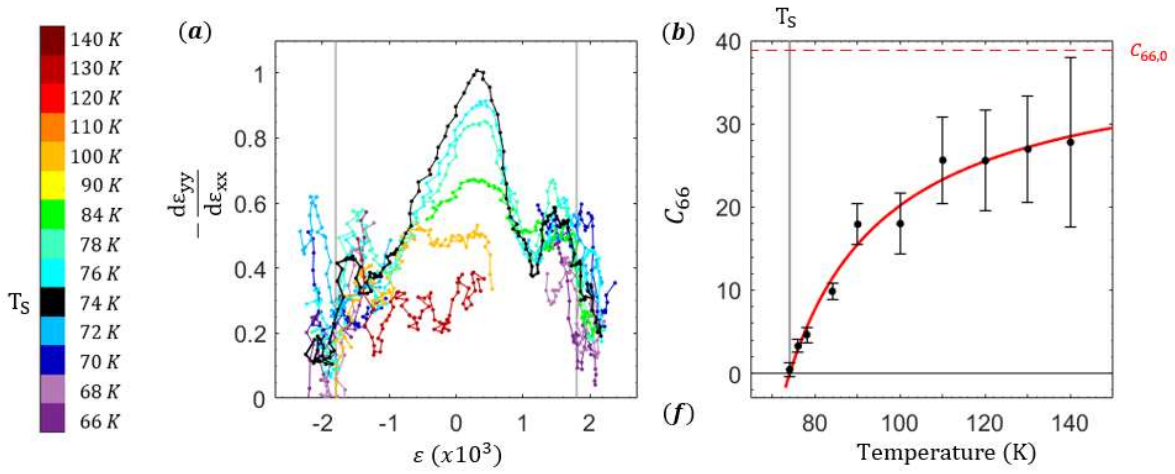

Figure 6.5 (a) The rate of change of in-plane unidirectional strains $-\frac{d\varepsilon_{yy}}{d\varepsilon_{xx}}$ vs ε. (b) The shear modulus C_{66} extracted from $-\frac{d\varepsilon_{yy}}{d\varepsilon_{xx}}|_{\varepsilon=0}$. Grey lines in (a) show the 8 K zero-stress value of in-plane orthorhombicity, $\varepsilon = 0.18\%$. Red line in (b) is Curie-Weiss fit $C_{66} = C_{66,0} + A\left(\frac{1}{T-T^*}\right)$ with fit values: $T^* = 50.0K \pm 8.3K$, $A = -933 \pm 51$ GPa K, $C_{66,0} = 38.8 \pm 4.7$ GPa, $R^2 = 0.98$.

We next turn to the resistivity response to strain. The resistivity ρ_{xx} vs ε_{xx}^{nom} is increasingly nonlinear with cooling (Fig.6.6a). In particular, near the phase transition ρ_{xx} shows a kink-like behavior as ε_{xx}^{nom} increases from zero to positive, and an inflection point at large negative values of ε_{xx}^{nom}. Intriguingly, while still being nonlinear, the kink and inflection point of ρ_{xx} vanish when plotted against the simultaneously measured orthorhombicity ε (Fig.6.6b), and ρ_{xx} can be well fitted by a 2nd order polynomial (Fig.6.7). This stark contrast indicates that the anomalies observed in ρ_{xx} vs ε_{xx}^{nom} are artifacts of the nonlinear strain transmission, highlighting the importance of in-situ x-ray measurements. The 2nd order polynomial can be understood from a symmetry analysis by decomposing the inline resistivity dependence on the B_{2g} orthorhombicity as

$$\rho_{xx}(\varepsilon) = \rho_0\left(1 + m_{B_{2g}}^{B_{2g}}\varepsilon + m_{A_{1g}}^{B_{2g},B_{2g}}\varepsilon^2\right)$$

where $m_{B_{2g}}^{B_{2g}} = 2m_{66}$ is the linear coefficient with (odd) B_{2g} symmetry and $m_{A_{1g}}^{B_{2g},B_{2g}}$ is the quadratic coefficient with (even) A_{1g} symmetry. Consistent with previous work [95], $m_{A_{1g}}^{B_{2g},B_{2g}}$ has a large magnitude near the transition. As we cannot perform a simultaneous bidirectional transport measurement with this setup, we isolate the B_{2g} component and extract the $2m_{66}$ elastoresistivity coefficient at each temperature using $2m_{66} = \frac{d}{d\varepsilon}\left(\frac{\Delta\rho_{xx}}{\rho_0}\right)|_{\varepsilon=0}$, which diverges toward the transition (Fig.6.6c). We analyze this temperature dependence with the same Curie-Weiss model as used for the shear modulus and find it is well described with a similar $T^* = 48.9K \pm 7.1K$ (Fig.6.6c, blue line, $R^2 > .95$). Therefore, we demonstrate that both $2m_{66}$ and C_{66} within a single sample show the same mean-

field temperature dependence, confirming both have a linear proportionality to a common driver, namely the nematic fluctuations.

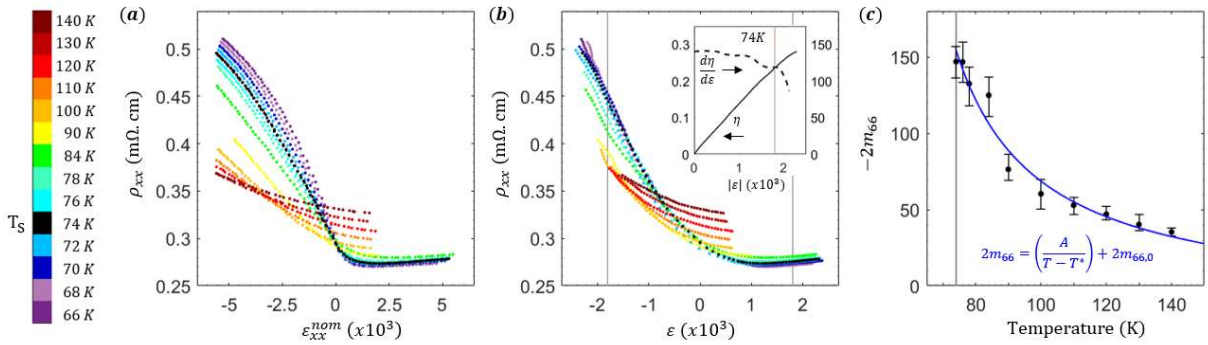

Figure 6.6 (a) Longitudinal resistivity ρ_{xx} vs ε_{xx}^{nom} and (b) vs ε . Inset to (b) shows the resistivity anisotropy $\eta = \frac{\rho_{xx}(\varepsilon)-\rho_{xx}(-\varepsilon)}{\rho_{xx}(\varepsilon)+\rho_{xx}(-\varepsilon)}$ and the derivative $\frac{d\eta}{d\varepsilon}$ at $T = 74$ K. (c) The $2m_{66}$ elastoresistivity extracted from $\frac{d\rho/\rho_0}{d\varepsilon}|_{\varepsilon=0}$. Grey lines in (b) show the 8 K zero-stress value of in-plane orthorhombicity, $\varepsilon = 0.18\%$. Blue line in (b) is Curie-Weiss fit $2m_{66} = 2m_{66,0} + A\left(\frac{1}{T-T^*}\right)$ with fit values $T^* = 48.9K \pm 7.1K$, $A = 4237 \pm 330$, $2m_{66,0} = -14.3 \pm 8.5$, $R^2 = 0.95$.

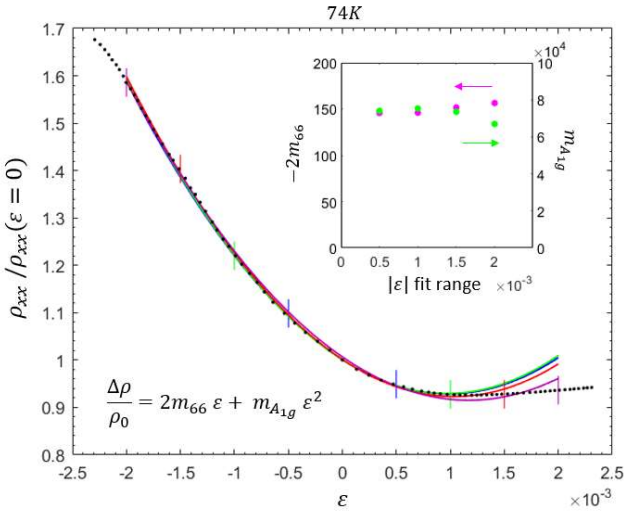

Figure 6.7 The zero-stress normalized resistivity $\frac{\rho}{\rho_0}$ vs in-plane orthorhombicity ε. A quadratic fit is made across 4 fitting ranges ($\pm 0.05\%$, $\pm 0.10\%$, $\pm 0.15\%$, and $\pm 0.20\%$ marked by blue, green, red and

purple fit lines and colored bars) with fit magnitudes of the linear ($2m_{66}$) and quadratic ($m_{A_{1g}}$) terms largely stable over different fitting ranges (inset).

While the $2m_{66}$ and C_{66} extracted near the zero-strain limit show good agreement with mean field behavior, it is no longer the case in the large strain limit where nematic fluctuations are expected to be heavily dampened. The Figure 6.6b inset shows the resistivity anisotropy $\eta = \frac{\rho_{xx}(\varepsilon)-\rho_{xx}(-\varepsilon)}{\rho_{xx}(\varepsilon)+\rho_{xx}(-\varepsilon)}$ (defined as the normalized resistivity difference at equal in-plane orthorhombicity between tension and compression) and its strain derivative $\frac{d\eta}{d\varepsilon}$ which corresponds to the induced nematic order parameter and nematic susceptibility at finite strain (note that $\frac{d\eta}{d\varepsilon}|_{\varepsilon=0} = \frac{d}{d\varepsilon}\left(\frac{\Delta\rho_{xx}}{\rho_0}\right)|_{\varepsilon=0} = 2m_{66}$). At temperatures near or below T_S, η shows no sign of saturation as ε exceeds 0.18% (the spontaneous orthorhombicity at T = 8 K, which is also the maximum value of spontaneous orthorhombicity for this doping concentration). This non-saturating behavior is in sharp contrast to the structural counterpart, where $\frac{d\varepsilon_{yy}}{d\varepsilon_{xx}}$ dampens rapidly towards its high temperature value (Fig.6.5a). Although in the large-stress limit $\frac{d\varepsilon_{yy}}{d\varepsilon_{xx}}$ and $\frac{d\eta}{d\varepsilon}$ no longer simply relate to C_{66} and $2m_{66}$, which are response functions defined in the zero-stress limit, the striking difference between $\frac{d\varepsilon_{yy}}{d\varepsilon_{xx}}$ and $\frac{d\eta}{d\varepsilon}$ is unexpected. This peculiar finding will be revisited in section 6.7.

6.5 Spontaneous Elastoresistivity and precision detwinning of orthorhombic domains

Next, we extract the spontaneous orthorhombicity ε_S and spontaneous resistivity anisotropy η_S in the nematic ordered phase. We focus on the 10 K range below T_S but above T_N because the long-range antiferromagnetic order induces shifts in the orthorhombicity [45], [63] and reconstructs the Fermi surface leading to additional resistivity anisotropy effects [96]–[99]. Upon cooling the sample below $T_S = 73.8K$, the single peak of the $(2\ 2\ 12)_T$ reflection splits into two peaks corresponding to the a_A and b_B orthorhombic lattice constants of the A and B domains, respectively, indicating the formation of structural twin domains (Fig.6.8a). As is often done for a freestanding crystal [45], we define the spontaneous orthorhombicity as $\varepsilon_S = \frac{a_A - b_B}{a_A + b_B}$ in the zero-stress limit. Within the purely nematic phase, ε_S is well fitted to a mean-field $\sqrt{T_S - T}$ temperature dependence, with fit parameters $\varepsilon_S = A\sqrt{73.8\ K - T}$, $A = .000290 \pm .0000006$, $R^2 = 0.99$ (Fig.6.8f).

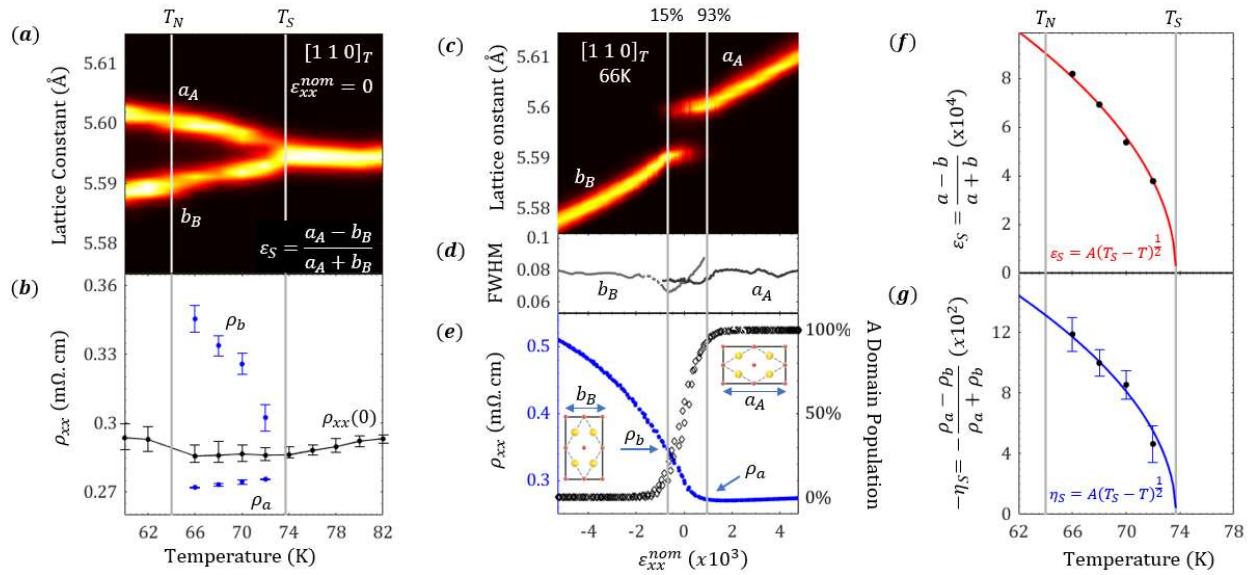

Figure 6.8 Spontaneous resistivity anisotropy and orthorhombicity. (a) Zero-stress x-ray diffraction of the $[1\,1\,0]_T$ lattice constants across the nematic (T_S) and antiferromagnetic (T_N) transitions. (b) The zero-stress twinned state resistivity ρ_{xx} (black) and the detwinned monodomain resistivities ρ_a and ρ_b (blue) extracted from the $D_A = 90\%$ and 10% points in (e). (c) X-ray diffraction of the $[1\,1\,0]_T$ lattice constants a_A and b_B with intensities I_A and I_B. (d) The full-width half maximum (FWHM) of the Gaussian fit to the XRD peak for both a_A and b_B. (e, right) Relative A domain population, $D_A = \frac{I_A}{I_A + I_B}$. Grey bars at $D_A = 15\%$ and $D_A = 93\%$. (e, left) Inline resistivity with monodomain resistivities ρ_a and ρ_b at $D_A = 93\%$ and $D_A = 15\%$. (f) The spontaneous orthorhombicity ε_S and (g) the spontaneous resistivity anisotropy η_S are both well fit to a $\sqrt{T_S - T}$ temperature dependence within the nematic phase with $T_S = 73.8K$.

The presence of twin domains cause transport measurements to average over the resistivities along the two domain directions. This presents a substantial experimental challenge to obtaining the resistivity anisotropy of the orthorhombic unit cell, which we overcome by precisely strain detwinning the sample. Figure 6.8c-e shows detwinning results for a representative temperature (66 K). The peak positions and intensities (I_A and I_B) are shown in Figure 6.8c. Strain homogeneity is confirmed by a nearly constant Bragg peak width throughout the nominal strain range (Fig.6.8d). The relative volume fraction of the A domain is determined as $D_A = \left(\frac{I_A}{I_A + I_B}\right) \mathrm{x}\, 100\%$, which varies smoothly between 0% and 100% with applied stress, i.e. between the B and A monodomains (Fig.6.8e, right). While the sample is mostly detwinned over a relatively small strain range, the last 10% volume fraction of the minor domain is detwinned over larger strain values where the inline lattice constant becomes highly susceptible to applied strain. Therefore, we find that we can mostly, but not fully, detwin the sample without inducing additional lattice distortions, which warrants consideration for the design and interpretation of future experiments involving uniaxial stress detwinning of structural domains.

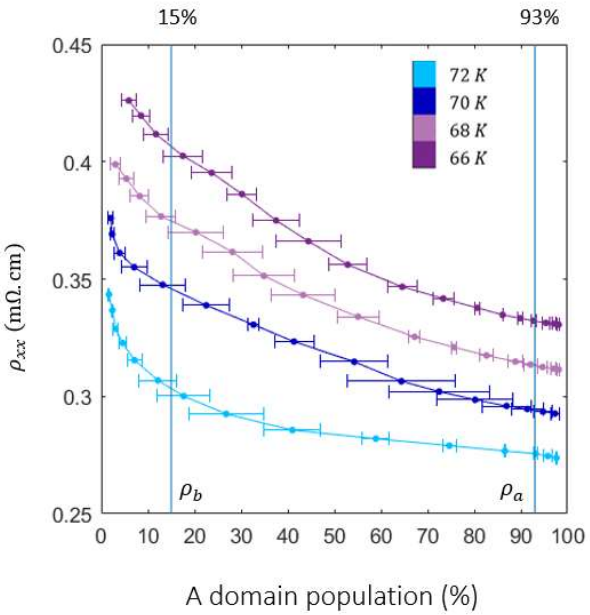

Figure 6.9 Resistivity vs average A domain population. Edges of error bars show the two as-measured values of D_A between the tensile and compressive strain loops. Data offset by 0.05 for each temperature for clarity.

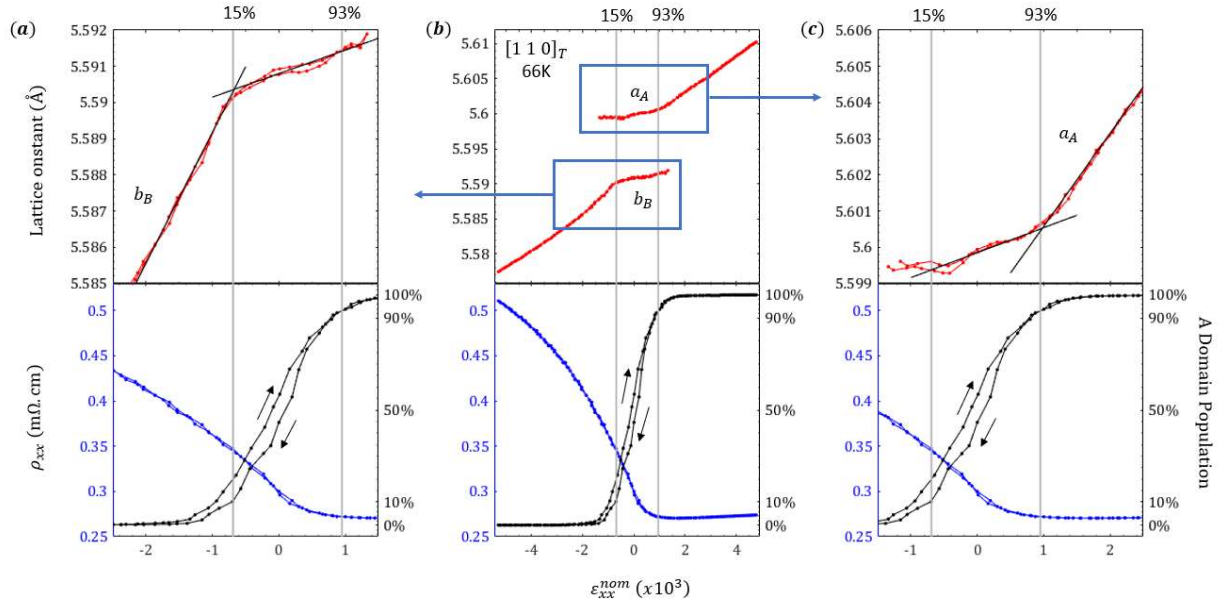

Figure 6.10 Same data as in Figure 6.8c-e plotted at different strain ranges. (b) Full strain range. (c) Tensile strain range, a_A lattice constant. (c) Compressive strain range, b_B lattice constant. Grey bars show the 15% and 93% (averaged) A domain population points, beyond which the lattice constants become strongly susceptible to strain. Black lines are linear fits to lattice constants.

The spontaneous resistivity anisotropy $\eta_S = \frac{\rho_a - \rho_b}{\rho_a + \rho_b}$ results from the different resistivities along the $\hat{a}$ and $\hat{b}$ directions, ρ_a and ρ_b. Due to the network of twin domains running at 45° to the length of the sample [57], the current takes nontrivial paths which results in a nonlinear dependence of ρ_{xx} on D_A (Fig.6.9). We approach the problem from two directions. First, we start in a zero nominal strain state and detwin the sample just until the lattice begins to deform (at 85% and 93% full detwinning to the compressive B and tensile A domains, respectively; see Fig.6.10). This is the closest condition to a single domain state without lattice distortion that we can achieve experimentally. The extracted ρ_a and ρ_b (Fig.6.8b) yield values of η_S which are well fit to $\sqrt{T_S - T}$ (Fig.6.8g).

Alternatively, we can extract η_S by starting in the fully-detwinned regime and linear fitting the resistivity anisotropy η down to ε_S. The resulting values of η_S are also well fit by $\sqrt{T_S - T}$ (Fig.6.11). The η_S obtained by these two approaches agree within 5%, suggesting that the remnant minor domain has a minimal impact on the transport. This result stands in sharp contrast to earlier works using fixed-strain/stress detwinning in a clamp or horseshoe device[39], [87], [93], [100]–[103], which generally found a large resistivity anisotropy above T_S from the strain-induced $2m_{66}$ that mixes with the detwinned domain η_S below T_S, preventing a determination of the real mean-field development of η_S. Thus, our elasto-XRD technique allows for a precise measurement of a new transport coefficient, the *spontaneous elastoresistivity*, defined as a resistivity anisotropy η_S and structural order parameter ε_S driven by the system itself in the zero-stress limit. In the next section we describe the physical interpretation of the spontaneous elastoresistivity and how it is related to $2m_{66}$ and C_{66} above the transition.

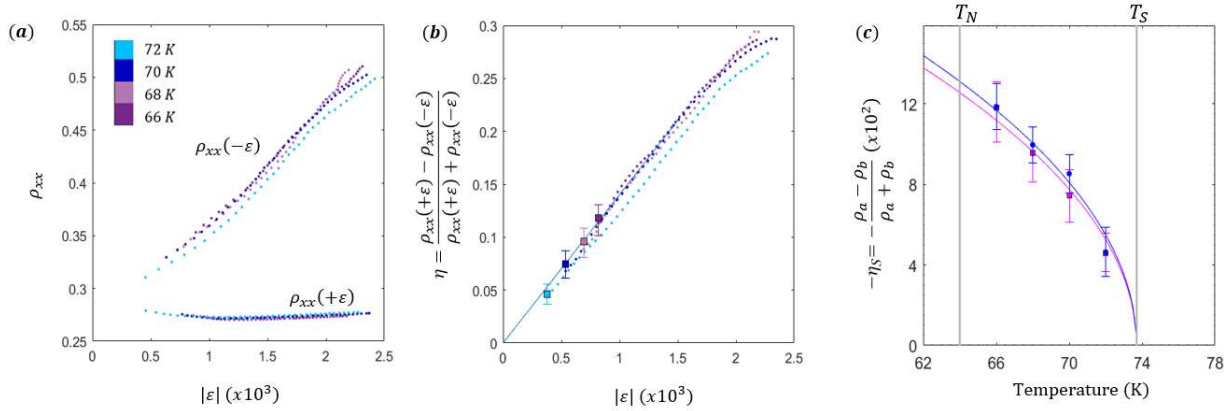

Figure 6.11 Nematic phase elastoresistivity. (a) The resistivity vs magnitude of orthorhombicity in the fully detwinned (>99%) regime. (b) The resistivity anisotropy $\eta = \frac{\rho_{xx}(\varepsilon) - \rho_{xx}(-\varepsilon)}{\rho_{xx}(\varepsilon) + \rho_{xx}(-\varepsilon)}$ calculated from the resistivities in (a). These values are used to linear extrapolate to ε_S to extract η_S (squares). The error bars here represent an uncertainty in the exact value of ε when defined from the difference of the a and b lattice constants taken from the $(2\ 2\ 12)_T$ and $(-1\ 1\ 14)_T$ reflections, where an instrumental uncertainty offset of $\varepsilon \pm .02\%$. Note that this offset does not affect the derivative $\frac{db}{da}$ used to extract the

Poisson's ratio. (c) The spontaneous resistivity anisotropy η_S extracted from detwinning (blue) and from fitting the high strain elastoresistivity (magenta) are both well fit to $\eta_S = A(73.8K - T)^{\frac{1}{2}}$.

6.6 Comparison of the nematic transport-structural coupling ratio across phase and temperature

The shared mean-field temperature dependence of η_S and ε_S below the transition echo the shared Curie-Weiss temperature dependence of the $2m_{66}$ and C_{66} above the transition, demonstrating the one-to-one correspondence between the transport and structural coefficients. The remaining question is whether this one-to-one correspondence is continuous across the phase transition. In Figure 6.12b we plot $\frac{\eta_S}{\varepsilon_S}$, the spontaneous elastoresistivity, and $2m_{66}\left(1-\frac{C_{66}}{C_{66,0}}\right)^{-1}$. These two quantities are the ratios between the dimensionless transport and structural coefficients below and above T_S, respectively. We find that both quantities show almost no temperature dependence and their temperature-averaged values are in strong agreement, with $\frac{\eta_S}{\varepsilon_S} = 142.6 \pm 20.7$ and $2m_{66}\left(1-\frac{C_{66}}{C_{66,0}}\right)^{-1} = 142.9 \pm 29.7$. This agreement suggests that for the entire temperature range of this study, the resistivity anisotropy behaves like a thermodynamic order parameter for all practical purposes. We note that this relationship is valid even at the lowest measured temperature within the pure nematic phase, 66 K, where the orthorhombicity reaches ~40% of its saturation value at base temperature, well beyond the infinitesimal limit.

We now show that $\frac{\eta_S}{\varepsilon_S}$ and $2m_{66}\left(1-\frac{C_{66}}{C_{66,0}}\right)^{-1}$ can be taken as the relative coupling of nematicity to the conducting electrons compared to the lattice. We again consider the Landau free energy discussed in detail in Chapter 3 that describes a nematic phase transition with a bilinear coupling to the lattice:

$$F = \frac{a_0(T-T^*)}{2}\psi^2 + \frac{b}{4}\psi^4 + \frac{C_{66,0}}{2}\varepsilon^2 - \lambda\psi\varepsilon\,.$$

Minimizing the free energy below the phase transition, we obtain the primary nematic order parameter $\psi_S \propto \sqrt{T_S - T}$ which induces a secondary order parameter, the spontaneous orthorhombicity $\varepsilon_S = \frac{\lambda}{C_{66,0}}\psi_S$. Combined with the linear nemato-transport relation $\eta_S = k\psi_S$, we get $\frac{\eta_S}{\varepsilon_S} = \frac{k\,C_{66,0}}{\lambda}$. Minimizing the free energy above the phase transition yields a Curie-Weiss nematic susceptibility $\frac{d\psi}{d\varepsilon} = \frac{\lambda}{a_0(T-T^*)}$ which results in $2m_{66} = k\frac{\lambda}{a_0(T-T^*)}$ and $\frac{C_{66}}{C_{66,0}} = 1 - \frac{\lambda}{C_{66,0}}\frac{\lambda}{a_0(T-T^*)}$. From this we find $2m_{66}\left(1-\frac{C_{66}}{C_{66,0}}\right)^{-1} = \frac{k\,C_{66,0}}{\lambda}$, identical to $\frac{\eta_S}{\varepsilon_S}$ below the transition (Fig.6.12a). If we ignore $C_{66,0}$, which is a material specific parameter not related to nematicity, we have a simple physical interpretation of $\frac{\eta_S}{\varepsilon_S}$ and

$2m_{66}\left(1-\frac{C_{66}}{C_{66,0}}\right)^{-1}$ – they measure the ratio of the nemato-transport coupling constant k and nemato-elastic coupling constant λ.

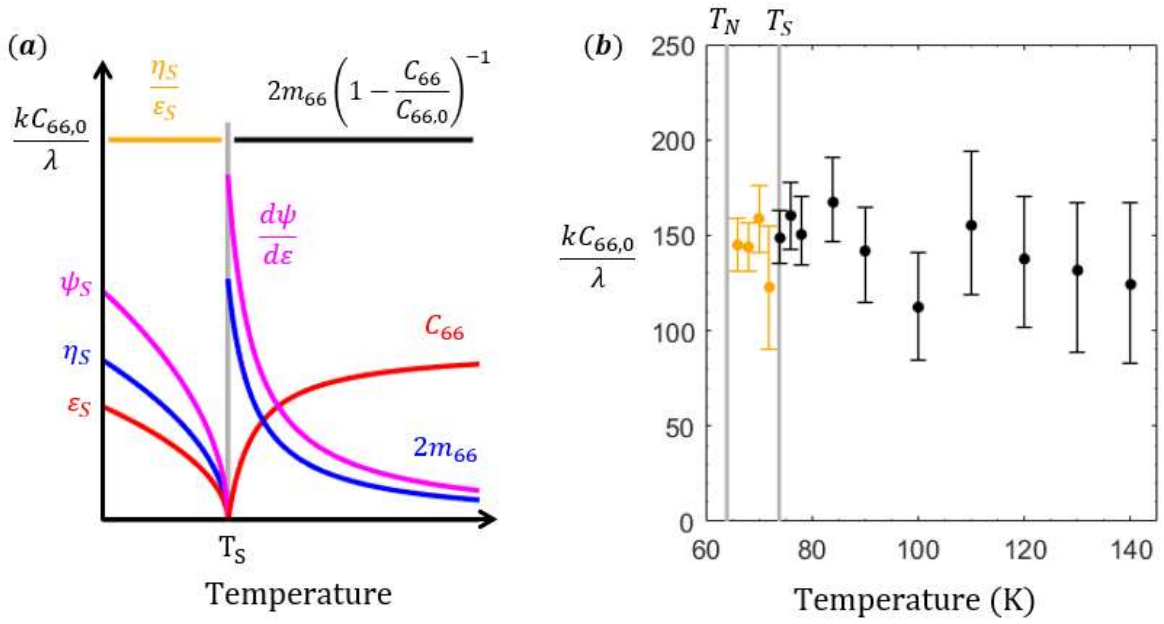

Figure 6.12 Transport-structural ratio equivalence. (a) For $T < T_S$, the spontaneous nematic order parameter $\psi_S \propto \sqrt{T_S - T}$ drives the linear proportional spontaneous orthorhombicity $\varepsilon_S = \frac{\lambda}{C_{66,0}}\psi_S$ and spontaneous resistivity anisotropy $\eta_S = k\,\psi_S$, yielding a temperature independent ratio $\frac{\eta_S}{\varepsilon_S}$. For $T > T_S$ the diverging nematic susceptibility $\frac{d\psi}{d\epsilon} = \frac{\lambda}{a_0(T^*-T)}$ drives the diverging elastoresistivity $2m_{66} = k\frac{d\psi}{d\epsilon}$ and the softened shear modulus $C_{66} = C_{66,0} - \lambda\frac{d\psi}{d\epsilon}$. The ratio $2m_{66}\left(1-\frac{C_{66}}{C_{66,0}}\right)^{-1}$ is thus also temperature independent. If the nematic-elastic (λ) and nematic-transport (k) proportionality coefficients are constant across the phase transition, both ratios equate at T_S with a value $\frac{kC_{66,0}}{\lambda}$. (b) The measured ratios $\frac{\eta_S}{\varepsilon_S}$ (gold) and $2m_{66}\left(1-\frac{C_{66}}{C_{66,0}}\right)^{-1}$ (black) vs temperature.

6.7 Comparison of transport-structural coupling ratio across doping.

Extensive measurements of $2m_{66}$ and C_{66} have been made across the phase diagram of $Ba(Fe_{1-x}Co_x)_2As_2$. In Figure 6.13 we plot the fitted Curie constant $(k\frac{\lambda}{a_0})$ for the $2m_{66}$ data from

ref.[55] and ($\frac{\lambda}{C_{66,0}}\frac{\lambda}{a_0}$) for the C_{66} data from ref.[54], which demonstrates that while ($k\frac{\lambda}{a_0}$) is enhanced towards the optimal doping, ($\frac{\lambda}{C_{66,0}}\frac{\lambda}{a_0}$) is not similarly enhanced. This observation suggests that the enhancement of $2m_{66}$ with doping is due not only to an enhancement of nematic fluctuations themselves but also due to a relative enhancement of nematic coupling to conduction electrons over the lattice. Indeed, we find that $2m_{66}\left(1-\frac{C_{66}}{C_{66,0}}\right)^{-1}$, or $\frac{k\,C_{66,0}}{\lambda}$, increases by more than a factor of 5 towards the optimal doping. Given that $C_{66,0}$ only shows weak doping dependence[68], the increase of $\frac{k\,C_{66,0}}{\lambda}$ can only come from the relative increase of k over λ, a condition which favors the superconducting pairing by nematic fluctuations[104]. A similar conclusion was made in a recent work comparing the doping evolution of the elastocaloric effect and elastoresistivity in this same system[56], which found evidence for a diminishing value of λ with doping towards optimal.

The efficacy of resistivity anisotropy as a representation of a thermodynamic order parameter and its breakdown in the large stress limit has a profound implication to the microscopic mechanism of nematicity. In the framework of Boltzmann transport theory, resistivity anisotropy is determined by the anisotropy of elastic and inelastic scattering rates and Fermi surfaces. Several theoretical studies argued that anisotropic spin fluctuations, the leading candidate of the microscopic mechanism of nematicity in iron pnictides, generate anisotropy in both elastic and inelastic scattering[88], [89], [105]. This picture provides a natural explanation for the non-saturating resistivity anisotropy in the large stress limit. The large stress shifts the antiferromagnetic transition to a higher temperature, which increases the spin fluctuations[40] and hence induces additional resistivity anisotropy. This is a non-linear effect that arises from the intertwined nature of vestigial nematicity[48], which is not captured in the Landau free energy discussed above. We note that this highly non-linear nemato-elastic coupling has also been observed in a recent elasto-scanning tunneling microscopy measurement.[106]

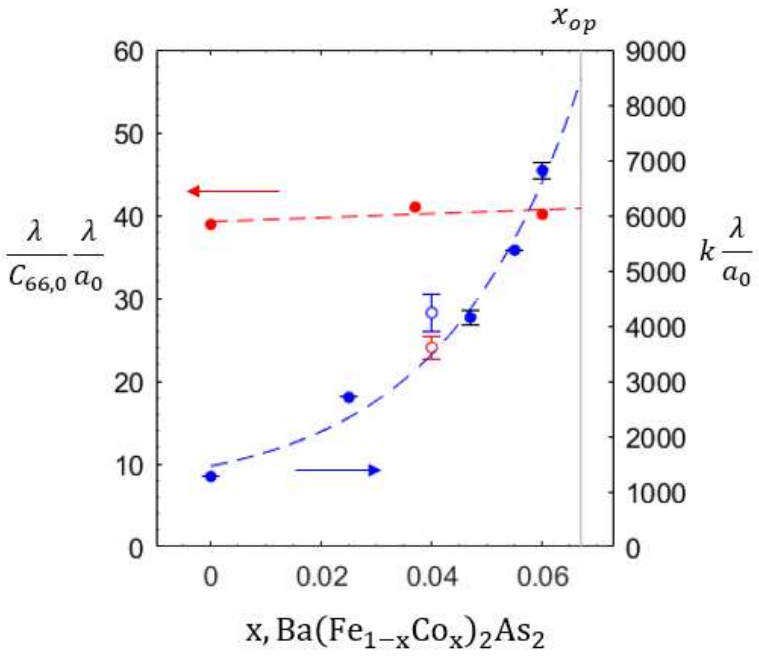

Figure 6.13 The Curie constants from Curie-Weiss fits to $2m_{66}$ (blue) and C_{66} (red) across the underdoped side of the phase diagram. Data from refs. [55], [68] (see main text). Dashed lines are a guide to the eye, solid vertical line at optimal Co doping $x_{op} = 0.067 \pm .02$. Open symbols from this work.

6.8 Conclusion

From the experimental perspective, the use of x-ray diffraction gives unprecedented detail in the detwinning process itself and reveals a highly non-linear structural and electronic responses close to the phase transition. While similar uniaxial stress approaches have been used recently to explore interesting properties in iron pnictides and beyond [8], [40], [84], [107]–[112], this work highlights the importance of in-situ microscopic measurement of structurally-complex quantum materials.

This project lays out several new methodologies that will be useful in future projects. First, we demonstrated a new method to extract the shear modulus from x-ray measurements of two lattice constants while applying strain. Second, we extracted the zero-stress elastoresistivity directly from the measured orthorhombicity and resistivity, obviating the need for a strain gauge. Importantly, as this method involved uniaxial stress and not biaxial strain, we do not add appreciable A_{1g} symmetric strain to the system as can occur from gluing sample directly to a piezo stack. Third, we stress tuned a single crystal sample to a nearly-fully detwinned state to extract the spontaneous resistivity anisotropy. This is the most precise measurement of the resistivity anisotropy that has yet been made. Fourth, this methodology allows for multiple quantities to be measured across phase transitions, allowing multimodal characterization of a single sample in both the infinitesimal and large order parameter limits.

Chapter 7:

Strongly Anisotropic Antiferromagnetic Coupling in $EuFe_2As_2$

7.1 Abstract:

In this chapter I present the first measurement of the metamagnetic spin flip transition in $EuFe_2As_2$ using a combination of applied uniaxial stress and the XMCD x-ray technique. From the form of this spin flip transition and from measuring three critical fields, I determine that the spin Hamiltonian describing this magnetic system must include both a non-Heisenberg biquadratic Eu-Fe coupling term and a strongly anisotropic Eu-Eu antiferromagnetic coupling term. The latter was such a surprising find that it became the title of my paper, "Strongly anisotropic antiferromagnetic coupling in $EuFe_2As_2$ revealed by stress detwinning" [9]. We posit that the Eu-Eu interaction has strongly anisotropic character due to the anisotropy of the nematic conduction electrons of the SDW-ordered Fe-layer that mediate the interaction, which is a new aspect of nematicity that has not yet been widely discussed.

7.2 Introduction: Magnetostructural coupling in $EuFe_2As_2$

Magnetism is the origin of a wide range of intriguing phenomena in iron-based superconductors, including electronic nematicity and high temperature superconductivity [32], [34], [62], [99], [113]. In contrast to the magnetism of the high-T_c cuprates, the stripe spin density wave (SDW) ground state breaks fourfold rotational symmetry and the spin dynamics are highly anisotropic [35], [112], [114], [115]. Key to this highly anisotropic magnetism is a sizable biquadratic coupling that is not captured in a simple Heisenberg model and likely arises from the dual itinerant-localized character of the Fe magnetism[36], [116]. It has also been suggested that this biquadratic term is necessary for the emergence of spin nematicity [37], [117].

Very recently, it was shown that a similar biquadratic coupling plays a role in the unusually large magnetoelastic coupling in $EuFe_2As_2$, where the introduction of a magnetic lanthanide element adds another layer of complexity into the magnetism of iron-based superconductors[118]. In addition to the SDW order, $EuFe_2As_2$ also hosts an A-type layered antiferromagnetic (AFM) order in the Eu layer, sharing the same easy axis with the Fe-SDW. Like in other iron pnictides, the SDW in $EuFe_2As_2$ creates orthorhombic twin domains. In $BaFe_2As_2$, due to the strong coupling between the structural distortion and the SDW, an applied field of order 25 T is able to fully detwin the structural domains [119]. Surprisingly, $EuFe_2As_2$ can be fully detwinned with less than 1 T, and partial detwinning can persist even after the field is turned off [120], [121]. Magnetization, NMR and neutron diffraction data show that this structural detwinning coincides with the reorientation of Eu moments towards the applied field direction, suggesting that the Eu magnetism and the associated large magnetic moments are responsible for this drastic reduction of detwinning field [120], [122], [123]. Nevertheless, as no single-ion anisotropy is present for the half-filled Eu $4f^7$ electrons and no dipolar coupling between the Fe and Eu layers is allowed by symmetry, it remained an open question how Eu moments even sense the

orthorhombic direction. Recently, Maiwald et al solved this mystery by considering a biquadratic coupling between Fe-SDW and Eu-AFM moments[118]. The biquadratic coupling of the form $K(f_i \cdot e_j)^2$, where f_i and e_j represent the Fe and Eu moments, respectively, provides an effective single-ion anisotropy that couples the Eu moment orientation with the Fe-SDW direction[118]. Therefore, while the Fe-Fe biquadratic coupling generates the nematicity in the FeAs layer, the Eu-Fe biquadratic coupling provides a pathway for the Eu magnetism to couple to the structural orthorhombicity and the underlying nematicity.

This chapter discusses the discovery of another consequence of the higher order Eu-Fe coupling in $EuFe_2As_2$ – a highly anisotropic Eu-Eu interplanar coupling. The degree of anisotropy of Eu-Eu interlayer exchange ($\frac{J_x - J_y}{J_x + J_y}$) is about 75 times larger than the structural orthorhombicity, which can only be understood by considering the influence of the Fe-SDW order. The anisotropy of Eu-Eu interlayer exchange was overlooked previously because the field detwinning process masked the spin-flip nature of Eu metamagnetic transition. We overcome this challenge by a direct measurement of the Eu metamagnetic transition in a mechanically detwinned sample using a piezoelectric stress device, which allows us to apply magnetic fields either parallel or perpendicular to the easy axis of Eu moments within a single structural domain. Conventional magnetometry techniques are difficult to apply to a sample mounted to a strain device due to the added size and background magnetization contributed by the device. We therefore employ x-ray magnetic circular dichroism (XMCD) on the Eu L_3 edge to measure the Eu-specific in-plane magnetization induced by an applied magnetic field. We show that we are able to strain the crystal into a monodomain which exhibits either a large jump in magnetization, consistent with a spin flip transition, or has a perfectly linear magnetization from continuous canting of Eu moments (i.e., we are able to turn the metamagnetic transition on and off). From the measurement of the critical field for the Eu spin flip and the field dependence of the spin canting, we determine the energies of the Eu-Eu and Eu-Fe coupling and discover that the Eu-Eu interaction itself is directionally dependent on the orientation of Fe moments. We then confirm this by first principles calculations. The discovery of the anisotropic Eu-Eu interplanar coupling also sheds light on the evolution of the Eu magnetism in doped $EuFe_2As_2$ which we reevaluate in section 7.12.

7.3 Sample preparation

The sample mounted to the strain device was prepared identically to the sample in Chapter 6. Single crystal samples of $\mathrm{EuFe_2As_2}$ were grown from a tin flux as described elsewhere [124]. The sample was cleaved from a large as-grown single crystal plate and cut along the tetragonal [1 1 0] direction into a bar with dimensions 3.2 x 0.50 x 0.065 mm. These sample dimensions correspond to a demagnetization factor of N=0.13 along the applied field direction [125], resulting in a small maximum demagnetization field of only $\mathrm{NM_{Eu}}{\sim}0.005\mathrm{T}$. A piezo-actuator uniaxial stress device (*Razorbill Instruments, CS*-100) was used to provide in-situ stress along the length of the bar which was affixed with Stycast epoxy. The four-wire electrical contact geometry is illustrated in Figure 7.1, with wires underneath the sample to not obstruct the x-ray fluorescence off the top surface of the crystal.

Measurements of the resistivity coefficient ρ_{xx} aligned along the stress axis were performed using a standard 4-point measurement and an SR830 lock-in amplifier.

Figure 7.1a shows the fully magnetically ordered unit cell at T=7K and zero applied magnetic field. Eu moments are aligned ferromagnetically within each plane and antiferromagnetically between planes. The Fe spin density wave ordering results in a small structural orthorhombicity and the formation of structural twin domains that are identical up to a 90-degree rotation. Within each domain, the Eu AFM and Fe SDW easy axes are aligned with the longer orthorhombic a lattice constant [81], [126]. We use a geometry with the $\hat{x}$ and $\hat{y}$ axes aligned to the orthorhombic a and b directions, and tensile or compressive stress applied along the $\hat{x}$ direction detwins the sample toward the A monodomain (a lattice vector along $\hat{x}$) or B monodomain (b lattice vector along $\hat{x}$), respectively (Fig.7.1b). Once in the A (B) monodomain state, the measured resistivity ρ_{xx} becomes sensitive to the anisotropic resistivity ρ_a (ρ_b) along the orthorhombic a (b) direction. Magnetic field is applied perpendicular to the current/strain axis and at 10 degrees above the ab plane. Except for a change in the strain state, the sample is not reoriented in any way during the experiment, ensuring identical effective fields and XMCD-illuminated sample volumes. XMCD measures the induced Eu magnetic moment along the field direction, which is fixed parallel to the incident x-ray direction in this study.

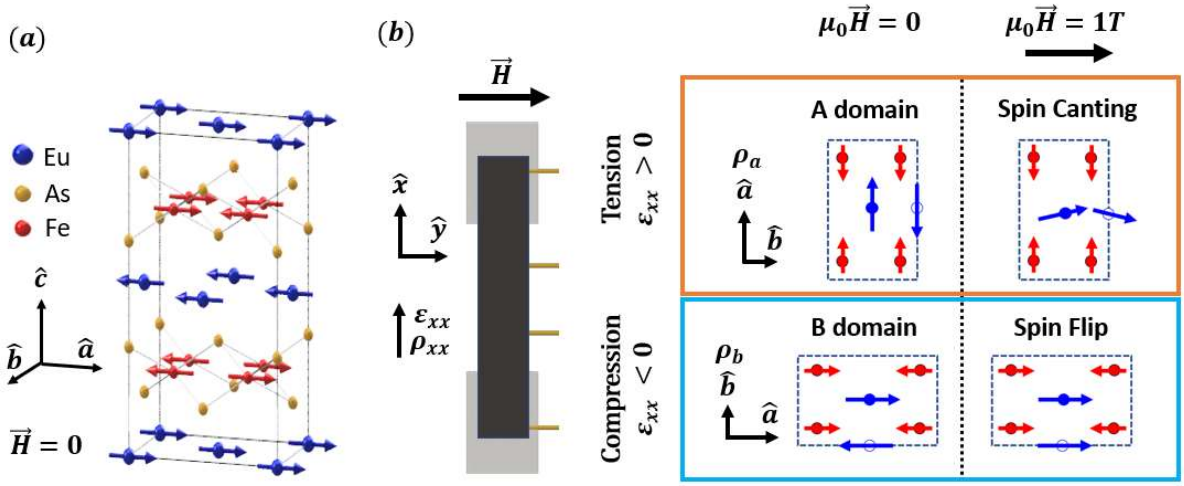

Figure 7.1 (a) $EuFe_2As_2$ unit cell at T=7K and zero applied magnetic field. Both Fe and Eu antiferromagnetic orders are stabilized with easy axes aligned with the longer a lattice constant of the orthorhombic unit cell. (b) Uniaxial stress is applied along the $\hat{x}$ direction aligned with the orthorhombic a/b orthorhombic unit cell lattice directions such that tension (compression) detwins the sample to the A (B) domain (orange/blue outline). Resistivity measurements along the stress axis measure ρ_a (ρ_b) aligned with the a (b) lattice constant of the A (B) domain. A magnetic field is applied perpendicular to the strain axis at $10°$ above parallel from the a/b plane, causing a reorientation of Eu moments to align along the field direction. XMCD is proportional to the Eu magnetization along the applied field direction. For simplicity, we collapse the 4 Eu atoms and 8 Fe atoms of the doubled orthogonal unit cell into 2 Eu (blue arrows) and 4 Fe (red arrows) effective moments.

7.4 Strain detwinning

At T=7K, the $EuFe_2As_2$ B_{2g} orthorhombicity $\left(\varepsilon = \frac{a-b}{a+b}\right)$ is approximately 0.28%, while the maximum nominal strain (ε_{xx}^{nom}) applied to the sample is 0.3%. Naively we would expect to fully detwin the sample. However, as discussed in ref. [5], pinned remnant domains persist up to large applied strains, inhibiting a total detwinning. We can estimate the A domain population vs applied strain using calibration data from refs. [5], [8], where the uniaxial strain detwinning was monitored with simultaneous x-ray diffraction. In Figure 7.2 we show simulated detwinning data for $EuFe_2As_2$, adjusting the detwinning for the difference in sample orthorhombicity. We find that at our maximum applied strain (grey bars) that the sample volume should contain about 5% of the minor domain (evidence for this remnant domain is visible in the small resistivity drop of the A domain at 7K in Figure 7.5a).

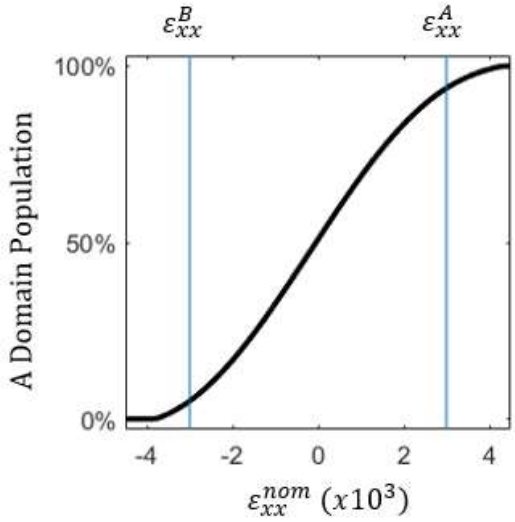

Figure 7.2 Simulated detwinning data for $EuFe_2As_2$ at T=7K based on x-ray diffraction detwinning data from ref. [5]. Grey bars indicate the strain applied to create the A and B monodomains of Figure 7.5.

7.5 X-ray Magnetic Circular Dichroism

Here I discuss important methodology details of the XMCD measurement; for a theoretical introduction to XMCD see Chapter 4.4. XMCD was measured at the Advanced Photon Source beamline 4-ID-D at Argonne National Laboratory. We probed the Eu L_3 edge using x-rays of 6.97 keV, which measure the spin polarization of the Eu 5d band due to the magnetic moment of the 4f orbital. Generally, the Eu L_3 edge XMCD signal can be taken as proportional to the 4f moment magnetization; however, as the Eu 5d band has a significant hybridization with the As 4p orbitals [127], which themselves hybridize with the Fe 3d orbitals, the exact value of the XMCD is expected to have some dependence on Fe conduction effects. Nonetheless, we can use the sharp changes in XMCD signal to mark the fields at which magnetic transitions and saturations occur at. A superconducting split coil

magnet with a large bore was used to apply magnetic field. The sample temperature was controlled using He flow. XMCD was collected in fluorescence geometry by monitoring the Eu L_α line using a four element Vortex detector integrated with the Xspress module to enable a larger dynamical range. Circularly polarized x-rays were generated using a 180 microns thick diamond (111) phase plate.

The XMCD spot size illuminates the whole sample width across the y direction and is roughly 100 microns wide along the x direction (between the transport wires) and probes a depth of about 5 microns. The beam is centered on the middle of the crystal where strain is most transmitted and homogenous. The transport wires are separated by about 1700 microns, and transport is sensitive to the whole bulk of the sample. While the resistivity and XMCD are not measuring exactly the same volume of crystal, the tight correlation between the two data sets suggests no major difference in crystal behavior between the two sampled volumes.

The XMCD measurement uses a circularly polarized incident x-ray beam and measures the helicity-dependent intensities $\mu_{R,0}$ and $\mu_{L,0}$ as a function of x-ray energy. To analyze these data, we first sum $\mu_{R,0}$ and $\mu_{L,0}$ and normalize by the jump in intensity at the L_3 edge. Then we correct the data for self-absorption to get μ_R and μ_L. In this case the XAS is the sum of the two intensities, $\mu_R + \mu_L$, and is found to peak at E=6.975 keV, i.e. at the peak of the Eu L_3 edge as expected. The difference in intensity $\mu_R - \mu_L$ is the XMCD and is peaked at E=6.973 keV. Hence, the XMCD is already normalized by the total intensity.

During the initial calibration it was found that the sample was not appreciably displaced by applied field up to 1T; this means the same sample volume was probed by the XMCD measurement over the whole field range. For this reason, it was unnecessary to do a full energy scan at every field point. Instead, a much quicker measurement was performed using x-rays of energy E=6.970 keV, just below the XMCD peak but with roughly half the peak intensity. At each field point the helicity-dependent intensity measurement was made. At the maximum field value of $\pm$1T a full energy scan was performed and used to normalize the E=6.970 keV data vs field by the peak XMCD value at 1T and E=6.973 keV.

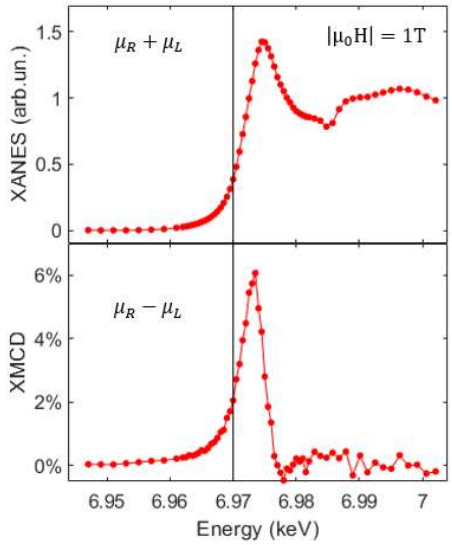

Figure 7.3 XANES and XMCD. Energy scan of incident x-rays of left and right helicity (normalized intensity μ_L and μ_R, respectively) at a fixed applied field of 1T and at T=7K for the B domain (i.e. saturated magnetic moment post spin flip). The sum of the normalized helicity intensities yields the XANES (arbitrary units) while the difference yields the XMCD. Line shows energy at which field-dependent intensity scans were made.

7.6 Paramagnetic Eu magnetization

First, we address the effect of the applied magnetic field at T=30K, below the orthorhombic and SDW transitions ($T_{SDW} = 187K$), but above the Eu AFM ordering temperature ($T_N = 19.1K$). In the Eu^{2+} valence state, the $4f^7$ electrons have zero orbital angular momentum ($L = 0$), and as such are expected to show an isotropic response to applied field. After detwinning to either the A or B monodomain, we applied fields from 0 to 1 T and measured the XMCD and resistivity simultaneously in 0.02 T steps (XMCD data were not collected for the B monodomain for 0.8 T-1 T at this temperature). We find an XMCD signal that is indistinguishable between the two domains, suggesting that at this temperature and field range the Eu-Fe interaction is negligible compared to the Eu paramagnetic coupling to applied field (Fig.7.4). We note that compared to the data presented next, the XMCD values at 1 T and 30 K are roughly 3 times smaller than the 1 T XMCD saturation value within the Eu AFM phase, consistent with a lower susceptibility in the paramagnetic phase. As in $BaFe_2As_2$, the zero-field resistivity is considerably larger along the orthorhombic b direction than the a direction. Both ρ_a and ρ_b have a weak field dependence at 30K. The inset to Figure 7.4 shows the detwinned sample cooling through the Eu AFM transition. As demonstrated previously in mechanically detwinned $EuFe_2As_2$, we see no change in the Eu transition temperature between the tensile and compressive cooling data, nor do we see any additional resistivity anisotropy induced by the Eu AFM ordering [128]. Indeed, the resistivity anisotropy $\frac{\rho_b - \rho_a}{\rho_b + \rho_a} = 0.084(2)$ is unchanged through this temperature range.

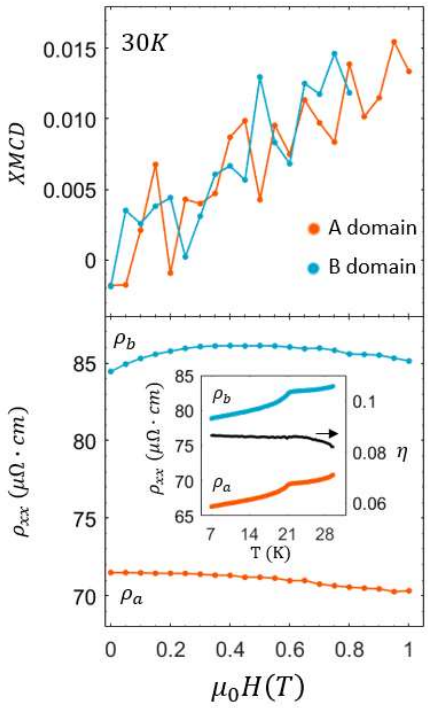

Figure 7.4 $T = 30K$ single pass applied magnetic field sweep for the detwinned A and B domains (XMCD data was not collected for B domain 0.8T-1T). XMCD above the Eu AFM ordering temperature shows a nearly isotropic response to field. ρ_{xx} vs applied magnetic field reveals a minimal magnetoresistance. (Inset, left) ρ_{xx} vs temperature for the detwinned A and B monodomains reveal no additional anisotropy induced at the Eu AFM ordering temperature $T_{N,Eu} = 19.1K$. (Inset, right) The resistivity anisotropy $\eta = \frac{\rho_b - \rho_a}{\rho_b + \rho_a}$ (black).

7.7 Antiferromagnetic Eu magnetization

We now discuss results from within the Eu AFM phase at 7K. We applied field through a ±1 T loop to each detwinned state and measured the XMCD and resistivity simultaneously in 0.02 T steps (Fig.7.5). In the A domain (Fig.7.5a), the Eu moments are initially aligned with the AFM easy axis transverse to the field direction. The linear growth of XMCD signal with field indicates that Eu moments cant continuously to align with the field, with no observable hysteresis. Conversely, in the B domain (Fig.7.5b) the easy axis is along the field direction, and so for fields below 0.4 T the XMCD is nearly flat as no canting can occur. The jump in XMCD from 0.4 T to 0.6 T and accompanying hysteresis is a clear sign of a metamagnetic spin flip transition between the Eu AFM and FM states. The weak linear field dependence of magnetization in the pre- and post-spin-flip field ranges are due to the out of plane magnetization induced by the small out of plane field component, which is assumed to equally contribute to the A domain magnetization. We note that the observation of spin flip transition contradicts the expectation from the spin Hamiltonian derived from ref.[118], which predicts a spin flop

transition. As will be shown in section 7.10, this contradiction can only be resolved by including an anisotropic interlayer exchange between Eu moments.

The resistivity is approximately linear in field for $|\mu_0 H| < 0.4T$ and $|\mu_0 H| > 0.6T$ for both domains. For $0.4T < |\mu_0 H| < 0.6T$, a large hysteretic drop occurs in the B domain resistivity, coinciding with the jump in XMCD. A much smaller drop also occurs in the A domain, which also shows a small hysteresis (Fig.7.5a, inset), and is likely due to a remnant B domain that was not fully detwinned and which is not resolved in the XMCD measurement. For each domain, the resistivity returns to the initial zero-field value after the field loop, indicating that there is no persistent field-detwinning in our setup as is found reliably from previous studies of freestanding samples [120], [121]. Further, given the field and current orientation, the sample in either strain state would be expected to detwin towards the higher-resistivity B domain above ~0.5T, and so the drop in resistivity for both domains suggests that our stress device is indeed preventing field detwinning. This is also strong evidence for a purely Eu spin origin of the resistivity jump.

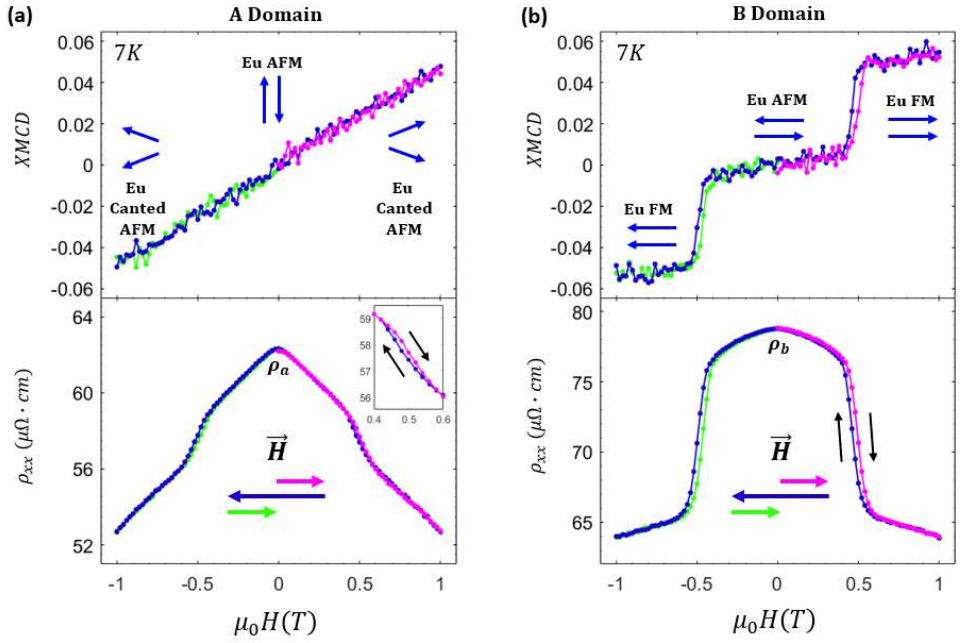

Figure 7.5 Field sweep at T=7K in the fully magnetically ordered phase presented in Fig.7.1a. Applied field ramped from 0T to 1T, -1T and 0T in each detwinned A (a) and B (b) monodomain states. Inset to bottom panel of (a) shows the small magnetoresistance hysteresis visible near 0.5T in the A domain.

Both the XMCD and resistivity data show excellent agreement between positive and negative field values. In Figure 7.6a, we plot the average value over positive and negative field sweeps of the XMCD and the magnetoresistance. While we were unable to apply enough field to fully saturate the A domain XMCD, we can extrapolate the field dependencies of each domain to estimate the saturation field. Linear fits to the XMCD of the A and B domains at fields greater than 0.6 T are shown, with an intersection at $\mu_0 H_A^{sat}$ = 1.17 T. Beyond this field, the Eu magnetic moment is expected to be fully saturated in each domain, as seen in freestanding crystal magnetometry studies [118], [121], [122],

[129]. To more precisely determine the B domain spin flip field H_B^{flip} we use the value at the center of the field hysteresis. Figure 7.6b shows the difference between the increasing and decreasing field values of the XMCD and resistivity. In the B domain, a sharp peak in both quantities occurs at $\mu_0 H_B^{flip} = 0.48T$. We will use these critical field values to develop an appropriate spin Hamiltonian to describe these magnetization data, but first in the next section we will confirm that the data really does correspond to a fixed-domain state by comparing to a 50/50 A/B twin domain state as well as to a freestanding twinned crystal.

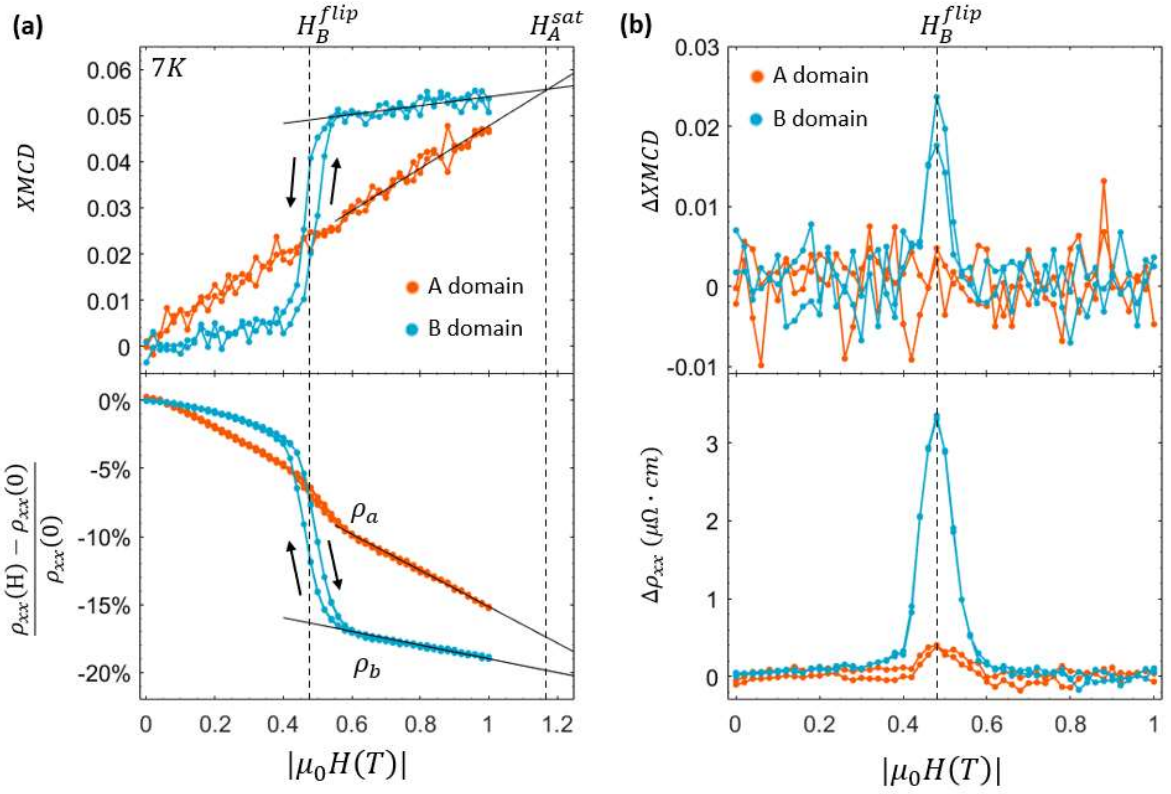

Figure 7.6 (a) Data from Fig.7.5a-b replotted as the average value of positive and negative field sweeps of XMCD and the magnetoresistance against the absolute value of applied magnetic field for the detwinned A (orange) and B (blue) monodomains. Linear fits (black lines) to the XMCD magnitude for $|\mu_0 H| = 0.6T$ to $1T$ indicate both values coincide at $|\mu_0 H_A^{sat}| \sim 1.17T$. The magnetoresistance for positive and negative field are nearly identical and tightly overlap. (b) The difference in XMCD and ρ_{xx} for increasing and decreasing fields yields $\Delta XMCD = XMCD(H_{inc}) - XMCD(H_{dec})$ and $\Delta\rho_{xx} = \rho_{xx}(H_{inc}) - \rho_{xx}(H_{dec})$. For the B domain the peak values of $\Delta XMCD$ and $\Delta\rho_{xx}$ coincide at $\mu_0 H_B^{flip} = 0.48T$.

7.8 Fixed-length twinned sample prevented from field detwinning

In principle, the lattice distortions induced by the detwinning strain could cause a change in the interaction strengths between Eu and Fe planes that could alter these critical fields. Here we show that H_A^{sat} and H_B^{flip} are essentially unchanged by considering also a nearly zero-strain state, demonstrating that the strain applied to detwin the sample does not appreciably affect the interplanar coupling strengths. In Figure 7.7 we present data for the same sample tuned to a nearly-zero strain state in which both A and B domains are present in approximately equal proportions at 7K, and then run through the same field loop as the data measured in the fully detwinned states presented in Figure 7.5 (XMCD data was not collected for the first 0 to 0.6T range of the field sweep). Figure 7.7a shows the XMCD and resistivity of the twin domain state (green) compared to the detwinned A and B domain data from Figure 7.5. The resistivity returns to its zero-field value after the field loop, suggesting that no persistent field detwinning occurs. In Figure 7.5b we plot the absolute value of the XMCD and the magnetoresistance of the twin domain state against a linear combination of 51% A domain and 49% B domain data from Figure 7.6a. We find the linear combination is an extremely good match to the measured data, with $R^2 > 0.97$ and $R^2 > 0.99$ for the XMCD and magnetoresistance, respectively (Fig.7.7b, black). This indicates the twinned state is indeed in a nearly equal domain population state at zero field, which is maintained over the applied field range, and each domain responds nearly identically to field as in the fully detwinned state. Further, this shows that the detwinning strains applied in this work do not meaningfully alter the critical fields H_A^{sat} and H_B^{flip}.

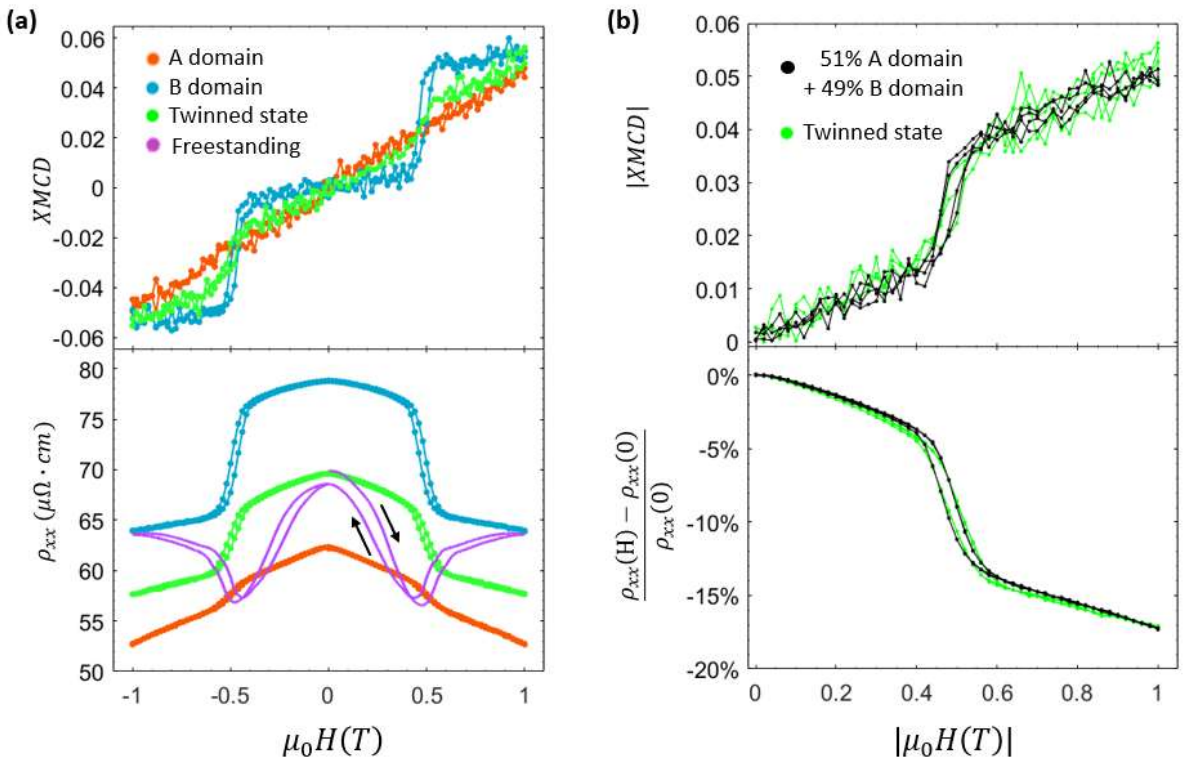

Figure 7.7 (a) Data from Fig.7.5a-b for A (orange) and B (blue) detwinned monodomains, as well as a nearly-zero strain twin domain state (green) run through the same field loop. Resistivity from a second freestanding sample (violet) shows a substantially different field response to the fixed length sample due to hysteretic domain detwinning. (b) Twin domain data (green) with a linear superposition of 51% A domain and 49% B domain data superimposed (black) (absolute value of XMCD across field sweeps).

The behavior of the twinned sample held in the strain cell is in sharp contrast with the freestanding sample (i.e. one not encased in epoxy or mounted to a strain device). We measured the magnetoresistance of a freestanding sample in a Quantum Design PPMS at 7K with field applied perpendicular to current and in-plane at 10 degrees above grazing incidence, identical to the conditions of the strained sample. For a freestanding crystal in an initial zero-field equal A/B domain population state, an applied field in this geometry would first detwin the sample towards the lower resistivity A domain followed by a rapid detwinning to the higher resistivity B domain [118], [120], [121]. This manifests in our freestanding sample as an initial decrease of the resistivity at low field followed by a sudden jump at $\mu_0 H = 0.44T$, with a large hysteresis across the loop and a lower resistivity value on return to zero field indicating the persistent domain detwinning (Fig.7.7a, violet). This clear difference in behavior from the fixed strain sample further corroborates that fixed strain prevents field detwinning and so the resulting magnetoresistance can be interpreted as purely the consequence of Eu moment reorientation [121], [122], [130].

7.9 Spin Hamiltonian derivation

In anticipation of the coming discussion, we define a spin Hamiltonian with an anisotropic Eu-Eu interaction and calculate the critical fields and other quantities. We refer the reader to ref. [118] for a detailed discussion of the spin Hamiltonian in this system. My contribution to the development of this spin Hamiltonian was to incorporate an Eu-Eu anisotropic exchange term W and determine its consequences on the critical fields and saturation fields. We start by considering the doubled unit cell of the fully ordered state ($Eu_2Fe_4As_4$), and a fixed Fe moment orientation aligned along $\hat{x}$ (Fig.7.8). From the symmetry of the magnetic ordering structure (Fig. 7.1a), the dipolar interactions of Eu and Fe moments cancel each other and so do not contribute to the magnetic energy. The half-filled $4f^7$ orbital of Eu^{2+} has zero orbital angular momentum ($L = 0$) and negligible single ion anisotropy, but the posited biquadratic coupling between Eu and Fe moments creates an effective magnetocrystalline anisotropy. We define a biquadratic coupling energy K between the 8 inequivalent Eu-Fe moment pairs, with a total Eu-Fe planar coupling energy $8K$. We define the anisotropic coupling energy between the Eu AFM sublattices to be directionally dependent, with $J_x = J + W$, $J_y = J - W$, and $W = W(e_{1,x}e_{2,x} - e_{1,y}e_{2,y})$, where $\overrightarrow{e_i} = (e_{ix}, e_{iy})$ is the unit vector of the ferromagnetic moment of the Eu atoms in the 2 AFM sublattices. Finally, the magnetic energy is given by

$$E = 2J_x e_{1x}e_{2x} + 2J_y e_{1y}e_{2y} + 8K\sum_i (\overrightarrow{e_i} \cdot \hat{y})^2 - M\sum_i \vec{H} \cdot \overrightarrow{e_i}$$

where $(\overrightarrow{e_i} \cdot \hat{y})^2$ is the biquadratic interaction between Eu and Fe moments (with interaction energy K for each of the 8 Fe nearest neighbors to each Eu moment), $\vec{H}$ is the applied field with isotropic coupling to the Eu moments (the moment size M of each Eu AFM sublattice is approximately 6.8 μ_B at T=7K), and the summations are over the two Eu planes. In the initial zero field case (Fig.7.8a) we have $\overrightarrow{e_1} = \hat{x}$, $\overrightarrow{e_2} = -\hat{x}$, and $E = -2J_x$.

We consider the evolution of the energy with a magnetic field applied along the 3 directions used in the main experiment by symmetrizing the Eu moments about the field direction. First defining $\overrightarrow{e_1} = \cos\theta\ \hat{x} + \sin\theta\ \hat{y}$ in all cases, we define $\overrightarrow{e_2} = -\cos\theta\ \hat{x} + \sin\theta\ \hat{y}$ for $\vec{H} = H\hat{y}$ (Fig.7.8b), $\overrightarrow{e_2} = \cos\theta\ \hat{x} - \sin\theta\ \hat{y}$ for $\vec{H} = H\hat{x}$ (Fig.7.8c), and $\overrightarrow{e_2} = \sin\theta\ \hat{x} + \cos\theta\ \hat{y}$ for $\vec{H} = H\left(\frac{1}{\sqrt{2}}\hat{x} + \frac{1}{\sqrt{2}}\hat{y}\right)$ (Fig.7.8d). By substituting these moment definitions into the spin Hamiltonian, minimizing the energy with respect to θ, and then solving for a fully saturated moment ($\theta = \frac{\pi}{2}$, 0, and $\frac{\pi}{4}$, respectively) we arrive at the saturation fields:

$$H_A^{sat} = \frac{4J + 16K}{M}$$

$$H_B^{flop,sat} = \frac{4J - 16K}{M}$$

$$H_{AB}^{sat} = \frac{4J}{M}$$

From the form of these saturation fields, it is clear that the anisotropy between J_x and J_y are averaged over, resulting in the isotropic J and no explicit term W. However, the term $H_B^{flop,sat}$ refers to the saturation field after a spin flop transition (which onsets at $H_B^{flop,onset} = \frac{8}{M}\sqrt{K(J-4K)}$ for $W = 0$), while a key finding of our measurement is that a sharp spin flip transition occurs instead. Treating this transition as an Ising spin flip, we have

$$H_B^{flip} = \frac{2J_x}{M} = \frac{2(J+W)}{M}$$

For a spin flip transition to occur, the energy at the transition must be lower than the fully-saturated spin flop phase, $E\left(H_B^{flip}\right) < E\left(H_B^{flop,sat}\right)$. Solving for each energy results in the condition

$$\frac{J}{8K+W} < 1$$

As discussed in the main text, from our measurements of H_A^{sat}, H_B^{flip} and $H_{45°}^{sat}$, our experimentally determined values of J, W, and K result in the spin flip condition being satisfied.

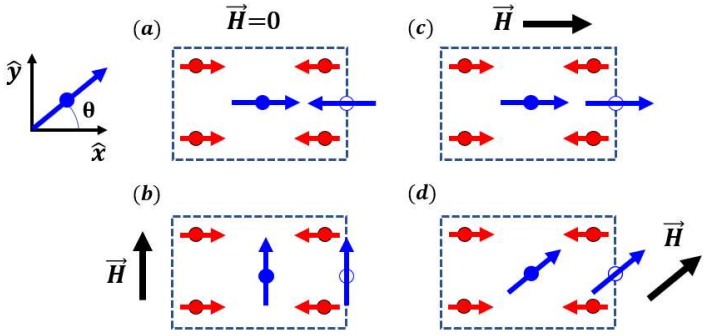

Figure 7.8 The 4 Eu-Eu moment arrangements relative to a fixed Fe moment arrangement, with (a) Eu AFM along $\hat{x}$, (b) Eu FM along $\hat{y}$, (c) Eu FM along $\hat{x}$, and (d) Eu FM along $\frac{1}{\sqrt{2}}(\hat{x}+\hat{y})$

7.10 Measured critical fields and the spin Hamiltonian

We now relate the spin flip and saturation fields H_B^{flip} and H_A^{sat} to the microscopic interactions in the sample using the spin Hamiltonian. We will start with the isotropic Eu-Eu case ($J_x = J_y = J, W = 0$) and show that to explain the experimental results an additional anisotropic exchange term is needed.

Using the results derived above and following the usual treatment of spin-flip and spin canting transitions we determine the critical fields as

$$H_B^{flip} = \frac{2J}{M}$$

$$H_A^{sat} = \frac{4J + 16K}{M} = 2\left(H_B^{flip} + \frac{8K}{M}\right)$$

For the B domain, Eu and Fe moments are aligned both before and after the spin flip, and so the presence of the biquadratic coupling does not change the value of the spin flip field, but only serves to provide the necessary magnetocrystalline anisotropy to enforce a sharp spin flip transition. For the A domain, the biquadratic coupling provides an extra energy barrier that must be overcome by the field to reach the fully saturated canted state. From the measured values $\mu_0 H_A^{sat} = 1.17\ \mathrm{T}$ and $\mu_0 H_B^{flip} = 0.48\ \mathrm{T}$, and using the expected Eu moment $M = 6.8\ \mu_B$ [120], [121], we obtain $J = 94.5\ \mu eV$ and $8K = 41.3\ \mu eV$. Thus, the Eu-Eu and Eu-Fe planar coupling energies are comparable, $\frac{J}{8K} = 2.3$.

At this point we are facing an apparent contradiction: we observe experimentally a sharp spin *flip* transition, but for $\frac{J}{8K} > 1$ the spin Hamiltonian would actually be expected to result in a spin *flop* transition, as shown in Fig.7.9. (See ref. [118] for further discussion). This discrepancy has important implications for correctly modelling the field detwinning process, which has been based on the (never actually observed) spin flop transition. This apparent contradiction indicates that an additional term is needed in the spin Hamiltonian. The simplest such term is a symmetric anisotropic exchange term $W(e_{i,x}e_{i+1,x} - e_{i,y}e_{i+1,y})$, where $e_{i,x}$ and $e_{i,y}$ are the x and y components of the Eu moment in the ith layer, using a notation with Fe moments aligned antiferromagnetically along $\hat{x}$. This term then increases (decreases) the interaction strength between Eu moments when aligned parallel (perpendicular) to the Fe moments, and provides the additional anisotropy needed to enforce a spin flip transition. Although other higher order terms could also be introduced to the spin Hamiltonian, they generally lead to non-linear *M-H* curves which were not observed in the experiment. With this additional term, the criterion for a spin flip transition becomes $\frac{J}{8K+W} < 1$, and the critical fields are:

$$H_B^{flip} = \frac{2(J + W)}{M}$$

$$H_A^{sat} = \frac{4J + 16K}{M} = 2\left(H_B^{flip} + \frac{8K - 2W}{M}\right).$$

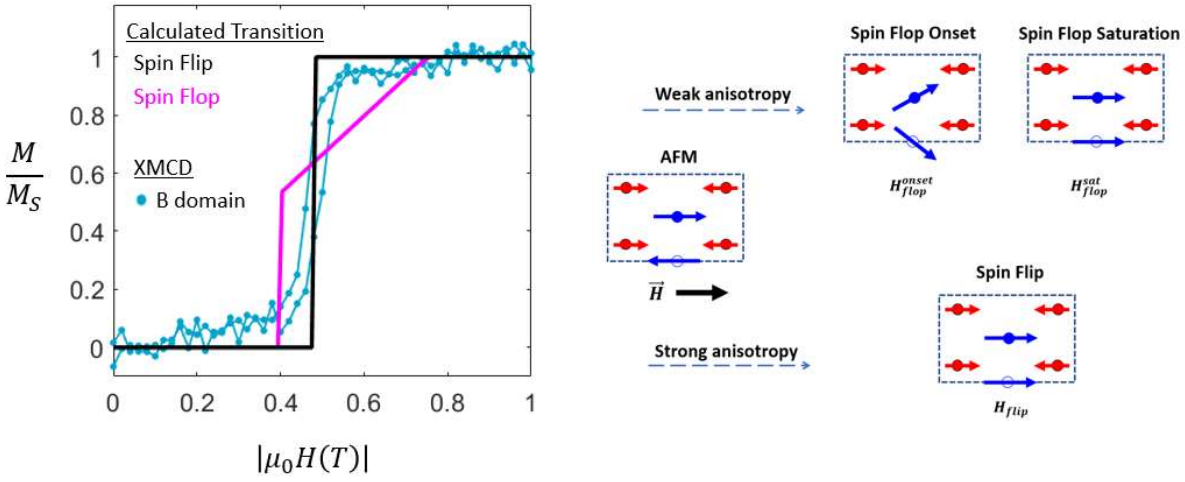

Figure 7.9 The XMCD data of Fig.7.5a for the B domain normalized to the 1T mean value. Black (magenta) line represents the T=0K metamagnetic spin flip (spin flop) transition calculated using the anisotropic JKW (isotropic JK) model (see main text).

7.11 VSM magnetization measurement to yield 3 critical fields

The three parameters J, K and W cannot be uniquely determined by the two experimentally measured values. Therefore, additional constraint is needed. This constraint can be provided by the measurement of $H_{45°}^{sat}$, i.e. the field required to saturate the magnetization when the field is aligned 45 degrees to the easy and hard axis, such that the field has an equivalent effect on both domains. It has the following expression:

$$H_{45°}^{sat} = \frac{4J}{M}.$$

As our strain+XMCD measurements have demonstrated the need for the W term, we now discuss the extraction of J, K and W from a second sample from the same growth batch via magnetization measurements using a vibrating sample magnetometer (VSM) in a Quantum Design PPMS. The sample was cut into a thin octagon with surface area 2.18 mm^2 and thickness 0.0165 mm. The thin octagonal shape of the sample also ensures that field applied totally in-plane along the $[1\,0\,0]_T$ and $[1\,1\,0]_T$ directions have an identical (negligible) demagnetization factor [125]. The sample was encased in GE varnish so that the domain configuration is fixed to 50/50 and the field detwinning is prohibited. As shown in Figure 7.9b, at T=2K for field applied along the $[1\,0\,0]_T$ direction (blue curve), i.e. at 45° to both domain easy axes, the magnetization exhibits continuous spin canting toward saturation at $\mu_0 H_{45°}^{sat} = 0.73$ T. For field applied along the $[1\,1\,0]_T$ direction (red curve) the *M* vs *H* perfectly overlaps with the combination of the responses of A and B domains from the XMCD measurements (grey), confirming the absence of field detwinning. We extract $\mu_0 H_A^{sat} = 1.15$ T and $\mu_0 H_B^{flip} = 0.45$ T from these spin flip and saturation fields, which is in good agreement with the XMCD-measured values. Using

these 3 measured values, we can uniquely solve for the interaction terms and find $J = 71.8\,\mu eV$, W= 16.7 μeV and 8K $= 82.7\,\mu eV$, with a ratio $\frac{J}{8K+W} = 0.72 < 1$ satisfying the sharp spin flip criterion. Therefore, we find that the Eu-Eu interaction is much stronger for Eu moments aligned parallel ($J_x = J + W = 88.5\,\mu eV$) compared to perpendicular ($J_y = J - W = 55.1\,\mu eV$) to Fe moments. Further, the normalized difference of the anisotropic interplanar interaction, $\frac{J_x - J_y}{J_x + J_y} = 23.3\%$, is nearly two orders of magnitude greater than the corresponding normalized difference of in-plane lattice constants (the orthorhombicity), $\frac{a-b}{a+b} \sim 0.28\%$, which strongly implies the Fe-SDW origin of the anisotropy.

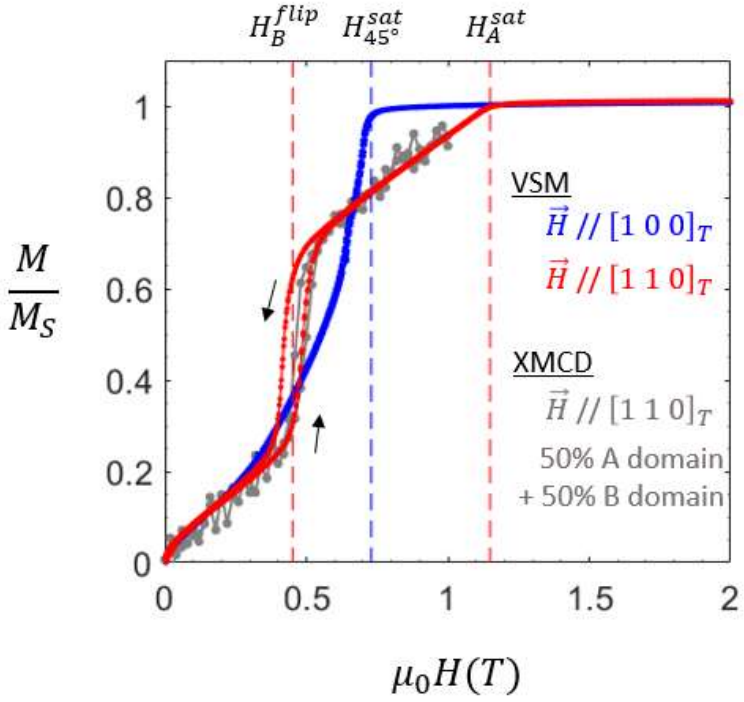

Figure 7.10 Octagon sample magnetization with field applied along the tetragonal $[1\,0\,0]_T$ (blue) and $[1\,1\,0]_T$ (red) directions. Critical fields marked by dashed lines. Magnetization normalized by 1T saturation value along $[1\,0\,0]_T$. (grey) Average of the two domain XMCD data of Fig.7.6a, normalized by the B domain saturated value at 1T.

7.12 DFT and proposed origin of anisotropic Eu-Eu coupling

To gain more insight, we used density functional theory (DFT) to calculate the exchange coupling between Eu layers as the difference between ferro- and antiferromagnetically stacked Eu layers, for Eu moments parallel and perpendicular to the Fe moments. We used the standard VASP package [131], [132], and verified that the results were fully converged with respect to the Brillouin zone integration,

plane wave cutoff, and the number of bands included in the diagonalization. We also varied the effective Hubbard repulsion parameter for Eu *f* orbitals, U-J, between 5 and 7 eV, which had little impact on the result. We find that for parallel Eu-Fe moments, J_{x}=150-170 μeV, while for perpendicular Eu-Fe moments, J_{y} is essentially zero. While this result seems to considerably overestimate the exchange anisotropy (see ref. [118], Supplementary Materials Section 1A, for a discussion of the difficulties of DFT calculation for noncollinear Eu-Fe moments, which we assume contributes to this overestimation), it clearly shows that DFT calculations also support a strongly anisotropic Eu interplanar interaction.

The anisotropic interaction between Eu planes can be thought to result from the anisotropic hopping of conduction electrons through the Fe plane. Considering a standard superexchange interaction, conduction electrons with spins polarized along the Eu direction will generally have a larger Eu-Fe hopping amplitude t when the Eu and Fe moments are parallel ($J_x = J + W$) rather than perpendicular ($J_y = J - W$), which generates a stronger antiferromagnetic interaction for collinear Eu-Fe moments. Further, the weak but finite *ferromagnetic* interaction between Eu planes is also mediated through the Fe layer, and as the Fe moments have a much larger susceptibility perpendicular to their ordering direction, the ferromagnetic interaction is stronger for perpendicular Eu and Fe moments, which weakens their overall effective *antiferromagnetic* interaction (this can be considered an extreme case of the RKKY interaction). In this sense, we can view this Eu interplanar interaction anisotropy (W) as a generalized Eu-Fe biquadratic coupling independent of the previously investigated Eu-Fe biquadratic coupling (K), where the square of Fe moments $\left(f_{i,x}^2 - f_{i,y}^2\right)$ couples the Eu moments above and below the iron plane. We note that this picture is reminiscent of the Fe-Fe biquadratic coupling within the FeAs plane that generates an effective anisotropic in-plane exchange of Fe moments $J_{1a} - J_{1b}$ [36]. These types of interactions have been long overlooked in the past, but are relevant to rare-earth and transition metal intermetallic systems with multiple magnetic orders[133], [134].

A complete determination of the spin Hamiltonian in $EuFe_2As_2$ also sheds light on the doping dependence of Eu magnetic order, which has yet to be fully understood. As in other iron pnictides, chemical doping in $EuFe_2As_2$ rapidly suppresses the Fe-SDW and stabilizes superconductivity [135]–[143]. In contrast, the doping has only a weak effect on the magnetic ordering temperature in the Eu layer, but causes a smooth evolution from an A-type AFM order to a c-axis canted AFM order (c-AFM), and finally to a c-axis ferromagnetic order (FM) [81], [85], [124], [126], [135], [143]–[146]. This doping dependence can be naturally understood as the consequence of Eu moments lowering their energy by aligning with the Fe-SDW, with this energy saving being gradually diminished as doping weakens the Fe-SDW. Further, in the parent compound both the Fe-SDW and Eu-AFM are robust under moderate hydrostatic pressure even as superconductivity develops [147], while in the underdoped case a pressure-induced transition from c-AFM to FM occurs only after the SDW is nearly fully suppressed[148]. This suggests the SDW plays a role in both the orientation and the interaction of Eu moments. Future doping dependence studies may provide more insight on how the Eu interlayer interaction is influenced by the various orders in the FeAs plane, including by superconductivity[149].

7.13 Conclusion

In conclusion, our sample environment allows us to approach the magnetic coupling and magnetotransport properties of the $EuFe_2As_2$ system in an unprecedented fashion. Through mechanical stress we can prevent field detwinning and gain access to the meta-magnetism and the associated magnetotransport behavior of a monodomain sample. From measurements of the spin flip and moment saturation fields we are able to determine the strengths of coupling between Eu and Fe planes and discover the presence of an anisotropic exchange term in the spin Hamiltonian. We emphasize again that in a freestanding crystal, the rapid field-detwinning has prevented any previous determination of the anisotropic Eu interplanar interaction in this system. This new technique not only deepens our understanding of the $EuFe_2As_2$ system, but can also be applied to a variety of systems to disentangle the strongly coupled spin, orbit and lattice degree of freedom.

Chapter 8:
Thesis Conclusion

This thesis set out to answer old and new questions in iron pnictide materials about how nematicity, magnetism, and the crystal lattice are coupled, and how well the transport represents the nematicity. To make progress in this effort, it was necessary to develop a new technique to enable in-situ structural and magnetic tuning of a sample with structural and magnetic characterization via x-ray techniques and electronic characterization via transport measurements. Over the course of my thesis work I developed just such a system which has produced its first results. We have demonstrated that the resistivity anisotropy can indeed be treated as a reliable proxy of the nematicity in a nonmagnetic nematic ordered or disordered phase of $Ba(Fe_{.96}Co_{.04})_2As_2$ and likely in a much broader range of iron-based superconductors. This thesis presents a new methodology that can confirm this result across materials and potentially discover new phenomena such as the dissociation between lattice distortion and transport anisotropy under large strain. When incorporating magnetic x-ray techniques, we were able to show that nematic conduction electrons mediate a large anisotropic coupling between localized Eu magnetic moments, resulting in a metamagnetic spin flip transition in response to applied magnetic field. This strain + field + x-ray methodology can likewise now be applied to a large class of materials with diverse magnetic structures and strong magnetostructural coupling. This ability to perform multimodal characterization of complex materials represents an important advancement in the tools available to condensed matter physicists and is only at the beginning of its utility to the field.

Chapter 9:
Appendix

9.1 Crystal Growth

Single crystal samples of $Ba(Fe_{1-x}Co_x)_2As_2$ were grown from an FeAs flux as described in ref. [55].

Single crystal samples of $EuFe_2As_2$ were grown from a tin flux as described in ref. [124].

Single crystal samples of $Eu(Fe_{.85}Co_{.15})_2As_2$ were grown from a tin flux as described in ref. [124], however, an FeCo rich growth was found to enhance superconducting properties, and the sample used in Chapter 5 used a nonstoichiometric molar growth ratio of Eu:($Fe_{.85}Co_{.15}$):As:Sn = 1:8:2:19.

As a service component of my UW Clean Energy Institute fellowship (2016-2017), I made a short video detailing the steps of growing and preparing a 4-point measurement on a single crystal sample. Link

9.2 Extraction of Shear Modulus from Poisson Ratio.

We consider an applied uniaxial stress along the $\hat{x}$ direction τ_x which induces a uniaxial strain ε_{xx} along the $\hat{x}$ direction in a single crystal sample. In response to the induced uniaxial strain, the two transverse lattice constants also experience uniaxial strains $\varepsilon_{yy} = -\nu_{xy}\varepsilon_{xx}$, and $\varepsilon_{zz} = -\nu_{xz}\varepsilon_{xx}$, where ν_{xi} is the Poisson's ratio for each direction. In Chapter 6 we use the xyz coordinate basis of the 4-Fe unit cell but continue to use the irreducible representation names appropriate for the 2-Fe unit cell, which complicates the determination of ν_{xy} in terms of the components of the elastic modulus tensor. The 4-Fe uniaxial strains ε_{xx}, ε_{yy}, and ε_{zz} compose the antisymmetric B_{2g} and symmetric A_{1g} strains, defined as

$$\varepsilon_{B_{2g}} = \frac{1}{2}(\varepsilon_{xx} - \varepsilon_{yy}) = \frac{1}{2}\varepsilon_{xx}(1 + \nu_{xy})$$
$$\varepsilon_{A_{1g,1}} = \frac{1}{2}(\varepsilon_{xx} + \varepsilon_{yy}) = \frac{1}{2}\varepsilon_{xx}(1 - \nu_{xy})$$
$$\varepsilon_{A1g,2} = \varepsilon_{zz} = -\varepsilon_{xx}\nu_{xz}$$

The strain $\varepsilon_{B_{2g}}$ is equivalent to the in-plane orthorhombicity that is created by the nematic order (ε in the main text), i.e. the nematicity and $\varepsilon_{B_{2g}}$ are both in the B_{2g} symmetry channel. The shear modulus C_{66} is also in this B_{2g} symmetry channel and so nematic fluctuations effectively soften the shear modulus. We may relate our applied uniaxial stress to the shear modulus through consideration of the full compliance tensor. However, given our choice for the xyz coordinate system, we must also rotate the compliance tensor from the tetragonal unit cell basis to our chosen xyz basis via a 45 degree rotation.

For a tetragonal crystal, the stiffness tensor takes the form

$$C = \begin{pmatrix} C_{11} & C_{12} & C_{13} & 0 & 0 & 0 \\ C_{12} & C_{11} & C_{13} & 0 & 0 & 0 \\ C_{13} & C_{13} & C_{33} & 0 & 0 & 0 \\ 0 & 0 & 0 & C_{44} & 0 & 0 \\ 0 & 0 & 0 & 0 & C_{44} & 0 \\ 0 & 0 & 0 & 0 & 0 & C_{66} \end{pmatrix}$$

The compliance tensor is the inverse of the stiffness tensor, so we have

$$S = C^{-1} = \begin{pmatrix} \frac{-C_{13}{}^2 + C_{11}C_{33}}{A} & \frac{+C_{13}{}^2 - C_{12}C_{33}}{A} & \frac{C_{13}}{B^+} & 0 & 0 & 0 \\ \frac{+C_{13}{}^2 - C_{12}C_{33}}{A} & \frac{-C_{13}{}^2 + C_{11}C_{33}}{A} & \frac{C_{13}}{B^+} & 0 & 0 & 0 \\ \frac{C_{13}}{B^+} & \frac{C_{13}}{B^+} & \frac{C_{11} + C_{12}}{B^-} & 0 & 0 & 0 \\ 0 & 0 & 0 & \frac{1}{C_{44}} & 0 & 0 \\ 0 & 0 & 0 & 0 & \frac{1}{C_{44}} & 0 \\ 0 & 0 & 0 & 0 & 0 & \frac{1}{C_{66}} \end{pmatrix}$$

where *A* = $(C_{11} - C_{12})(-2C_{13}{}^2 + C_{33}(C_{11} + C_{12})$ and $B^{\pm} = \pm(2C_{13}{}^2 - C_{33}(C_{11} + C_{12}))$.

This matrix is in the basis of the tetragonal lattice. We rotate the in-plane axes by 45 degrees with respect to this basis as

$$S' = K^{-T} S K^{-1}$$

where *K* is the rotation matrix given by

$$K = \begin{pmatrix} c^2 & c^2 & 0 & 0 & 0 & 2cs \\ c^2 & c^2 & 0 & 0 & 0 & -2cs \\ 0 & 0 & 1 & 0 & 0 & 0 \\ 0 & 0 & 0 & c & s & 0 \\ 0 & 0 & 0 & -s & c & 0 \\ -cs & cs & 0 & 0 & 0 & c^2 - s^2 \end{pmatrix}$$

and $c = \cos(45°), s = \sin(45°)$.

This then gives the rotated compliance tensor:

$$S' = \begin{pmatrix} \frac{C_{33}}{-2B^-} + \frac{1}{4C_{66}} & \frac{C_{33}}{-2B^-} - \frac{1}{4C_{66}} & \frac{C_{13}}{B^+} & 0 & 0 & 0 \\ \frac{C_{33}}{-2B^-} - \frac{1}{4C_{66}} & \frac{C_{33}}{-2B^-} + \frac{1}{4C_{66}} & \frac{C_{13}}{B^+} & 0 & 0 & 0 \\ \frac{C_{13}}{B^+} & \frac{C_{13}}{B^+} & \frac{C_{11+}C_{12}}{B^-} & 0 & 0 & 0 \\ 0 & 0 & 0 & \frac{1}{2C_{44}} & 0 & 0 \\ 0 & 0 & 0 & 0 & \frac{1}{2C_{44}} & 0 \\ 0 & 0 & 0 & 0 & 0 & \frac{2}{C_{11} - C_{12}} \end{pmatrix}$$

Finally, the Poisson ratios are given by

$$\nu_{xy} = -\frac{\varepsilon_{yy}}{\varepsilon_{xx}} = -\frac{S'_{12}}{S'_{11}} = \frac{-C_{13}^2 + \frac{1}{2}(C_{11} + C_{12})C_{33} - C_{33}C_{66}}{-C_{13}^2 + \frac{1}{2}(C_{11} + C_{12})C_{33} + C_{33}C_{66}}$$

$$\nu_{xz} = -\frac{\varepsilon_{zz}}{\varepsilon_{xx}} = -\frac{S'_{13}}{S'_{11}} = \frac{2C_{13}C_{66}}{-C_{13}^2 + \frac{1}{2}(C_{11} + C_{12})C_{33} + C_{33}C_{66}}$$

We solve for the shear modulus C_{66} in terms of the in-plane Poisson ratio ν_{xy} as

$$C_{66} = \left(\frac{1}{2}(C_{11} + C_{12}) - \frac{C_{13}^2}{C_{33}}\right)\left(\frac{1 - \nu_{xy}}{1 + \nu_{xy}}\right)$$

$$C_{66} = (50.5\ GPa)\frac{1 - \nu_{xy}}{1 + \nu_{xy}}$$

We determine the magnitude from ultrasound data for an x=0.037 sample from ref. [68], using the measured values of C_{11}, C_{12} and C_{33}, and taking $C_{13} = \frac{1}{2}C_{12}$. The magnitude is nearly temperature-independent over this temperature range, reflecting the small impact that diverging nematic fluctuations have on the other elastic modulus terms. The exact value of the magnitude is not critical to our analysis as it only changes the fit parameter "$C_{66,0}$" and not the temperature dependence. Still, the fitted value of $C_{66,0} = 38.8 \pm 4.7\ GPa$ is in excellent agreement with the high temperature limit of the measured C_{66} presented in ref [68]. Using the values of ν_{xy} extracted from Fig.6.5a, we calculate C_{66} to yield Fig.6.5b.

In principle, we could also determine the shear modulus from the divergence of the out of plane Poisson ratio ν_{xz}. In this case, ν_{xz} approaches zero at T_S and so we encounter the difficulty of accurately measuring a diminishing value. In contrast, ν_{xy} approaches its maximum value of 1 at T_S, giving stronger evidence that C_{66} actually does approach zero at the structural transition.

Bibliography

[1] Y. Kamihara, T. Watanabe, M. Hirano, and H. Hosono, “Iron-based layered superconductor La[O1-xFx]FeAs (x=0.05-0.12) with T_c = 26 K,” *J. Am. Chem. Soc.*, vol. 130, no. 11, p. 3296, 2008.

[2] D. Van Delft and P. Kes, “The discovery of superconductivity,” *Phys. Today*, vol. 63, no. 9, pp. 38–43, Sep. 2010.

[3] C. Fang, H. Yao, W. F. Tsai, J. Hu, and S. A. Kivelson, “Theory of electron nematic order in LaFeAsO,” *Phys. Rev. B*, vol. 77, no. 22, p. 224509, Jun. 2008.

[4] S. Lederer, Y. Schattner, E. Berg, and S. A. Kivelson, “Enhancement of superconductivity near a nematic quantum critical point,” *Phys. Rev. Lett.*, vol. 114, no. 9, p. 097001, Mar. 2015.

[5] J. J. Sanchez *et al.*, “The transport–structural correspondence across the nematic phase transition probed by elasto X-ray diffraction,” *Nat. Mater.*, Aug. 2021.

[6] J. Chu, H. Kuo, J. G. Analytis, and I. R. Fisher, “Divergent nematic susceptibility in an iron arsenide superconductor,” vol. 1, no. D, pp. 1–8, 2012.

[7] S. Zapf and M. Dressel, “Europium-based iron pnictides: A unique laboratory for magnetism, superconductivity and structural effects,” *Reports Prog. Phys.*, vol. 80, no. 1, p. 016501, Jan. 2017.

[8] P. Malinowski *et al.*, “Suppression of superconductivity by anisotropic strain near a nematic quantum critical point,” *Nat. Phys.*, 2020.

[9] J. J. Sanchez *et al.*, “Strongly anisotropic antiferromagnetic coupling in EuFe2As2 revealed by stress detwinning,” *arXiv: 2012.00623*, Dec. 2020.

[10] J. A. Johnson, “Populating the periodic table: Nucleosynthesis of the elements,” *Science.*, vol. 363, pp. 474–478, 2019.

[11] I. R. Fisher, M. C. Shapiro, and J. G. Analytis, “Principles of crystal growth of intermetallic and oxide compounds from molten solutions,” *Philos. Mag.*, vol. 92, no. 19–21, 2012.

[12] T. Nakamuro, M. Sakakibara, H. Nada, K. Harano, and E. Nakamura, “Capturing the Moment of Emergence of Crystal Nucleus from Disorder,” *J. Am. Chem. Soc.*, vol. 143, no. 4, pp. 1763–1767, Feb. 2021.

[13] J. Russo and H. Tanaka, “Crystal nucleation as the ordering of multiple order parameters,” *J. Chem. Phys.*, vol. 145, no. 21, p. 211801, Dec. 2016.

[14] M. Tinkham, *Group Theory And Quantum Mechanics*. McGraw-Hill, New York: Dover, 1964.

[15] M. Shatruk, “ThCr 2 Si 2 structure type: The ‘perovskite’ of intermetallics ☆,” *J. Solid State Chem.*, vol. 272, pp. 198–209, 2019.

[16] F. jie Ma, Z. yi Lu, and T. Xiang, “Electronic structures of ternary iron arsenides AFe2As2 (A = Ba, Ca, or Sr),” *Frontiers of Physics in China*, vol. 5, no. 2. Springer, pp. 150–160, 13-Jun-2010.

[17] C. H. Lin, T. Berlijn, L. Wang, C. C. Lee, W. G. Yin, and W. Ku, “One-Fe versus Two-Fe Brillouin zone of Fe-based superconductors: Creation of the electron pockets by translational symmetry breaking,” *Phys. Rev. Lett.*, vol. 107, no. 25, p. 257001, Dec. 2011.

[18] R. A. Ewings *et al.*, “High-energy spin excitations in BaFe2As2 observed by inelastic neutron scattering,” *Phys. Rev. B*, vol. 78, no. 22, p. 220501, Dec. 2008.

[19] D. J. Singh, “Electronic structure of Fe-based superconductors,” *Phys. C Supercond. its Appl.*, vol. 469, no. 9–12, pp. 418–424, May 2009.

[20] J. Paglione and R. L. Greene, “High-temperature superconductivity in iron-based materials,” *Nat. Phys. 6, 645-658*, 2010.

[21] H. Ikeda, R. Arita, and J. Kuneš, “Phase diagram and gap anisotropy in iron-pnictide superconductors,” *Phys. Rev. B*, vol. 81, no. 5, p. 054502, Feb. 2010.

[22] M. Yi *et al.*, “Symmetry-breaking orbital anisotropy observed for detwinned Ba(Fe 1-xCox)2As2 above the spin density wave transition,” *PNAS*, vol. 108, no. 17, pp. 6878–6883, Apr. 2011.

[23] S. Kasahara *et al.*, “Evolution from non-Fermi- to Fermi-liquid transport via isovalent doping in BaFe 2 (As 1 − x P x) 2 superconductors,” *Phys. Rev. B*, vol. 81, no. 18, p. 184519, May 2010.

[24] I. I. Mazin, D. J. Singh, M. D. Johannes, and M. H. Du, “Unconventional superconductivity with a sign reversal in the order parameter of LaFeAsO1-xFx,” *Phys. Rev. Lett.*, vol. 101, no. 5, p. 057003, Jul. 2008.

[25] L. Fang *et al.*, “Roles of multiband effects and electron-hole asymmetry in the superconductivity and normal-state properties of Ba (Fe1-x Co x)2As2,” *Phys. Rev. B*, vol. 80, no. 14, p. 140508, Oct. 2009.

[26] M. Nakajima *et al.*, “Normal-state charge dynamics in doped BaFe 2 As 2: Roles of doping and necessary ingredients for superconductivity,” *Sci. Rep.*, vol. 4, no. 1, pp. 1–6, Jul. 2014.

[27] J. H. Chu, J. G. Analytis, C. Kucharczyk, and I. R. Fisher, “Determination of the phase diagram of the electron-doped superconductor Ba (Fe1-x Cox)2 As2,” *Phys. Rev. B*, vol. 79, no. 1, 2009.

[28] I. I. Mazin and J. Schmalian, “PAIRING SYMMETRY AND PAIRING STATE IN FERROPNICTIDES: THEORETICAL OVERVIEW,” *Phys. C Supercond. its Appl.*, vol. 469, no. 9–12, pp. 614–627, 2009.

[29] S. E. Sebastian *et al.*, “Quantum oscillations in the parent magnetic phase of an iron arsenide high temperature superconductor,” *J. Phys. Condens. Matter*, vol. 20, no. 42, p. 422203, Oct. 2008.

[30] S. Dugdale, “Life on the edge: a beginner’s guide to the Fermi surface,” IOP Publishing, Apr. 2016.

[31] R. M. Fernandes, A. V. Chubukov, and J. Schmalian, “What drives nematic order in iron-based superconductors?,” *Nat. Phys.*, vol. 10, no. 2, pp. 97–104, Feb. 2014.

[32] P. Dai, “Antiferromagnetic order and spin dynamics in iron-based superconductors,” *Rev. Mod. Phys.*, vol. 87, no. 3, p. 855, Aug. 2015.

[33] C. Wang *et al.*, “Longitudinal spin excitations and magnetic anisotropy in antiferromagnetically ordered BaFe2As2,” *Phys. Rev. X*, vol. 3, no. 4, p. 041036, Dec. 2013.

[34] P. Dai, J. Hu, and E. Dagotto, “Magnetism and its microscopic origin in iron-based high-temperature superconductors,” *Nat. Phys.*, vol. 8, no. 10, pp. 709–718, Oct. 2012.

[35] J. Zhao *et al.*, “Spin waves and magnetic exchange interactions in CaFe 2 As 2,” *Nat. Phys.*, vol. 5, no. 8, pp. 555–560, Jul. 2009.

[36] A. L. Wysocki, K. D. Belashchenko, and V. P. Antropov, “Consistent model of magnetism in ferropnictides,” *Nat. Phys.*, vol. 7, no. 6, pp. 485–489, Mar. 2011.

[37] R. M. Fernandes, A. V. Chubukov, J. Knolle, I. Eremin, and J. Schmalian, “Preemptive nematic order, pseudogap, and orbital order in the iron pnictides,” *Phys. Rev. B*, vol. 85, no. 2, 2012.

[38] J. H. Chu *et al.*, “In-plane electronic anisotropy in underdoped Ba(Fe1-xCo x)2As2 revealed by partial detwinning in a magnetic field,” *Phys. Rev. B*, vol. 81, no. 21, 2010.

[39] J.-H. Chu *et al.*, “In-Plane Resistivity Anisotropy in an Underdoped Iron Arsenide Superconductor,” *Science.*, vol. 329, no. August, pp. 824–826, 2010.

[40] T. Kissikov *et al.*, “Uniaxial strain control of spin-polarization in multicomponent nematic order of BaFe2As2,” *Nat. Commun.*, vol. 9, no. 1, p. 1058, Dec. 2018.

[41] M. Fu, D. A. Torchetti, T. Imai, F. L. Ning, J. Q. Yan, and A. S. Sefat, “NMR search for the spin nematic state in a LaFeAsO single crystal,” *Phys. Rev. Lett.*, vol. 109, no. 24, p. 247001, Dec. 2012.

[42] E. Fradkin, S. A. Kivelson, M. J. Lawler, J. P. Eisenstein, and A. P. Mackenzie, “Nematic Fermi Fluids in Condensed Matter Physics,” *Annu. Rev. Condens. Matter Phys.*, vol. 1, no. 1, pp. 153–178, Oct. 2010.

[43] M. Carpenter *et al.*, “Ferroelasticity, anelasticity and magnetoelastic relaxation in Co-doped iron pnictide: $Ba(Fe_{0.957}Co_{0.043})_2As_2$,” *J. Phys. Condens. Matter*, vol. 31, no. 155401, 2019.

[44] R. M. Fernandes and J. Schmalian, “Manifestations of nematic degrees of freedom in the magnetic, elastic, and superconducting properties of the iron pnictides,” *Supercond. Sci. Technol.*, vol. 25, no. 8, p. 17, Aug. 2012.

[45] M. G. Kim *et al.*, “Character of the structural and magnetic phase transitions in the parent and electron-doped $BaFe_2As_2$ compounds,” *Phys. Rev. B*, vol. 83, no. 13, p. 134522, Apr. 2011.

[46] R. M. Fernandes *et al.*, “Effects of Nematic Fluctuations on the Elastic Properties of Iron Arsenide Superconductors,” *Phys. Rev. Lett.*, vol. 105, no. 15, p. 157003, Oct. 2010.

[47] D. D. Khalyavin *et al.*, “Symmetry of reentrant tetragonal phase in Ba1-xNaxFe2As2: Magnetic versus orbital ordering mechanism,” *Phys. Rev. B*, vol. 90, no. 17, p. 174511, Nov. 2014.

[48] R. M. Fernandes, P. P. Orth, and J. Schmalian, “Intertwined Vestigial Order in Quantum Materials: Nematicity and Beyond,” *Annu. Rev. Condens. Matter Phys.*, vol. 10, no. 1, pp. 133–154, Mar. 2019.

[49] C. Xu, M. Müller, and S. Sachdev, “Ising and spin orders in the iron-based superconductors,” *Phys. Rev. B*, vol. 78, no. 2, p. 020501, Jul. 2008.

[50] Z. P. Yin and W. E. Pickett, “Antiphase magnetic boundaries in iron-based superconductors: A first-principles density-functional theory study,” *Phys. Rev. B*, vol. 80, no. 14, p. 144522, Oct. 2009.

[51] M. G. Kim *et al.*, “Imaging antiferromagnetic antiphase domain boundaries using magnetic Bragg diffraction phase contrast,” *Nat. Commun.*, vol. 9, no. 1, pp. 1–7, Dec. 2018.

[52] T. Kissikov *et al.*, “Local nematic susceptibility in stressed BaFe 2 As 2 from NMR electric field gradient measurements,” *Phys. Rev. B*, vol. 96, no. 24, p. 241108, Dec. 2017.

[53] M. Yoshizawa *et al.*, “Structural Quantum Criticality and Superconductivity in Iron-Based Superconductor $Ba(Fe_{1-x}Co_x)_2As_2$,” *J. Phys. Soc. Japan*, vol. 81, no. 2, p. 024604, Feb. 2012.

[54] A. E. Böhmer *et al.*, “Nematic Susceptibility of Hole-Doped and Electron-Doped $BaFe_2As_2$ Iron-Based Superconductors from Shear Modulus Measurements,” *Phys. Rev. Lett.*, vol. 112, no. 4, p. 047001, Jan. 2014.

[55] H. H. Kuo, J. H. Chu, J. C. Palmstrom, S. A. Kivelson, and I. R. Fisher, “Ubiquitous signatures of nematic quantum criticality in optimally doped Fe-based superconductors,” *Science.*, vol. 352, no. 6288, pp. 958–962, May 2016.

[56] M. S. Ikeda, T. Worasaran, E. W. Rosenberg, J. C. Palmstrom, S. A. Kivelson, and I. R. Fisher, “Elastocaloric signature of nematic fluctuations,” *arXiv:2101.00080*, Dec. 2020.

[57] M. A. Tanatar *et al.*, “Direct imaging of the structural domains in the iron pnictides AFe_2As_2 (A=Ca,Sr,Ba),” *Phys. Rev. B*, vol. 79, no. 18, pp. 1–4, 2009.

[58] N. R. Poniatowski, “Superconductivity, Broken Gauge Symmetry, and the Higgs Mechanism,” *arXiv*, vol. 87, no. 6. arXiv, pp. 436–443, 19-May-2019.

[59] T. H. Hansson, V. Oganesyan, and S. L. Sondhi, “Superconductors are topologically ordered,” *Ann. Phys. (N. Y).*, vol. 313, no. 2, pp. 497–538, Oct. 2004.

[60] I. I. Mazin, “Superconductivity gets an iron boost,” *Nature*, vol. 464, no. 7286. Nature Publishing Group, pp. 183–186, 11-Mar-2010.

[61] D. K. Pratt *et al.*, “Coexistence of competing antiferromagnetic and superconducting phases in the underdoped Ba(Fe0.953Co0.047)2As2 compound using X-ray and neutron scattering techniques,” *Phys. Rev. Lett.*, vol. 103, no. 8, p. 087001, Aug. 2009.

[62] R. M. Fernandes *et al.*, “Unconventional pairing in the iron arsenide superconductors,” *Phys. Rev. B*, vol. 81, no. 14, p. 140501, Apr. 2010.

[63] S. Nandi *et al.*, “Anomalous suppression of the orthorhombic lattice distortion in superconducting $Ba(Fe_{1-x}Co_x)_2As_2$ single crystals,” *Phys. Rev. Lett.*, vol. 104, no. 5, p. 057006, Feb. 2010.

[64] L. Landau, “On the theory of phase transitions,” *Zh.Eksp.Teor.Fiz.*, vol. 7, 1937.

[65] A. E. Böhmer and C. Meingast, “Electronic nematic susceptibility of iron-based superconductors,” *Comptes Rendus Phys.*, vol. 17, no. 1–2, pp. 90–112, Jan. 2016.

[66] S. Kasahara *et al.*, “Electronic nematicity above the structural and superconducting transition in BaFe2(As1−xP x)2,” *Nature*, vol. 486, no. 7403, pp. 382–385, Jun. 2012.

[67] A. Cano, M. Civelli, I. Eremin, and I. Paul, “Interplay of magnetic and structural transitions in iron-based pnictide superconductors,” *Phys. Rev. B*, vol. 82, no. 2, p. 020408, Jul. 2010.

[68] C. Fujii *et al.*, “Anisotropic Grüneisen Parameter and Diverse Order Parameter Fluctuations in

Iron-Based Superconductor $Ba(Fe_{1-x}Co_x)_2As_2$," *J. Phys. Soc. Japan*, vol. 87, no. 7, p. 074710, Jul. 2018.

[69] V. K. Wadhawan, "Ferroelasticity," *Bull. Mater. Sci.*, vol. 6, no. 4, pp. 733–753, Sep. 1984.

[70] Z. Liu *et al.*, "Nematic Quantum Critical Fluctuations in BaFe2-xNixAs2," *Phys. Rev. Lett.*, vol. 117, no. 15, p. 157002, Oct. 2016.

[71] Y. Gallais *et al.*, "Observation of incipient charge nematicity in Ba(Fe1-XCoX)2As2," *Phys. Rev. Lett.*, vol. 111, no. 26, Dec. 2013.

[72] Y. Gallais and I. Paul, "Charge nematicity and electronic Raman scattering in iron-based superconductors," *Comptes Rendus Physique*, vol. 17, no. 1–2. Elsevier Masson SAS, pp. 113–139, 01-Jan-2016.

[73] T. Goto *et al.*, "Quadrupole Effects of Layered Iron Pnictide Superconductor Ba(Fe 0.9 Co 0.1) 2 As 2," *J. Phys. Soc. Japan*, vol. 80, no. 7, p. 073702, Jul. 2011.

[74] M. Blume, "Relativistic Calculation of Anomalous Scattering Factors for X," *Rays J. Chem. Phys.*, vol. 57, p. 1891, 1985.

[75] G. H. Lander and W. G. Stirling, "Magnetic x-ray scattering," *Phys. Scr.*, vol. 1999, no. T45, pp. 15–21, Jan. 1999.

[76] C. H. Payne, "Stellar Atmospheres; a Contribution to the Observational Study of High Temperature in the Reversing Layers of Stars.," Radcliffe College, 1925.

[77] Z. Fei *et al.*, "Two-dimensional itinerant ferromagnetism in atomically thin Fe3GeTe2," *Nature Materials*, vol. 17, no. 9. Nature Publishing Group, pp. 778–782, 01-Sep-2018.

[78] X. Tan *et al.*, "A Transition from Localized to Strongly Correlated Electron Behavior and Mixed Valence Driven by Physical or Chemical Pressure in ACo 2 As 2 (A = Eu and Ca)," *J. Am. Chem. Soc.*, vol. 138, no. 8, pp. 2724–2731, Mar. 2016.

[79] J. H. Kang *et al.*, "Superconductivity in undoped BaFe2As2by tetrahedral geometry design," *Proc. Natl. Acad. Sci. U. S. A.*, vol. 117, no. 35, pp. 21170–21174, Sep. 2020.

[80] J. A. W. Straquadine, M. S. Ikeda, and I. R. Fisher, "Evidence for realignment of the charge density wave state in ErTe$_3$ and TmTe$_3$ under uniaxial stress via elastocaloric and elastoresistivity measurements," May 2020.

[81] J. Herrero-Martín *et al.*, "Magnetic structure of EuFe2 As2 as determined by resonant x-ray scattering," *Phys. Rev. B*, vol. 80, no. 13, p. 134411, Oct. 2009.

[82] H. Zhang *et al.*, "Deterministic Control of Metamagnetic Transition of Antiferromagnetic Mott Insulator Sr2IrO4 by in-situ Anisotropic Strain," Nov. 2019.

[83] J. Kim *et al.*, "Spin-split conduction band in EuB 6 and tuning of half-metallicity with external stimuli," *Phys. Rev. B*, vol. 87, no. 15, p. 155104, Apr. 2013.

[84] M. S. Ikeda, T. Worasaran, J. C. Palmstrom, J. A. W. Straquadine, P. Walmsley, and I. R. Fisher, "Symmetric and antisymmetric strain as continuous tuning parameters for electronic nematic order," *Phys. Rev. B*, vol. 98, no. 24, pp. 1–6, 2018.

[85] V. H. Tran, T. A. Zaleski, Z. Bukowski, L. M. Tran, and A. J. Zaleski, "Tuning superconductivity in

Eu(Fe 0.81Co 0.19) 2As 2 with magnetic fields," *Phys. Rev. B*, vol. 85, no. 5, p. 052502, Feb. 2012.

[86] M. C. Shapiro, A. T. Hristov, J. C. Palmstrom, J. Chu, and I. R. Fisher, "Measurement of the B_{1g} and B_{2g} components of the elastoresistivity tensor for tetragonal materials via transverse resistivity configurations," *Rev. Sci. Instrum.*, vol. 063902, no. 87, 2016.

[87] S. Ishida *et al.*, "Anisotropy of the In-Plane Resistivity of Underdoped $Ba(Fe_{1-x}Co_x)_2As_2$ Superconductors Induced by Impurity Scattering in the Antiferromagnetic Orthorhombic Phase," *Phys. Rev. Lett.*, vol. 110, no. 20, p. 207001, May 2013.

[88] M. N. Gastiasoro, I. Paul, Y. Wang, P. J. Hirschfeld, and B. M. Andersen, "Emergent defect states as a source of resistivity anisotropy in the nematic phase of iron pnictides," *Phys. Rev. Lett.*, vol. 113, no. 12, p. 127001, Sep. 2014.

[89] R. M. Fernandes, E. Abrahams, and J. Schmalian, "Anisotropic in-plane resistivity in the nematic phase of the iron pnictides," *Phys. Rev. Lett.*, vol. 107, no. 21, p. 217002, Nov. 2011.

[90] H. H. Kuo and I. R. Fisher, "Effect of disorder on the resistivity anisotropy near the electronic nematic phase transition in pure and electron-doped $BaFe_2As_2$," *Phys. Rev. Lett.*, vol. 112, no. 22, p. 227001, Jun. 2014.

[91] Y. Cao *et al.*, "Nematicity and Competing Orders in Superconducting Magic-Angle Graphene," *Science.*, vol. 372, no. 6539, Apr. 2021.

[92] X. Chen, S. Maiti, R. M. Fernandes, and P. J. Hirschfeld, "Nematicity and superconductivity: Competition versus cooperation," *Phys. Rev. B*, vol. 102, p. 184512, 2020.

[93] M. A. Tanatar *et al.*, "Uniaxial-strain mechanical detwinning of $CaFe_2As_2$ and $BaFe_2As_2$ crystals: Optical and transport study," *Phys. Rev. B*, vol. 81, no. 18, p. 184508, May 2010.

[94] C. W. Hicks, M. E. Barber, S. D. Edkins, D. O. Brodsky, and A. P. Mackenzie, "Piezoelectric-based apparatus for strain tuning," *Rev. Sci. Instrum.*, vol. 85, no. 6, p. 065003, Jun. 2014.

[95] J. C. Palmstrom, A. T. Hristov, S. A. Kivelson, J. H. Chu, and I. R. Fisher, "Critical divergence of the symmetric (A_{1g}) nonlinear elastoresistance near the nematic transition in an iron-based superconductor," *Phys. Rev. B*, vol. 96, no. 205133, 2017.

[96] J. G. Analytis *et al.*, "Quantum oscillations in the parent pnictide $BaFe_2As_2$: Itinerant electrons in the reconstructed state," *Phys. Rev. B*, vol. 80, no. 6, p. 064507, Aug. 2009.

[97] T. Shimojima *et al.*, "Orbital-Dependent modifications of electronic structure across the magnetostructural transition in $BaFe_2As_2$," *Phys. Rev. Lett.*, vol. 104, no. 5, p. 057002, Feb. 2010.

[98] M. Nakajima *et al.*, "Unprecedented anisotropic metallic state in undoped iron arsenide $BaFe_2As_2$ revealed by optical spectroscopy," *Proc. Natl. Acad. Sci. U. S. A.*, vol. 108, no. 30, pp. 12238–12242, Jul. 2011.

[99] M. D. Watson *et al.*, "Probing the reconstructed Fermi surface of antiferromagnetic $BaFe_2As_2$ in one domain," *npj Quantum Mater.*, vol. 4, no. 1, pp. 1–9, Dec. 2019.

[100] M. A. Tanatar *et al.*, "Origin of the Resistivity Anisotropy in the Nematic Phase of FeSe," *Phys. Rev. Lett.*, vol. 117, no. 12, p. 127001, Sep. 2016.

[101] L. Liu *et al.*, "In-plane electronic anisotropy in the antiferromagnetic orthorhombic phase of

isovalent-substituted $Ba(Fe_{1-x}Ru_x)_2As_2$," *Phys. Rev. B*, vol. 92, no. 9, p. 094503, Sep. 2015.

[102] E. C. Blomberg *et al.*, "In-plane anisotropy of electrical resistivity in strain-detwinned $SrFe_2As_2$," *Phys. Rev. B*, vol. 83, no. 13, p. 134505, Apr. 2011.

[103] I. R. Fisher, L. Degiorgi, and Z. X. Shen, "In-plane electronic anisotropy of underdoped '122' Fe-arsenide superconductors revealed by measurements of detwinned single crystals," *Reports Prog. Phys.*, vol. 74, no. 12, p. 124506, Dec. 2011.

[104] I. Paul and M. Garst, "Lattice Effects on Nematic Quantum Criticality in Metals," *Phys. Rev. Lett.*, vol. 118, no. 22, p. 227601, Jun. 2017.

[105] M. Breitkreiz, P. M. R. Brydon, and C. Timm, "Resistive anisotropy due to spin-fluctuation scattering in the nematic phase of iron pnictides," *Phys. Rev. B*, vol. 90, no. 12, p. 121104, Sep. 2014.

[106] E. F. Andrade *et al.*, "Visualizing the Nonlinear Coupling between Strain and Electronic Nematicity in the Iron Pnictides by Elasto-Scanning Tunneling Spectroscopy," *arXiv: 1812.05287*, Dec. 2018.

[107] J. Schmidt *et al.*, "Nematicity in the superconducting mixed state of strain detwinned underdoped $Ba(Fe_{1-x}Co_x)_2As_2$," *Phys. Rev. B*, vol. 99, no. 6, p. 064515, Feb. 2019.

[108] H. Pfau *et al.*, "Detailed band structure of twinned and detwinned $BaFe_2As_2$ studied with angle-resolved photoemission spectroscopy," *Phys. Rev. B*, vol. 99, no. 3, p. 035118, Jan. 2019.

[109] X. Y. Zheng, R. Feng, D. S. Ellis, and Y. J. Kim, "Bulk-sensitive imaging of twin domains in $La_{2-x}Sr_xCuO_4$ under uniaxial pressure," *Appl. Phys. Lett.*, vol. 113, no. 7, p. 071906, Aug. 2018.

[110] H. H. Kim *et al.*, "Uniaxial pressure control of competing orders in a high-temperature superconductor," *Science.*, vol. 362, no. 6418, pp. 1040–1044, Nov. 2018.

[111] C. Dhital *et al.*, "Effect of uniaxial strain on the structural and magnetic phase transitions in $BaFe_2As_2$," *Phys. Rev. Lett.*, vol. 108, no. 8, p. 087001, Feb. 2012.

[112] X. Lu, R. Zhang, H. Luo, A. H. Nevidomskyy, Q. Si, and P. Dai, "Nematic spin correlations in the tetragonal state of uniaxial-strained $BaFe_{2-x}Ni_xAs_2$," *Science.*, vol. 345, no. 6197, pp. 657–660, 2014.

[113] F. Kretzschmar *et al.*, "Critical spin fluctuations and the origin of nematic order in Ba(Fe 1-x Co x) 2 As 2," *Nat. Phys.*, vol. 12, no. 6, pp. 560–563, Jun. 2016.

[114] S. O. Diallo *et al.*, "Itinerant magnetic excitations in antiferromagnetic $CaFe_2As_2$," *Phys. Rev. Lett.*, vol. 102, no. 18, p. 187206, May 2009.

[115] J. Pelliciari *et al.*, "Local and collective magnetism of EuFe 2 As 2," *Phys. Rev. B*, vol. 95, p. 115152, 2017.

[116] A. N. Yaresko, G. Q. Liu, V. N. Antonov, and O. K. Andersen, "Interplay between magnetic properties and Fermi surface nesting in iron pnictides," *Phys. Rev. B*, vol. 79, no. 14, p. 144421, Apr. 2009.

[117] J. K. Glasbrenner, I. I. Mazin, H. O. Jeschke, P. J. Hirschfeld, R. M. Fernandes, and R. Valentí, "Effect of magnetic frustration on nematicity and superconductivity in iron chalcogenides," *Nat. Phys.*, vol. 11, no. 11, pp. 953–958, Nov. 2015.

[118] J. Maiwald, I. I. Mazin, and P. Gegenwart, “Microscopic Theory of Magnetic Detwinning in Iron-Based Superconductors with Large-Spin Rare Earths,” *Phys. Rev. X*, vol. 8, no. 1, p. 011011, Jan. 2018.

[119] J. P. C. Ruff *et al.*, “Susceptibility anisotropy in an iron arsenide superconductor revealed by X-ray diffraction in pulsed magnetic fields,” *Phys. Rev. Lett.*, vol. 109, no. 2, pp. 1–5, 2012.

[120] Y. Xiao *et al.*, “Field-induced spin reorientation and giant spin-lattice coupling in EuFe2 As2,” *Phys. Rev. B*, vol. 81, no. 22, 2010.

[121] S. Zapf *et al.*, “Persistent detwinning of iron-pnictide EuFe2As2 crystals by small external magnetic fields,” *Phys. Rev. Lett.*, vol. 113, no. 22, p. 227001, Nov. 2014.

[122] S. Jiang *et al.*, “Metamagnetic transition in $EuFe_2As_2$ single crystals,” *New J. Phys.*, vol. 11, no. 2, p. 025007, Feb. 2009.

[123] Q.-P. Ding *et al.*, “Magnetic detwinning and biquadratic magnetic interaction in $EuFe_2As_2$ revealed by 153Eu NMR,” *Phys. Rev. B*, vol. 102, no. 180406, 2020.

[124] W. T. Jin *et al.*, “Phase diagram of Eu magnetic ordering in Sn-flux-grown Eu(Fe1-x Cox)2 As2 single crystals,” *Phys. Rev. B*, vol. 94, no. 18, p. 184513, Nov. 2016.

[125] R. Prozorov and V. G. Kogan, “Effective Demagnetizing Factors of Diamagnetic Samples of Various Shapes,” *Phys. Rev. Appl.*, vol. 10, no. 1, p. 014030, Jul. 2018.

[126] Y. Xiao *et al.*, “Magnetic structure of EuFe 2 As 2 determined by single-crystal neutron diffraction,” *Phys. Rev. B*, vol. 80, no. 17, p. 174424, Nov. 2009.

[127] G. Adhikary *et al.*, “Electronic structure of EuFe2As2,” *J. Phys. Condens. Matter*, vol. 25, no. 22, 2013.

[128] J. J. Ying *et al.*, “Measurements of the Anisotropic In-Plane Resistivity of Underdoped FeAs-Based Pnictide Superconductors,” *Phys. Rev. Lett.*, vol. 107, no. 6, p. 067001, Aug. 2011.

[129] T. Terashima *et al.*, “Magnetotransport studies of EuFe2As2: The influence of the Eu2+ magnetic moments,” *J. Phys. Soc. Japan*, vol. 79, no. 10, 2010.

[130] Y. Xiao *et al.*, “Anomalous in-plane magnetoresistance in a EuFe 2As 2 single crystal: Evidence of strong spin-charge-lattice coupling,” *Phys. Rev. B*, vol. 85, no. 9, p. 094504, Mar. 2012.

[131] G. Kresse and J. Hafner, “Ab. initio molecular dynamics for liquid metals,” *Phys. Rev. B*, vol. 47, no. 1, 1993.

[132] I. I. Mazin, M. D. Johannes, L. Boeri, K. Koepernik, and D. J. Singh, “Problems with reconciling density functional theory calculations with experiment in ferropnictides,” *Phys. Rev. B*, vol. 78, no. 085104, 2008.

[133] N. J. Ghimire *et al.*, “Competing magnetic phases and fluctuation-driven scalar spin chirality in the kagome metal YMn6Sn6,” *Sci. Adv.*, vol. 6, no. 51, p. eabe2680, Dec. 2020.

[134] J. X. Yin *et al.*, “Quantum-limit Chern topological magnetism in TbMn6Sn6,” *Nature*, vol. 583, no. 7817, pp. 533–536, Jul. 2020.

[135] S. Nandi *et al.*, “Coexistence of superconductivity and ferromagnetism in P-doped EuFe2As 2,” *Phys. Rev. B*, vol. 89, no. 1, p. 014512, Jan. 2014.

[136] N. Kurita *et al.*, “Phase diagram of pressure-induced superconductivity in EuFe 2As2 probed by high-pressure resistivity up to 3.2 GPa,” *Phys. Rev. B*, vol. 83, no. 21, p. 214513, Jun. 2011.

[137] W. Uhoya *et al.*, “Anomalous compressibility effects and superconductivity of EuFe 2As2 under high pressures,” *J. Phys. Condens. Matter*, vol. 22, no. 29, 2010.

[138] Y. He *et al.*, “Evidence for competing magnetic and superconducting phases in superconducting Eu 1 - X Sr x Fe 2 - y Co y As 2 single crystals,” *J. Phys. Condens. Matter*, vol. 22, no. 23, p. 235701, Jun. 2010.

[139] Anupam, P. L. Paulose, S. Ramakrishnan, and Z. Hossain, “Doping dependent evolution of magnetism and superconductivity in Eu1-xKxFe2As2 (x = 0-1) and temperature dependence of lower critical field Hc1,” *J. Phys. Condens. Matter*, vol. 23 455702, May 2011.

[140] M. Nicklas, M. Kumar, E. Lengyel, W. Schnelle, and A. Leithe-Jasper, “Competition of local-moment ferromagnetism and superconductivity in Co-substituted EuFe2As2,” *J. Phys. Conf. Ser.*, vol. 273, no. 1, 2011.

[141] G. H. Cao, W. H. Jiao, Y. K. Luo, Z. Ren, S. Jiang, and Z. A. Xu, “Coexistence of superconductivity and ferromagnetism in iron pnictides,” *J. Phys. Conf. Ser.*, vol. 391, no. 1, p. 012123, Dec. 2012.

[142] W. H. Jiao *et al.*, “Anisotropic superconductivity in Eu(Fe0.75Ru0.25) 2As2 ferromagnetic superconductor,” *Epl*, vol. 95, no. 6, p. 67007, Sep. 2011.

[143] U. B. Paramanik, P. L. Paulose, S. Ramakrishnan, A. K. Nigam, C. Geibel, and Z. Hossain, “Magnetic and superconducting properties of Ir-doped EuFe2As 2,” *Supercond. Sci. Technol.*, vol. 27, no. 7, p. 075012, Jul. 2014.

[144] S. Jiang *et al.*, “Superconductivity and local-moment magnetism in Eu (Fe0.89 Co0.11) 2 As2,” *Phys. Rev. B*, vol. 80, no. 18, p. 184514, Nov. 2009.

[145] A. Baumgartner *et al.*, “Reentrant phases in electron-doped EuFe 2 As 2 : Spin glass and superconductivity,” *Phys. Rev. B*, vol. 95, no. 17, p. 174522, May 2017.

[146] W. H. Jiao, Q. Tao, Z. Ren, Y. Liu, and G. H. Cao, “Evidence of spontaneous vortex ground state in an iron-based ferromagnetic superconductor,” *npj Quantum Mater.*, vol. 2, no. 1, p. 50, Dec. 2017.

[147] W. T. Jin *et al.*, “Coexistence of Eu antiferromagnetism and pressure-induced superconductivity in single-crystal ${\rm EuFe}_2 {\rm As}_2$,” *Phys. Rev. B*, vol. 100, p. 14503, 2019.

[148] W. T. Jin *et al.*, “Hydrostatic pressure effects on the static magnetism in Eu(Fe0.925Co0.075)2As2,” *Sci. Rep.*, vol. 7, no. 1, pp. 1–10, Dec. 2017.

[149] Z. Devizorova and A. Buzdin, “Superconductivity-driven helical magnetic structure in EuRbFe4As4 ferromagnetic superconductor,” *Phys. Rev. B*, vol. 100, no. 10, p. 104523, Sep. 2019.